Construction, testing and in-situ operation of the T2K ND280 Electromagnetic Calorimeter

Submitted in accordance with the requirements of
the University of Liverpool for the degree of Master of Philosophy

by

Alex Thorley

January 23, 2016

UNIVERSITY OF
LIVERPOOL

Declaration

I hereby declare that all work contained in this thesis that is not my own has been properly cited and referenced.

Abstract

The T2K experiment is a long baseline, second generation neutrino oscillation experiment located in Japan. Its aim is to measure the θ_{23} and θ_{13} neutrino oscillation mixing angles, as well as to make precision measurements of the atmospheric mass squared difference Δm^2_{32}. Along with its other commitments, the UK was responsible for the design, assembly, testing and commissioning of the near detector's electromagnetic calorimeters, as well as the development of the detector's reconstruction software. Some of the processes by which these objectives were achieved are highlighted within, with a specific focus on physical assembly and testing of the detectors, as well as the development of software designed to estimate the energy of interaction byproducts which arrive in the detector's fiducial volume.

Acknowledgements

This document would not have seen the light of day in the absence of the seemingly limitless supply of patience of my supervisors, as well as the always welcome support from the staff of the Livepool Physics Department, past and present. To Neil, Christos, Dave Joss and Barry King, thank you for affording me the opportunity to help leave a part of the world a better place than I found it, and for allowing me to see this process through to its conclusion, despite many bumps along the way. Carlos, thank you for everything dude. Dave, thank you for continually destroying and rebuilding my self-esteem, and for also being a top-notch bloke. And to Coleman, despite appearances you may actually be my favourite scientist of all time. Keep up the good work.

I'm also eternally grateful to those who have been around for me during what have been an unusually difficult few years, the names of whom are countless. Be that as it may, a special nod to Matt, without the support of whom I'd likely have been found face first in a skip long ago. To Richard, who fell off the jetway again. To Henry, who taught me that sometimes it's okay to come second place in gungame. To Mark, whose levity, compassion and generosity are a credit to the species. To Yan-Jie, whose coathangers I'm still holding hostage. To my brother Andrew who is, and always will be, the best of us. And to Nick Dalby, who amongst many things, taught me not to feed the bad wolf.

And to Lesley, whose companionship I barely deserve, and to whom words need not be spoken... LOVE YA BABE LOLOL xxx

A special thank you to everyone at Radius for being beyond awesome and giving me a chance to find my feet in the world again. Nicholls, Pete, Jamie, cheers chaps. Robert, may your vividly coloured shirts forever damage the retinas of your enemies. Stay righteous and wise, Christopher, and Atanas? Ditch this computing guff and become the Slark player you were born to be.

To those in Japan who took care of us during the events of 2011, I can refer only to the indelible mark left in me having been amongst those who meet adversity and tragedy with kindness, resilience and good humour.

Contents

List of Figures

Chapter 1

Neutrino physics

It could be argued that the neutrino, as an element of nature, has spent most of its career in the sphere of human awareness at a distinct disadvantage. Initially comically miscast as a mere kinematic necessity in an otherwise inexplicable conundrum of early 20th century nuclear physics, it has gone on to serve as a driving force of confirmation and re-evaluation of our understanding of the fabric of nature. In more recent times it has proved itself to be perhaps one of the few experimental vectors of approach in understanding the intricacies of the universe beyond the confines of the hallowed "Standard Model".

1.1 History

1.1.1 The Neutrino

Our journey begins in 1914, the year in which Chadwick discovered that the energy spectrum of emitted β-rays in nuclear decays was continuous [1]. Theorist and experimentalist alike wrangled, scuffled and toiled over the implications of this observation for well over a decade and, amidst the ongoing dispute, in the winter of 1930, Wolfgang Pauli famously and reluctantly submitted a letter to a physics conference in Tübingen. The contents of this missive outlined, as a solution to the β-ray problem, a proposal for a highly penetrating neutral particle with a spin of $\frac{1}{2}$ and whose mass was of a comparable order of magnitude to that of an electron. The rationale for such a proposal was straightforward, rather than forsake the very much sacrosanct axiom of conservation of energy to explain the deviation from expectation in β decay experiments, Pauli instead envisioned a more familiar 3-body kinematic explanation to account for the continuous energy spectrum, in which the total energy available is distributed in the usual way between the expected decay products and a third particle too weakly interacting to detect by the experiments carried out to date. He imbued this mysterious particle with the now obsolete moniker of "neutron".

Upon Chadwick's discovery of a heavy, chargeless and neutral particle in 1932, a now familiar model of the atomic nucleus was cultivated, and in what is arguably history's most underwhelming taxonomic coup d'etat, Pauli's "neutron" was hastily supplanted by this altogether bulkier and more

investigable character. Fortunately, in the intervening years, Enrico Fermi had begun to formulate his theory of beta decay, which was the first major milestone in the development of a theory to describe what we now understand to be the "weak" interaction. In his theory, Fermi adopted the more Italic label "neutrino" to identify Pauli's semantically dislodged particle. The name stuck, and the neutrino as we know it was born.

The explanatory success of Fermi's β-decay theory was compelling, however, the neutrino had yet to be detected by any experiment. This situation was finally rectified in 1956 upon the publication of the results of the first reactor neutrino experiment, conducted by Reines and Cowan [2]. The experiment relied upon a nuclear reactor to provide a large flux of anti-neutrinos from β-decay, and looked for the coincidence of electron-positron annihilation and the absorption of a neutron (and subsequent emission of a photon) by Cadmium nuclei in the reaction $p + \bar{\nu_e} \rightarrow n + e^+$. This experiment provided the long awaited evidence for the existence of the neutrino, as well as establishing the first neutrino cross-section measurement. This pioneering work earned Reines the Nobel Prize in Physics in 1995, in the absence of Cowan who died in 1974.

The experiment at the Brookhaven Alternating Gradient Synchrotron (AGS) [3] confirmed the long speculated notion that the neutrinos produced in reactions involving muons and electrons were distinct. This discovery also hailed the birth of the "neutrino beam method" which is still in use in contemporary neutrino experiments. For this pioneering work, three of the original paper authors (Leon Lederman, Melvin Schwartz and Jack Steinberger) were awarded the Nobel prize in Physics in 1988. In 1974, the Gargamelle [4] bubble chamber experiment presented evidence for the existence of neutral current neutrino interactions, after efforts to develop theories for electroweak unification resulted in a requirement for the existence of a massive weak neutral current mediator. The discovery of the τ lepton in 1975 [5] naturally lead to speculation that it would be accompanied by a τ neutrino, reinforced as time went on by the clear evidence for three light neutrino families in the form of the decay width of the Z^0, (depicted in Figure 1.1) collected by various experiments at LEP [6]. Evidence for the existence of the tau neutrino was finally delivered by the DONUT [7] collaboration in 2000.

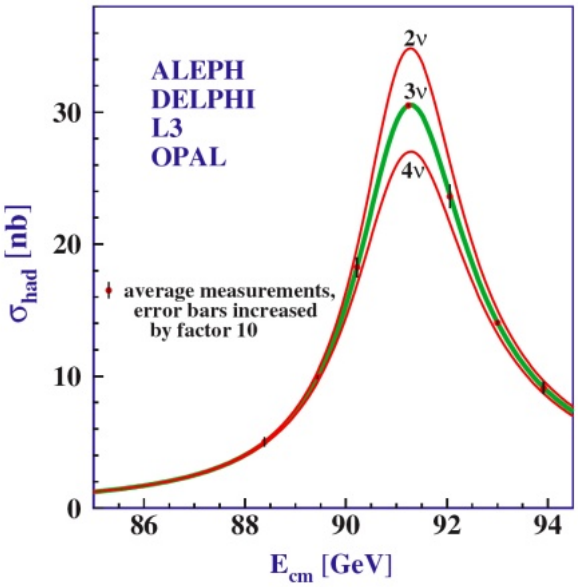

Figure 1.1: Fit involving the number of light neutrino families from data produced by e^+e^- collider experiments. [8]

1.1.2 The Solar and Atmospheric Neutrino Anomalies

The Standard Model of particle physics predicts that neutrinos should be massless [9] [10]. Measurements of neutrino fluxes from various experiments over the years indicated a deficit relative to what was expected from the massless interaction model of the time. These deficits have since been addressed with the collection of evidence in support of a model of neutrino flavour oscillations, first proposed by Bruno Pontecorvo in 1968, analogous to mixing in the quark sector, which requires neutrinos to have mass.

The "Solar Neutrino Problem"

The first experiment to record a deficit in the expected neutrino flux was the Homestake [11] experiment, lead by Raymond Davis. The experimental apparatus consisted of a tank containing 390,000 litres of tetrachloroethylene, located approximately 1.5km underground in a gold mine. Neutrinos produced in nuclear fusion reactions within the sun are captured in the reaction $\nu_e + \mathrm{Cl}^{37} \rightarrow e^- + \mathrm{Ar}^{37}$. The argon is flushed from the tank with gaseous helium and the number of neutrino reactions is determined by counting the number of Ar^{37} decays. The neutrino flux measured by this experiment was 30% of that predicted by the standard solar model. This deficit became known as the "solar neutrino problem".

Kamiokande (Kamioka Nucleon Decay Experiment) [12] was the next experiment to study solar neutrinos, having originally been built to search for the decay of protons. After its upgrade in 1986, the detection of solar neutrinos from $^8\mathrm{B}$ was possible, and the measured deficit in the neutrino flux was consistent with that measured by the Homestake experiment. It was also the first experiment in which the direction and momentum of the final state lepton could be measured, enabling the determination of the trajectory of the incoming neutrino to be uncovered, thereby allowing confirmation that the detected neutrinos originated from the sun.

Further radiochemical neutrino experiments were carried out in the 1990s, all reporting a neutrino flux deficit, and each involving the use of gallium in the capture of electron neutrinos from the sun in the reaction $\nu_e + {}^{71}\text{Ga} \rightarrow {}^{71}\text{Ge} + e^-$, the lower neutrino energy threshold of which allowed detection of solar neutrinos from all of the possible production modes involved in the standard solar model.

Gallium Experiment (GALLEX) [13], located at Gran Sasso, consisted of a 54m^3 tank containing a solution that included 30.3 tons of gallium, and was succeeded by the Gallium Neutrino Observatory (GNO) experiment in 1998. Soviet-American Gallium Experiment (SAGE) [14], situated within a underground laboratory within Mt. Andrychi in Russia, consisted of a set of heated chemical reactors containing a total of 50 tonnes of molten gallium. Both experiments involved the chemical extraction of ^{71}Ge produced by neutrino interactions and its subsequent conversion to germane, which undergoes radioactive decay with a half-life of approximately 11 days.

The resolution of the solar neutrino problem finally arrived with the measurements made by the Sudbury Neutrino Observatory (SNO) [15], located 2km deep within a nickel mine in Ontario, Canada. The detector consists of 10^6kg of highly pure deuterium, held in a spherical volume with a diameter of 12m, and uses inward facing photomultiplier tubes (PMTs) to detect and reconstruct Čerenkov radiation emitted by by-products of neutrino interactions. The presence of deuterium in the target of the experiment allowed a simultaneous measurement of both neutral current and charged current neutrino interactions, which implicitly allowed the measurement of both the total neutrino flux and the electron neutrino flux, owing to the insensitivity of neutral current reactions to neutrino flavour. The measurement of the total neutrino flux was consistent with that expected from the standard solar model, and the first convincing evidence for neutrino oscillations was apparent.

The Atmospheric Neutrino Anomaly

Cosmic rays interacting with the atmosphere produce showers of hadrons, many of which are charged pions. The vast majority of these pions decay by the process $\pi^+ \rightarrow \mu^+ + \nu_\mu$ and the conjugate charge process $\pi^- \rightarrow \mu^- + \bar{\nu}_\mu$, and the charged muons decay by $\mu^+ \rightarrow e^+ + \nu_e + \bar{\nu}_\mu$ and $\mu^- \rightarrow e^- + \bar{\nu}_e + \nu_\mu$. It was expected from these decay modes that the number of detected muon neutrinos of atmospheric origin would be approximately double that of atmospheric electron neutrinos. Results from Kamiokande in 1988 [16] showed that the measured ratio deviated from this expectation, and it was found that while the electron neutrino measurement was consistent with expectation, the muon neutrino measurement was much lower than predicted. The resolution of the anomaly came with the realisation that the measured rate of muon neutrino interactions could be explained by their oscillation of flavour in flight, as the rate had a strong dependence on the direction of the reconstructed muons, with up-going reconstructed muons from beneath the detector exhibiting the deficit. The evidence for this explanation was significantly bolstered with the publication of results from Kamiokande's successor Super-Kamiokande in 1998 [17], which strongly supported an atmospheric neutrino oscillation explanation for the observed deficit.

1.2 Neutrino-Nucleon Scattering

Neutrinos interact with nucleons by the exchange of massive, weak-force mediating vector bosons [18] [19], and lepton flavour is conserved at the weak interaction vertex. Charged Current (CC) interactions involve the exchange of the electrically charged $W^{\pm}$ bosons, while Neutral Current (NC) interactions are mediated by the electrical neutral Z boson. T2K relies upon the detection of charged current neutrino interactions in making flavour oscillation measurements by searching for the final state outgoing lepton in order to determine the original neutrino flavour. The total charged current cross section is a function of the energy of the participating neutrino, and in T2K's typical neutrino energy range (~1GeV) the total cross section is composed of contributions from a number of processes, as shown in Figure 1.2.

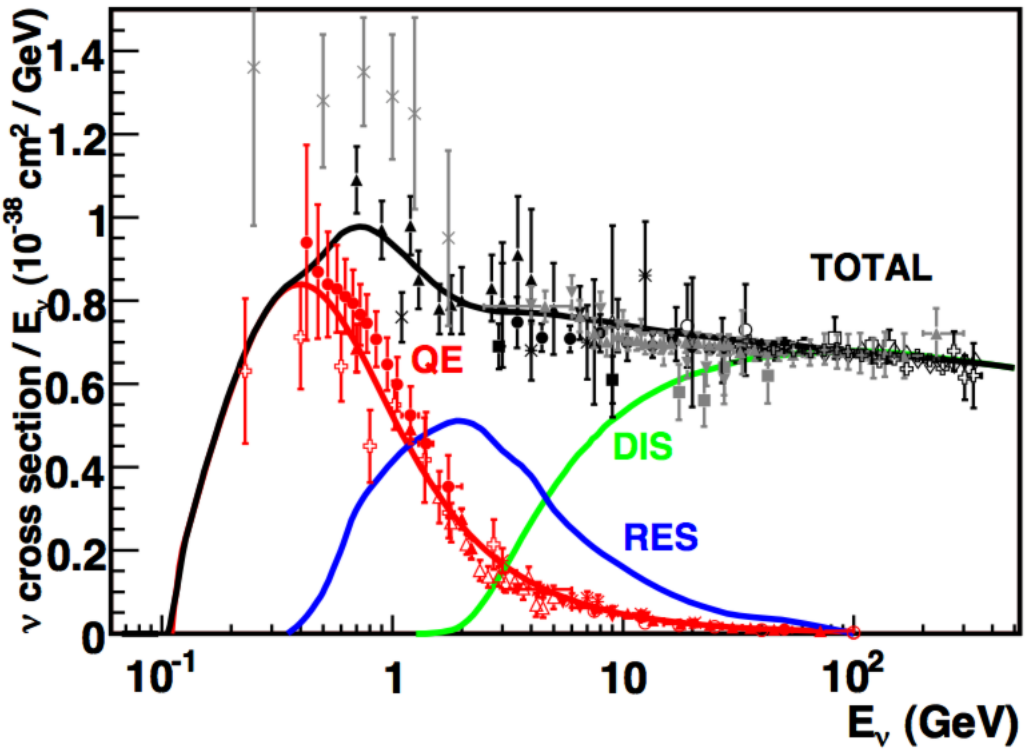

Figure 1.2: ν_μ charged current cross section measurement breakdown, from [20]

Charged current quasi-elastic (CCQE) interactions dominate in the region below 1GeV, a typical CCQE interaction is depicted in Figure 1.3a. This channel is particularly useful for T2K as it is a two body process, in which only the outgoing angle and lepton momentum are required to reconstruct the neutrino energy.

The CCQE cross-section is described by the Llewellyn-Smith [21] model and has two parameters (the axial mass M_A and the vector mass M_V) which are currently determined by experimental measurement. Moving beyond 1GeV, the contribution to the total cross section from charged current resonant (CCRES) production matches and subsequently exceeds that of CCQE, and involves the generation of a Δ resonance which then decays to a nucleon and a pion, as depicted in Figure 1.3b. The resonant cross-section is described by the Rein-Sehgal model [22].

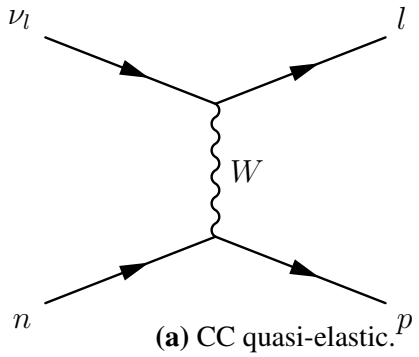

(a) CC quasi-elastic.

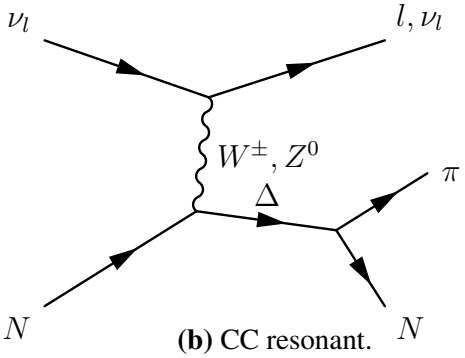

(b) CC resonant.

Finally, above a few GeV, charged current deep inelastic scattering processes (CCDIS) dominate the cross section (described by the Bodek-Yang model [23]), in which a neutrino has sufficient energy to resolve an individual quark and break a hadron apart. Charged current coherent pion production (CCCOH) is distinct from CCRES interactions in that the neutrino coherently interacts with the nucleus, and is also described by the Rein-Sehgal model.

Each of these interaction channels has a neutral current analogue, differing only in the mediating gauge boson (the Z^0) and the fact that neutral current interactions have a neutrino in the final state, as opposed to a charged lepton of the appropriate flavour. Of particular note to T2K are neutral current channels with neutral pions in their final state, an example of which is depicted in Figure 1.4a. The lack of an outgoing lepton in NC interactions coupled with the decay of the neutral pion to two photons can easily be mistaken for a CC interaction if the photons are misreconstructed.

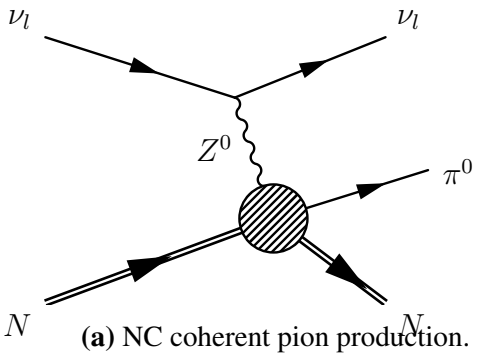

(a) NC coherent pion production.

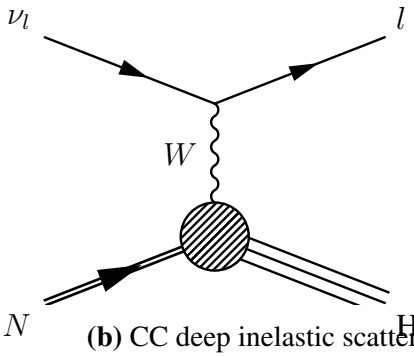

(b) CC deep inelastic scattering.

1.3 Neutrino Oscillations

The standard theory of neutrino oscillations states that the creation of a neutrino with a set flavour eigenstate $|\nu_\alpha\rangle$ is composed of a linear superposition of mass eigenstates $|\nu_1\rangle$, $|\nu_2\rangle$ and $|\nu_3\rangle$ [24] [25]. The implication is that in order for flavour oscillations to occur, neutrinos must have associated to them some mass, which was not an original prediction of the standard model.

Flavour Oscillation Probability in Vacuum

As stated, the weak flavour eigenstates of a neutrino are related to the mass eigenstates by a 3x3 unitary matrix U:

$$|\nu_\alpha\rangle = \sum_k U^*_{\alpha k} |\nu_k\rangle \tag{1.1}$$

Where U is the Pontecorvo-Maki-Nakagawa-Sakata (PMNS) mixing matrix which has historically been represented as a product of three 3x3 matrices:

$$U = \begin{pmatrix} 1 & 0 & 0 \\ 0 & c_{23} & s_{23} \\ 0 & -s_{23} & c_{23} \end{pmatrix} \begin{pmatrix} c_{13} & 0 & s_{13}e^{-i\delta} \\ 0 & 1 & 0 \\ -s_{13}e^{i\delta} & 0 & c_{13} \end{pmatrix} \begin{pmatrix} c_{12} & s_{12} & 0 \\ -s_{12} & c_{12} & 0 \\ 0 & 0 & 1 \end{pmatrix} \tag{1.2}$$

where $c_{ij} = \cos(\theta_{ij})$, $s_{ij} = \sin(\theta_{ij})$ and δ is a CP violation phase. This particular factorisation is representative of the distinct experimental sectors which each neutrino mixing angle corresponds to, with θ_{23} associated with atmospheric experiments and θ_{12} to solar experiments.

In order to determine the oscillation probability as a function of the distance travelled by the neutrino, we rely on the Schrödinger equation to determine how the initial state varies with time, assuming a plane wave solution the equation, which is given by:

$$|\nu_\alpha(t)\rangle = \sum_k U^*_{\alpha k} e^{-iE_k t} |\nu_k\rangle \tag{1.3}$$

By employing the unitarity of the mixing matrix, equation 1.1 can be rearranged to give the mass eigenstates in terms of the flavour eigenstates:

$$|\nu_k\rangle = \sum_\alpha U_{\alpha k} |\nu_\alpha\rangle \tag{1.4}$$

Which leads, by substitution of equation 1.4 into equation 1.3, to an expression relating the mixing of mass eigenstates of a flavour state $|\nu_\alpha(t)\rangle$ after an elapsed time t:

$$|\nu_\alpha(t)\rangle = \sum_{\beta=e,\mu,\tau} \left(\sum_k U^*_{\alpha k} e^{-iE_k t} U_{\beta k} \right) |\nu_\beta\rangle \tag{1.5}$$

To determine the amplitude of the transition from $|\nu_\alpha\rangle$ to $|\nu_\beta\rangle$ as a function of time, we evaluate $\langle\nu_\beta|\ \nu_\alpha(t)\rangle$:

$$\langle\nu_\beta|\ \nu_\alpha(t)\rangle = \sum_k U^*_{\alpha k} e^{-iE_k t} U_{\beta k} \tag{1.6}$$

The transition probability is then given by: $|\langle\nu_\beta|\ \nu_\alpha(t)\rangle|^2$:

$$P_{\nu_\alpha \to \nu_\beta}(t) = \sum_{k,j} U^*_{\alpha k} U_{\beta k} U_{\alpha j} U^*_{\beta j} e^{-i(E_k - E_j)t} \tag{1.7}$$

In the ultra-relativistic limit, t can be approximated to L, the distance travelled (in natural units). The energy can also be approximated as $E_k \approx E + \frac{m_k^2}{2E}$ which yields:

$$\begin{aligned} E_k - E_j &\approx E + \frac{m_k^2}{2E} - \left(E + \frac{m_j^2}{2E}\right) \\ &\approx \frac{m_k^2 - m_j^2}{2E} \\ &= \frac{\Delta m_{kj}^2}{2E} \end{aligned} \tag{1.8}$$

The final expression for the vacuum oscillation probability can therefore be written as:

$$P_{\nu_\alpha \to \nu_\beta}(L, E) = \sum_{k,j} U_{\alpha k}^* U_{\beta k} U_{\alpha j} U_{\beta j}^* e^{-i\frac{\Delta m_{kj}^2 L}{2E}} \tag{1.9}$$

This expression indicates that the amplitude of neutrino oscillations is determined purely by the product of the various mixing matrix elements, which are fixed parameters. The experimentalist has control over the distance from the neutrino source to the detector, as well as the neutrino energy, and these parameters determine the phases of neutrino oscillations.

Equation 1.9 can also be expressed, using the unitarity of the PMNS matrix as:

$$\begin{aligned} P_{\nu_\alpha \to \nu_\beta}(L, E) = \delta_{\alpha\beta} - 4 \sum_{k>j} \Re\left[U_{\alpha k}^* U_{\beta k} U_{\alpha j} U_{\beta j}^*\right] \sin^2\left(\frac{\Delta m_{kj}^2 L}{4E}\right) \\ + 2 \sum_{k>j} \Im\left[U_{\alpha k}^* U_{\beta k} U_{\alpha j} U_{\beta j}^*\right] \sin\left(\frac{\Delta m_{kj}^2 L}{2E}\right) \end{aligned} \tag{1.10}$$

Two and Three Flavour Oscillation

Often, considering the oscillation model in the case of only two massive neutrinos can be beneficial in the illustration and simplification of determining expressions for the transition probabilities. We start with U, a 2x2 mixing matrix

$$U = \begin{pmatrix} \cos\theta & \sin\theta \\ -\sin\theta & \cos\theta \end{pmatrix} \tag{1.11}$$

where θ is the sole mixing angle. There is also only one mass-squared difference to consider, namely $\Delta m^2 = \Delta m_{21}^2 = m_2^2 = m_1^2$.

Using equation 1.10, we can determine the probabilities of appearance (provided they are distinct) and survival in the general case of a neutrino ν_α oscillating to ν_β,

$$P_{\nu_\alpha \to \nu_\beta}(L, E) = \sin^2 2\theta \sin^2 \frac{\Delta m^2 L}{4E} \tag{1.12}$$

$$P_{\nu_\alpha \to \nu_\alpha}(L,E) = 1 - P_{\nu_\alpha \to \nu_\beta}(L,E) = 1 - \sin^2 2\theta \sin^2 \frac{\Delta m^2 L}{4E} \tag{1.13}$$

These equations are approximately valid for situations in which a particular oscillation angle dominates, allowing one to forgo evaluating the full three flavour oscillation transition probability. In the case of three flavour probability oscillations, one again uses equation 1.10, this time in conjunction with the full 3x3 PMNS matrix (which is obtained by multiplying through the matrices defined in Equation 1.2):

$$U = \begin{pmatrix} c_{12}c_{13} & s_{12}c_{13} & s_{13}e^{-i\delta} \\ -s_{12}c_{23} - c_{12}s_{23}s_{13}e^{i\delta} & c_{12}c_{23} - s_{12}s_{23}s_{13}e^{i\delta} & s_{23}c_{13} \\ s_{12}s_{23} - c_{12}c_{23}s_{13}e^{i\delta} & -c_{12}s_{23} - s_{12}c_{23}s_{13}e^{i\delta} & c_{23}c_{13} \end{pmatrix} \tag{1.14}$$

In the particular case of T2K, the main transition probabilities of interest are the ν_e appearance probability $P(\nu_\mu \to \nu_e)$ and the ν_μ disappearance probability $P(\nu_\mu \to \nu_\mu)$, and with the aid of Equations 1.10 and 1.14, expressions for these transition probabilities can be determined.

It is also important to note that these equations are generally only valid for neutrinos oscillating in vacuum, the transition probability of a neutrino traversing matter is altered by the "MSW" effect [26] [27]. Typically, neutrinos only interact with nucleons via the mediation of the Z^0, and the amplitude of this process is independent of the neutrino flavour. However, electron neutrinos coherently forward scatter with the electrons in atomic nuclei by exchange of a W boson, which can serve to alter the effective oscillation parameters involved and hence the oscillation probability. For the T2K baseline and neutrino energy, this effect is insignificant and can be ignored.

Mass Hierarchy

Results from neutrino oscillation experiments so far indicate that the differences between the three neutrino masses are such that two of the masses are similar in magnitude, with the mass of the third relatively displaced as shown in Figure 1.5, where the "normal" mass hierarchy corresponds to $m_1 < m_2 < m_3$ and the "inverted" hierarchy corresponds to $m_3 < m_1 < m_2$. The absolute neutrino masses have yet to be measured directly, with only upper limits having been established so far, and oscillation measurements have so far been insensitive to the sign of Δm^2_{23}

1.4 Status of Oscillation and Mass Parameter Measurements

In the wake of the evidence for neutrino oscillations, the race to constrain the neutrino mixing parameters began. Many experiments around the world of various configurations are currently running or are on the table in a bid to improve our understanding of the neutrino mixing matrix, with a number of experiments recently confirming the non-zero value of θ_{13}, which paves the way for an investigation into CP-violation in the lepton sector.

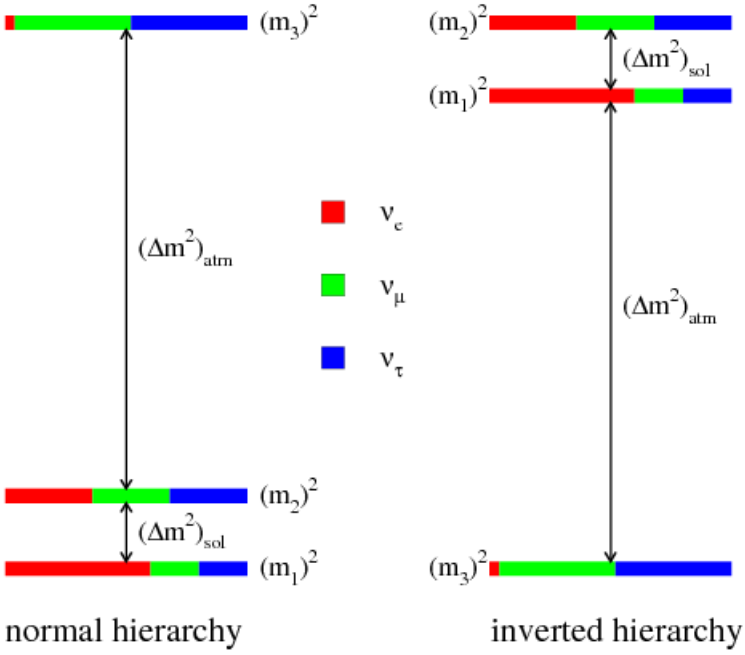

Figure 1.5: The two neutrino mass hierarchies as supported by current oscillation measurements, from [20]

Reactor Neutrino Experiments

Contemporary and past reactor neutrino efforts use the same detection method originally employed by Reines and Cowan, employing the enormous flux of $\bar{\nu_e}$ from nuclear reactors to detect electron anti-neutrino interactions, and their measurements are summarised below.

The Daya Bay [28] experiment consists of eight detectors situated in the vicinity of six nuclear reactors, at various baselines as indicated in Figure 1.6, and aims to measure θ_{13} to better than 0.01 at the 90% confidence limit by measuring the survival probability of anti-neutrinos. The experiment was the first to announce a 5.2σ "discovery" of a non-zero θ_{13}, and its current status is a measurement of $\sin^2 2\theta_{13} = 0.089 \pm 0.010(\text{stat.}) \pm 0.005(\text{syst.})$

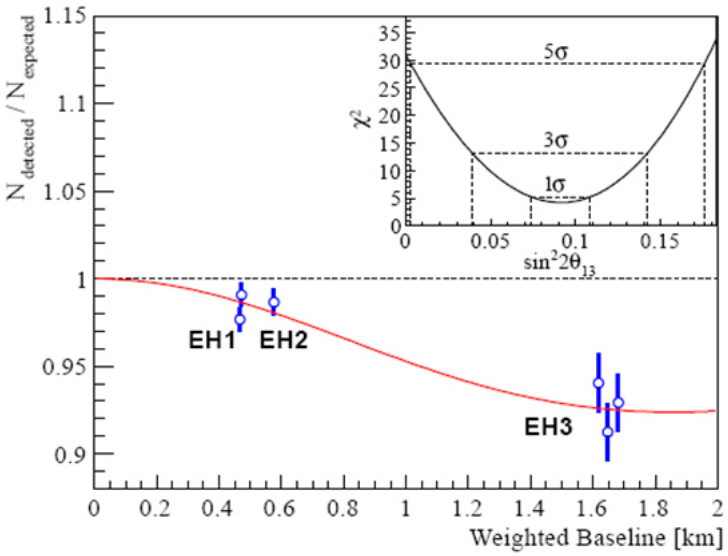

Figure 1.6: Ratio of predicted to detected antinuetrino events at each Daya Bay site, from [28].

This result was subsequently confirmed by the Reactor Experiment For Neutrino Oscillation (RENO) [29] situated in Korea. The experiment consists of two detectors placed in the vicinity of six nuclear reactors, and the experiment reported a measurement of $\sin^2 2\theta_{13} = 0.113 \pm 0.013(\text{stat.}) \pm 0.019(\text{syst.})$

The Chooz [30] and Double Chooz [31] experiments, located in France, measure the anti-neutrino flux of two nuclear reactors at the Chooz nuclear power station with the aid of a single liquid scintillator detector. Chooz reported no evidence for oscillations at the 90% confidence limit at its sensitivity range, however Double Chooz presented a measurement of $\sin^2 2\theta_{13} = 0.109 \pm 0.030(\text{stat.}) \pm 0.025(\text{syst.})$.

The Palo Verde experiment [32], located in the United States, consisted of a detector placed in the vicinity of three nuclear reactors, and ran for 350 days. It reported exclusion of $\bar{\nu_e} \leftrightarrow \bar{\nu_x}$ oscillations at the 90% confidence limit for $\Delta m^2 > 1.1 \times 10^{-3} eV^2$ at full mixing, and $\sin^2 2\theta < 0.17$ at large Δm^2.

The KamLAND [33] experiment, located in Japan, is designed to measure θ_{12} and Δ^2_{21}, and did so by measuring the anti-neutrino flux from a large number of nuclear reactors distributed around Japan, and reports the results of a joint solar neutrino analysis as $\Delta m^2 = 7.9^{+0.6}_{-0.5} \times 10^{-5}\text{eV}^2$ and $\tan^2\theta = 0.40^{+0.10}_{-0.07}$.

Accelerator Neutrino Experiments

Accelerator neutrino experiments rely on accelerating and subsequently impinging hadrons onto a target material, where the subsequent decay of electromagnetically focused charged mesons in the debris produces a beam of muon neutrinos, which are then detected by separate apparatus downstream of the beam source.

The Main Injector Neutrino Oscillation Search (MINOS) [34] experiment was a long baseline neutrino experiment based in the United States, in which a beam of neutrinos is fired from Fermilab at a far detector 735km away. A near detector is also located approximately 1km from the pro-

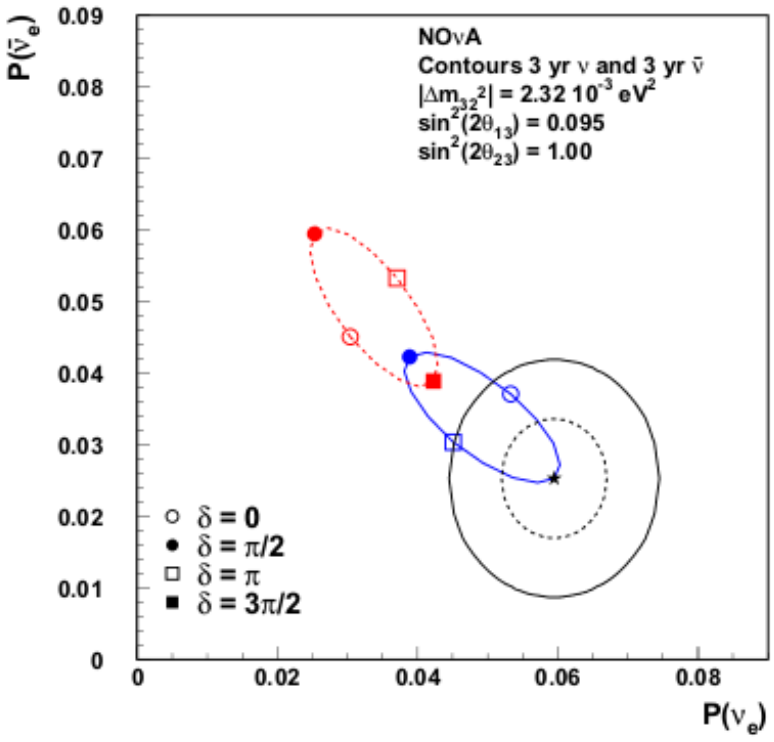

Figure 1.7: Nova appearance measurement probability contours for fixed θ_{13} and θ_{23}. The solid blue ellipse corresponds to the normal hierarchy scenario, the red dashed corresponds to the inverted hierarchy, from [35]

duction target. The experiment aimed to measure Δm^2_{32} and θ_{23}, and reported best fit results of $|\Delta m^2| = 2.39^{+0.09}_{-0.10} \times 10^{-3}\text{eV}^2$ and $\sin^2 2\theta = 0.957^{+0.035}_{-0.036}$

The NuMi Off-Axis ν_e Appearance experiment (NOνA) [35] will be a long baseline neutrino oscillation experiment located in the United States, intended to be a successor to MINOS. It will consist of a beam-line located at Fermilab with a far detector 810km away in Minnesota, with a near detector located on the Fermilab site. With the length of the baseline involved, the experiment will be sensitive to matter effects, the neutrino mass hierarchy and the CP violating phase δ, with sensitivities as depicted in Figure 1.7.

The KEK To Kamioka (K2K) [36] experiment was a long baseline neutrino experiment based in Japan, in which a beam of ν_μ was aimed from KEK to Super-Kamiokande. The experiment aimed to measure ν_μ disappearance thereby allowing a measurement of Δm^2_{23} and θ_{23}. The experiment reported best fit results of $\sin^2 2\theta_{23} = 1$ and $\Delta m^2_{23} = 2.8 \times 10^{-3}\text{eV}^2$.

OPERA [37] is a long baseline neutrino oscillation experiment in which a beam of ν_μ is generated from the CERN SPS. The far detector consists of a combination of electronic tracker and nuclear emulsion based detectors, and is located 730km from the beam source at Gran Sasso National Laboratory. The experimental aim is to measure the appearance of ν_τ in a ν_μ beam and, as of 2012, the experiment has detected two ν_τ candidates.

The Long-Baseline Neutrino Experiment (LBNE) [38] is a proposed experiment which aims to study neutrino oscillation parameters, with an emphasis on investigating CP violation and the mass hierarchy. The provisional hardware configuration consists of a 700kW neutrino beam generated at Fermilab and aimed at a far detector situated 1300km away in South Dakota.

Current Status of Mixing Parameter Measurements

The current experimentally determined values are shown in Table 1.1, and are obtained from a global analysis of neutrino oscillation data from various experiments.

Oscillation Parameter	Best Fit ($\pm 1\sigma$)
$\sin^2 2\theta_{12}$	$0.307^{+0.018}_{-0.016}$
$\sin^2 2\theta_{23}$	$0.386^{+0.024}_{-0.021}$ $(0.392^{+0.039}_{-0.022})$
$\sin^2 2\theta_{13}$	0.0241 ± 0.0025 $(0.0244^{+0.0023}_{-0.0025})$
$\Delta m^2_{21} \times 10^{-5}\text{eV}^2$	$7.54^{+0.26}_{-0.22}$
$\lvert\Delta m^2\rvert \times 10^{-3}\text{eV}^2$	$2.43^{+0.06}_{-0.10}$ $(2.42^{+0.07}_{-0.11})$

Table 1.1: Current neutrino mixing matrix parameter measurements, determined by a global analysis to available data. The values in brackets correspond to fits assuming an inverted mass hierarchy, and $\Delta m^2 = m^2_3 - \frac{m^2_2+m^2_1}{2}$, from [39]

Parameter Measurement Inconsistencies

While most oscillation experiments have reported mutually consistent measurements, two experiments have reported measurements which are anomalous when compared against the current global values for Δm^2_{32}, and remain unexplained. The Liquid Scintillator Neutrino Detector (LSND) [40] searched for electron anti-neutrino appearance from a beam of muon anti-neutrinos, with the ability to switch the beam polarity to search for electron neutrino appearance. The anomalous measurement came in the form of an excess of electron anti-neutrino events, with the implication that the inferred value for Δm^2_{32} was notably inconsistent with the world average. The MiniBooNE [41] experiment, built to search for $\nu_\mu \rightarrow \nu_e$ oscillation, also reported excesses in both ν_μ and $\bar{\nu_\mu}$ running modes.

Chapter 2

Tokai to Kamioka

2.1 Overview and Experimental Objectives

The Tokai to Kamioka (T2K) [42] experiment is a long baseline neutrino oscillation experiment based in Japan. The primary motivation for its development is the measurement of the formerly undetermined θ_{13} mixing angle through ν_e appearance (Figure 2.2), which until recently had remained unmeasured. Secondary objectives of the experiment include precision measurements of the mixing angle θ_{23} and the mass-squared difference parameter Δm^2_{23} through ν_μ disappearance. Phase two of the experiment will aim to make a measurement of the the CP-violating phase δ_{cp} by running in anti-neutrino mode, which is now a feasible objective given the recently determined non-zero value of θ_{13}. The current status of the experiment is a 7.3σ significance measurement of electron neutrino appearance, with 28 events measured against an expected background of 4.92 events from the non-oscillation hypothesis, giving a best fit value of $\sin^2 2\theta_{13} = 0.140^{+0.038}_{-0.032}$ assuming $\delta_{\text{cp}} = 0$ and $|\Delta m^2_{32}| = 2.4 \times 10^{-3}\text{eV}^2$ [43].

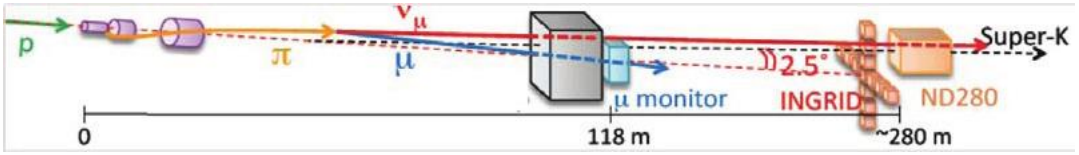

Figure 2.1: Illustrating the scale of T2K neutrino beamline and near detector complex [44].

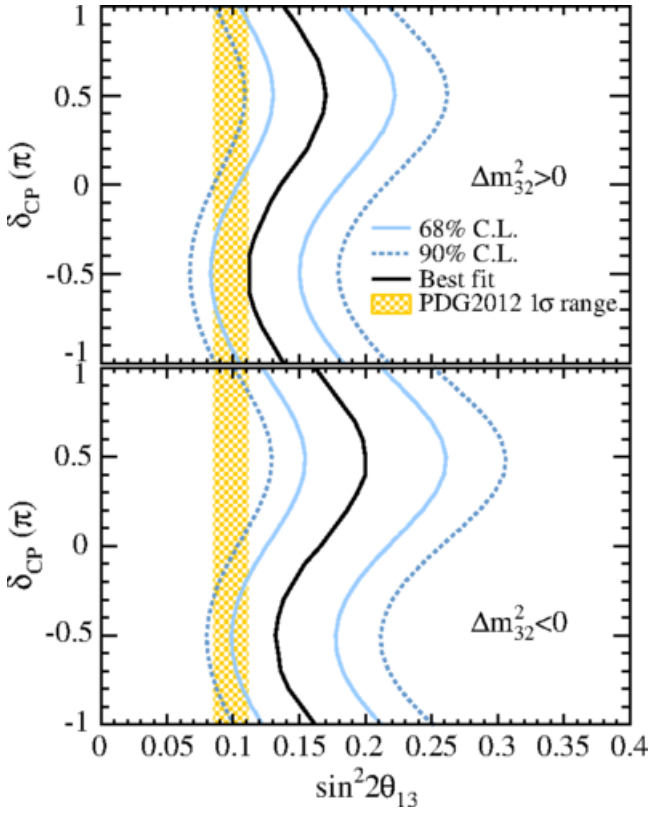

Figure 2.2: The 68% and 90% confidence limit allowed regions for $\sin^2 2\theta_{13}$, as a function of the CP violating phase, assuming normal (inverted) hierarchy at the top (bottom), from [45]

2.2 Proton Accelerator and the Neutrino Beamline

The recently constructed J-PARC facility [42] in Tōkai-mura provides the neutrino flux for the experiment. A beam of ν_μ is created at the J-PARC facility, and is aimed at the Super-Kamiokande far detector, as depicted in Figure 2.1. A near detector is situated 280 metres from the neutrino production target, which serves to make cross-section measurements and constrain backgrounds to the appearance measurement at Super-K. The process by which the beam is generated occurs in three stages, employing a range of particle accelerator hardware along the way, depicted in Figure 2.3. Firstly, a beam of H^- is accelerated by the linear accelerator (LINAC) up to a maximum kinetic energy of 400MeV. This H^- beam is then transformed to a proton beam by charge-stripping foils, which remove bound electrons from the constituent atoms of the beam, and this occurs at the point at which the beam is injected into a rapid-cycling synchotron (RCS).

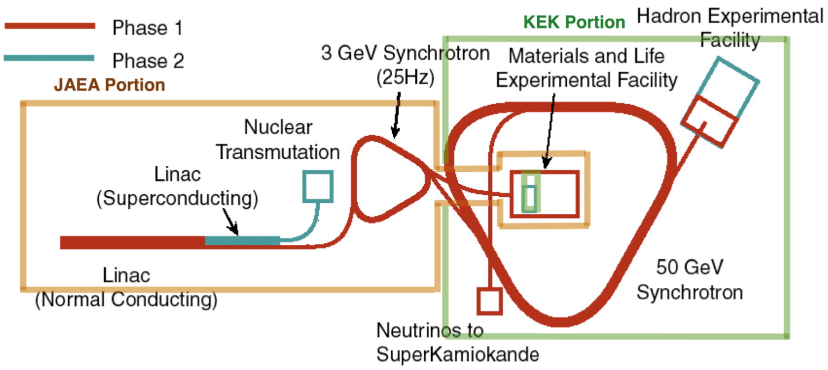

– Phase 1 + Phase 2 = 1,890 Oku Yen (= $1.89 billions if $1 = 100 Yen).
– Phase 1 = 1,527 Oku Yen (= $1.5 billions) for 8 years.
– JAEA: 860 Oku Yen (56%), KEK: 667 Oku Yen (44%).

Figure 2.3: Schematic diagram of J-PARC accelerators [46].

The RCS subsequently accelerates the proton beam to a kinetic energy of 3GeV, at which point the beam enters the main ring (MR) and is accelerated to 30GeV. The proton beam is arranged into a chain of eight "bunches" (six for Run 1 data), a fact which is used extensively in analyses to reject backgrounds at ND280 and Super-Kamiokande. These bunches are are fast extracted from the MR with the aid of kicker magnets to the neutrino beamline, shown in Figure 2.4.

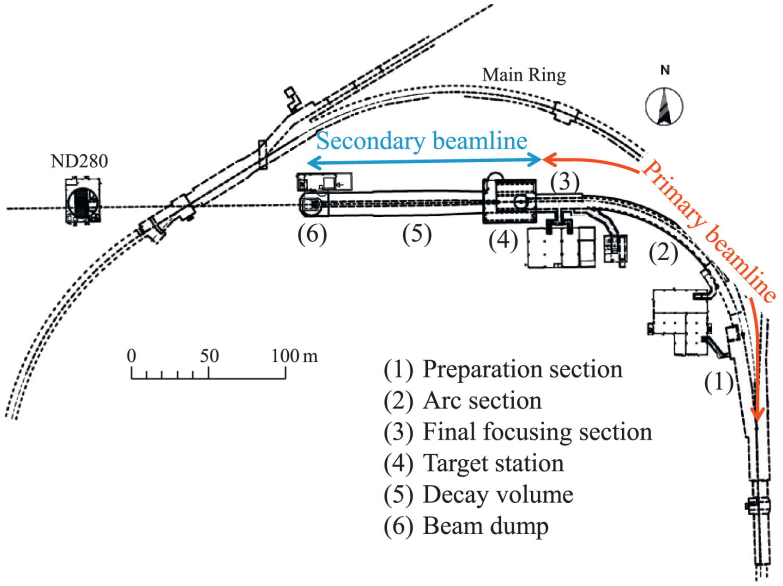

Figure 2.4: T2K neutrino beamline overview [42].

The primary beamline bends the proton beam toward Super-Kamiokande, the secondary beamline (shown in Figure 2.5) contains a graphite target upon which the proton beam impacts, producing a beam of largely pions and a small number of kaons. The debris is focused by a series of electromagnetic horns, and the pions and kaons decay in flight to $\mu^+\nu_\mu$, which constitute the muon neutrino beam. Some contamination of ν_e is introduced via muon decay and alternate decay channels of the kaon.

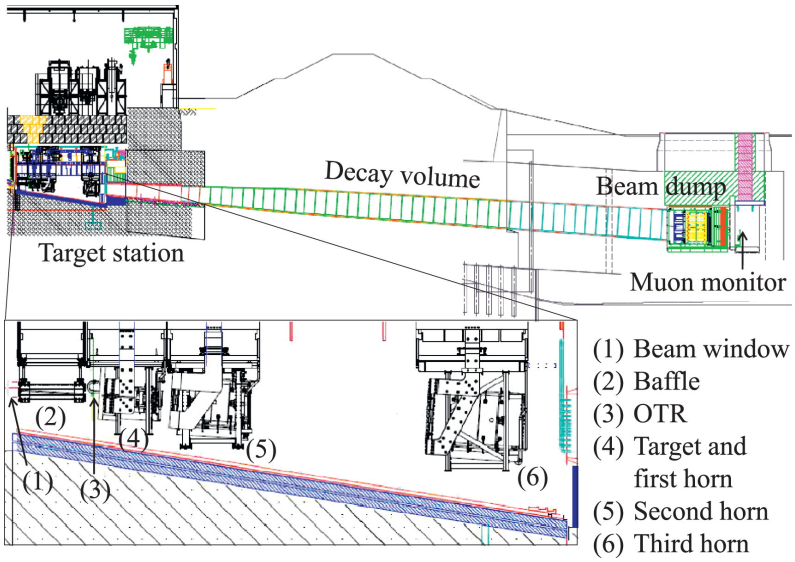

Figure 2.5: T2K secondary beamline [42].

2.3 Interactive Neutrino GRID: On-axis

The Interactive Neutrino GRID (INGRID) [47] detector serves as the on-axis detector component of the ND280 facility, and consists of a total of 17 detector modules. 14 of the modules are arranged in a cross shape, with the remaining two placed at symmetric points in the two upper quadrants of the arrangement, as depicted in Figure 2.6. The remaining module differs from the other 16, and is labelled the "Proton Module". The beam centre is intended to correspond to the centre position of the cross arrangement, and is measured to a precision better than 10cm.

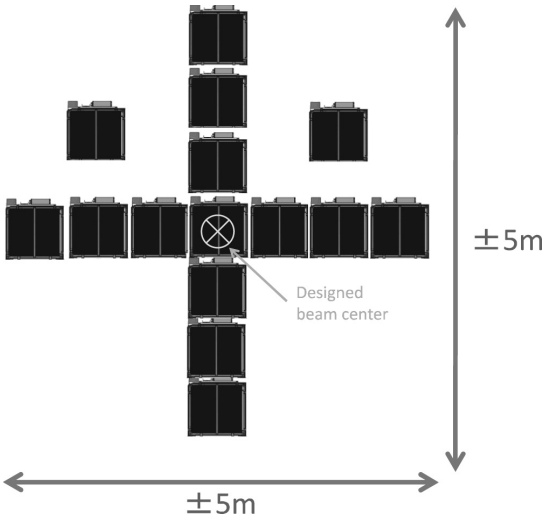

Figure 2.6: Diagram of the full INGRID on-axis detector [47].

A single INGRID module consists of an alternating sequence of nine iron plates and 11 layers of extruded plastic scintillator, and each module is surrounded by layers of polystyrene scintillator intended to serve as a veto for events originating outside of the module, as shown in Figure 2.7. The

"Proton Module" consists entirely of scintillator layers internally and is surrounded by veto layers. The physical dimensions of the scintillator bars used in the "Proton Module" differ from those used in the other modules, in a bid to improve the granularity of particle tracking.

The iron layers serve as the target material for the module, and have dimensions 124cm $\times$ 124cm $\times$ 6.5cm. The total mass of all of the iron layers in each module is 7.4 tons. Each of the 11 scintillator layers are comprised of 48 plastic scintillator bars, equally divided in number into two perpendicular orientations to allow three dimensional particle tracking. Each scintillator bar is threaded with wavelength shifting (WLS) fibre, and each fibre is instrumented with a single MPPC.

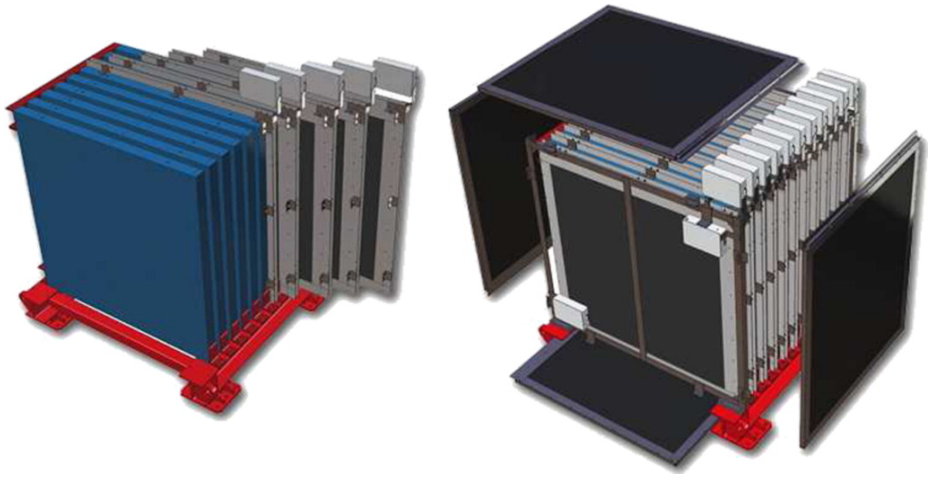

Figure 2.7: Engineering diagram of a single INGRID module [42].

The purpose of INGRID is to perform a precise measurement of the beam direction and intensity on its axis, an example measurement is shown in Figure 2.8. The 2.5° off-axis configuration of the T2K baseline levies the requirement that the beam direction is accurate to within $\pm$1mrad, as the peak neutrino energy of the beam is a function of the off-axis angle. The Proton Module of INGRID facilitates the measurement of final state muons and protons which emanate from CCQE interactions, allowing comparisons of collected data with beamline and neutrino interaction simulations.

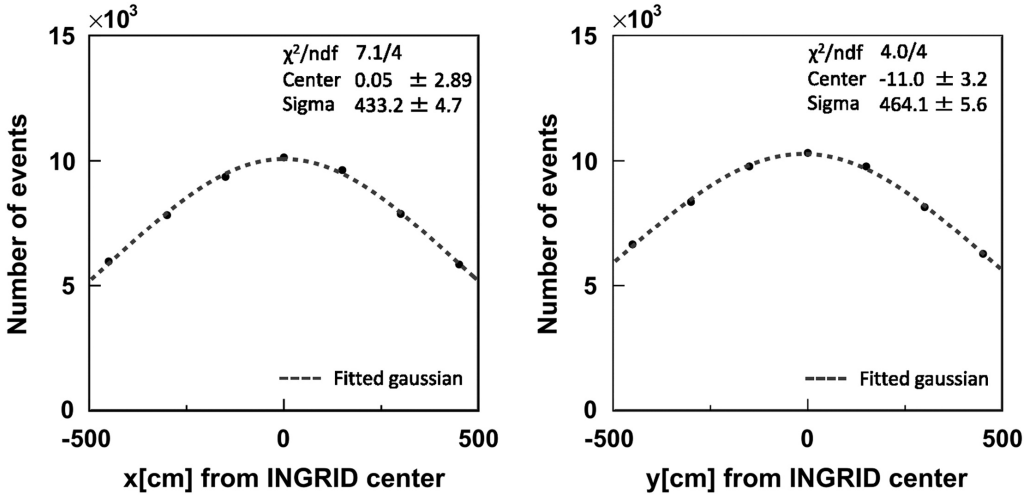

Figure 2.8: Measured neutrino beam profiles by INGRID in the X and Y planes (left and right figures respectively) [47].

2.4 ND280: Off-axis

The off-axis component of the ND280 detector [42] [44] complex consists of a collection of sub-detectors, housed within a region magnetised by the former UA1/NOMAD magnet. The entire facility consists of the π^0 Detector, two Fine Grained Detectors, three Time Projection Chambers, an Electromagnetic Calorimeter, a Side Range Muon Detector and the UA1/NOMAD magnet. The π^0 Detector, Fine Grained Detectors, the Time Projection Chambers and the Downstream ECAL are held in place within a basket of dimension 6.5m $\times$ 2.6m $\times$ 2.5m, and the UA1 magnet both encloses the basket and serves as the mechanical support for the Electromagnetic Calorimeter and the Side Range Muon Detector, as depicted in Figure 2.9.

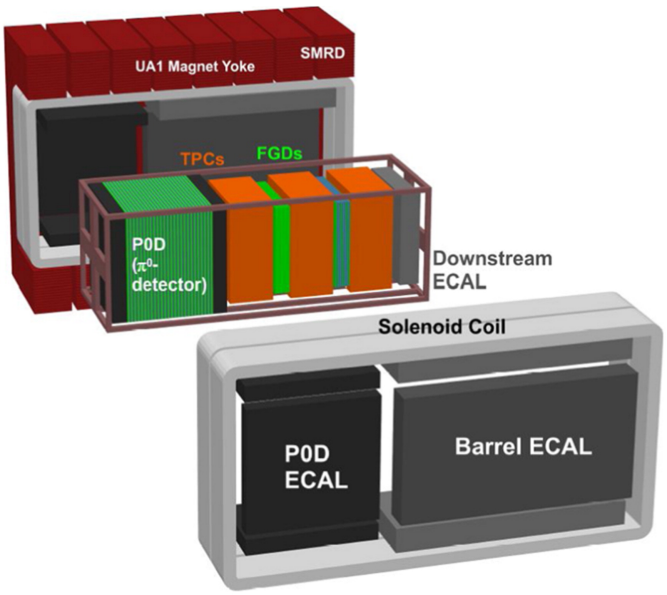

Figure 2.9: Exploded view of ND280's off-axis subdetectors [48].

The off-axis near detector was designed to fulfil a number of critical roles in the experiment. It is

located 280 metres from the neutrino production point to ensure that the beam composition and flux can be sampled before the beam constituents can undergo flavour oscillation. This allows predictions of the unoscillated beam flux to be made at Super-Kamiokande. The flavour composition of the beam is also an important measurement to make for oscillation analyses, as the beam contains a contamination of ν_e which must be determined owing to its status as an irreducible background to a ν_e oscillation appearance measurement at Super-K.

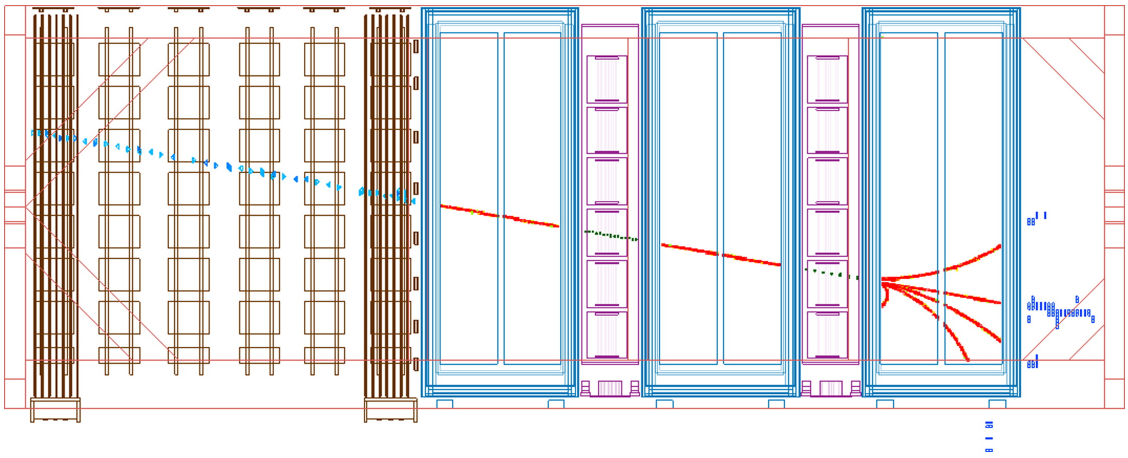

Figure 2.10: Two dimensional projection of the ND280 sub-detectors, showing an event containing a muon track entering from the left [42].

Finally, the detector must be able to make a measurement of the neutral current π^0 production rate, as this also constitutes a significant background to the ν_e appearance measurement. This, along with other inclusive and exclusive cross-section measurements, is achieved by the fine segmentation and particle tracking and identification capabilities of ND280's subdetectors. A two-dimensional cross section of a typical muon event highlighting these capabilities is shown in 2.10.

2.4.1 π^0 Detector

The π^0 Detector (P0D) [49] is situated at the most upstream position of all of the off-axis suite's detectors, and the active element of the detector consists of a collection of 40 individual modules (P0Dules). These modules are interstitially placed with either water bags and brass plates in the target regions of the detector, or lead plates in the calorimetric regions of the detector. This scheme is illustrated in Figure 2.11.

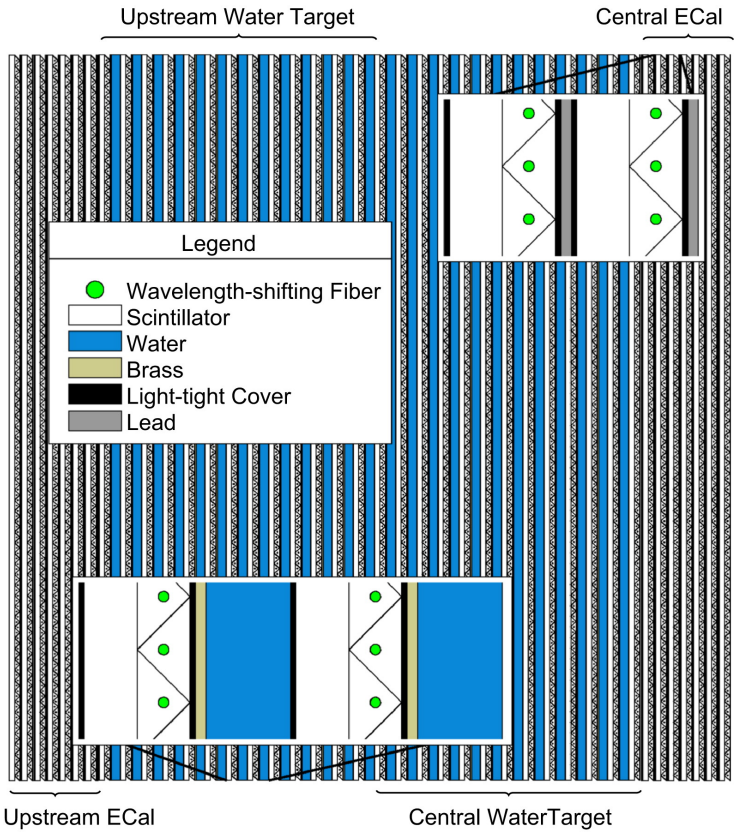

Figure 2.11: Schematic X-Y cross section of the P0D. [49]

Every P0Dule, an example of which is depicted in Figure 2.12, contains a sandwich of two perpendicularly oriented layers of plastic scintillator, and each layer is composed of an array of extruded scintillator bars with triangular cross-section dimensions of 17mm $\times$ 33mm (height $\times$ width). Each bar is individually threaded with a length of wavelength shifting (WLS) fibre, and each fibre is instrumented on one end with a Hamamatsu Multi-Photon Pixel counter [50] (MPPC), with a reflective coating applied to the uninstrumented end.

Figure 2.12: View of the installed P0D from beneath. [48]

The P0D consists of four regions, namely the "Upstream ECAL", "Upstream Water Target", "Central Water Target" and "Central ECAL", in order of increasing displacement along the beam direction. The ECAL regions ensure that any showering particles from π^0 decay in the detector are contained, as well as serving as a veto for events which originate from outside of the P0D's active volume. The central target region of the P0D contains scintillator modules and water bags placed in an alternating sequence, and the detector has the ability to run with or without the water bags filled.

The primary role of the P0D is to determine the rate of neutral current π^0 (NCπ^0) production on water near the neutrino beam's production target, as neutrino events which produce a π^0 are the dominant background to the ν_e appearance measurement at Super-K. The NCπ^0 production rate on water in the P0D is calculated by collecting data with the detector's water bags in both "full" and "empty" states, and then performing a statistical subtraction of one dataset from the other.

The P0D is also capable of measuring the intrinsic ν_e component of the ν_μ beam, which is an important background to any ν_e appearance measurement.

2.4.2 Time Projection Chamber

The Time Projection Chamber (TPC) [51] forms a significant proportion of the volume of the ND280 tracker. It is situated downstream of the P0D, and consists of a total of three rectangular modules. Each TPC module is composed of two gas-tight volumes, one encasing the other as shown in Figure 2.13.

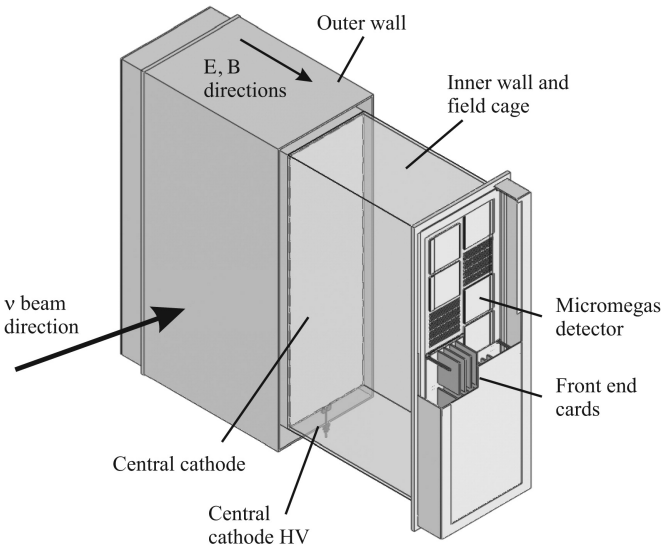

Figure 2.13: Cut-away diagram of a TPC module [51]

The outer volume is made of a mix of aluminium and aluminium/rohacell laminates, and serves as the electrical ground for the drift chamber. The inner and outer volumes are kept electrically insulated by the presence of carbon dioxide in the outer volume.

The inner volume is constructed from a mix of G10 and G10/rohacell copper-clad laminates, with the walls of the inner volume serving as the field cage of the detector. The panels of the inner volume are precisely machined to the end of producing a uniform electric field in the drift volume, this is achieved by machining a copper strip pattern with a pitch of 11.5mm. The central cathode splits the inner volume into two equal volumes, and the volume is filled with a gas mixture consisting of mostly Argon (95%), with smaller concentrations of tetrafluoromethane (3%) and isobutane (2%). The drift volume is instrumented with an array of 12 micromegas [52] modules on each end, parallel to the plane of the central cathode.

The functionality of the TPC is exploited in three vital areas of reconstruction at ND280. Namely, the accurate imaging of charged particle tracks in the drift volume, the measurement of the momenta of charged particles from their reconstructed trajectories and the identification of particles from a measurement of the energy they deposit in the detector.

A charged particle trajectory in the detector is reconstructed from the localised ionisation of the TPC gas as the particle traverses the active volume. Electrons liberated in the ionisation process drift toward and subsequently impinge upon the micromegas readout planes, at which point the signal is amplified and read-out. The positions at which the drift electrons arrive on the readout planes constitute a 2-dimensional projection of the track, which combined with the arrival of the signals in time provides the complete 3-dimensional track.

The fact that the tracking region is permeated by a magnetic field from the UA1 solenoid, coupled with accurate reconstruction of particle trajectories, allows the momenta of charged particles to be re-

constructed by considering their track curvature, which is a vital contribution to the power of the near detector to reconstruct the beam neutrino energy spectrum, particularly in the case of simple neutrino interaction topologies.

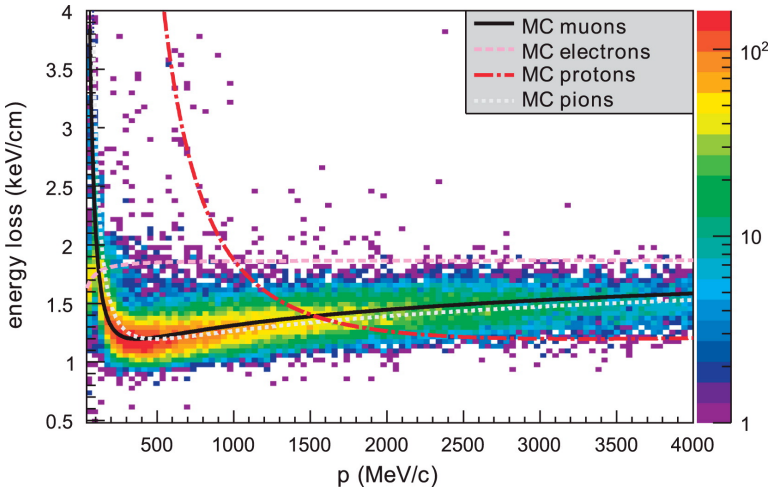

Figure 2.14: Reconstructed energy loss of negatively charged particles from neutrino interactions as a function of momentum [51]

Finally, particle identification is performed by a measurement of the energy loss of track as it traverses the detector. This information, combined with the measurement of the particle's momentum, can be used to determine the particle's identity. The distribution of energy loss as a function of particle momentum for a number of particle types in ND280 simulation is shown in Figure 2.14, along with the corresponding energy loss prediction of the Bethe-Bloch [39] formula.

2.4.3 Fine Grained Detector

The Fine Grained Detector (FGD) [53] makes up the target mass of the ND280 tracker, and consists of two separate modules, each of external dimensions 2300mm $\times$ 2400mm $\times$ 365mm (width $\times$ height $\times$ depth), as shown in Figure 2.15.

The active volume of first FGD is composed entirely of extruded polystyrene scintillator. A total of 5760 scintillator bars are arranged into "XY modules", and each "XY module" contains two layers of scintillator, with one layer arranged perpendicularly to the other, and with both layers perpendicular to the beam direction. Each scintillator bar has a square cross section of side 9.6mm, is threaded with a WLS fibre, each fibre is instrumented on one end with an MPPC and mirrored with a coating of aluminium on the other, as depicted in Figure 2.16.

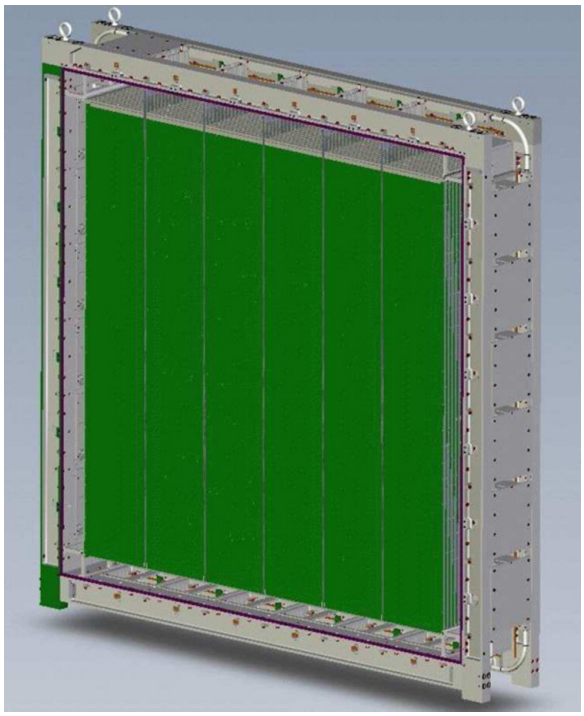

Figure 2.15: Schematic view of a full FGD module with the front cover removed. [42]

The second FGD is composed of a mix of extruded polystyrene scintillator and water. The scintillator component consists of 2688 bars, contained in seven "XY modules", and the water component is made up of six 2.5cm thick layers of water. The water layer is made from 2.5cm thick sheets of thin-walled hollow corrugated polycarbonate, the ends of which are sealed.

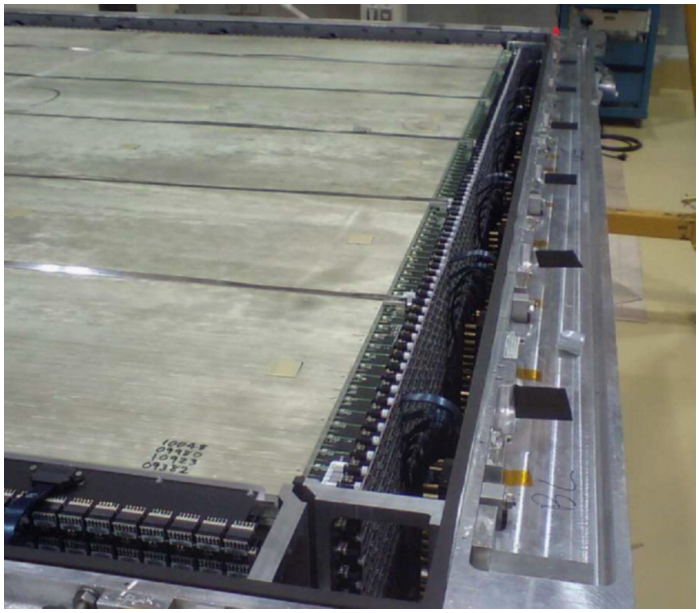

Figure 2.16: Inside an FGD dark box, scintillator and electronics readout visible [53]

The FGD's primary role is to provide the target mass for neutrino interactions at the ND280 off-axis detector, while simultaneously satisfying the requirement that the by-products of the neutrino interac-

tion reach the TPC, such that their momenta and electric charge can be determined. The fine-grained segmentation of the active volume also allows the reconstruction of the particles at the neutrino interaction vertex, which is important in distinguishing the type of neutrino interaction. Understanding the rates of these interactions before the beam oscillates is an important task in making predictions of similar quantities at Super-Kamiokande. This effort is further assisted by the FGD's ability to provide data on neutrino interaction rates on water as well as on scintillator, and is accomplished by comparing calculated rates between FGD1 and FGD2.

2.4.4 Electromagnetic Calorimeter

The Electromagnetic Calorimeter (ECAL) [54] [55] surrounds both the P0D and the ND280 tracker in a bid to provide near hermetic calorimetric coverage of the inner detectors, and is conventionally split into three sections: the P0D ECAL, the Barrel ECAL and the Downstream ECAL, the specifications of each module category are shown in Table 2.1.

Each of the ECAL's 13 constituent modules are lead-scintillator sampling calorimeters, using layers of extruded polystyrene scintillator bars as the active material. Alternating layers of lead sheets between scintillator layers provide the material in which electromagnetic showers develop. Each scintillator bar in a layer is threaded with a WLS fibre, and each fibre is either instrumented on both ends with an MPPC, or instrumented on one end and mirrored with a vacuum deposition of aluminium on the other, depending on the module type. The MPPCs are connected via coaxial cable to TFBs for the purpose of electronic readout.

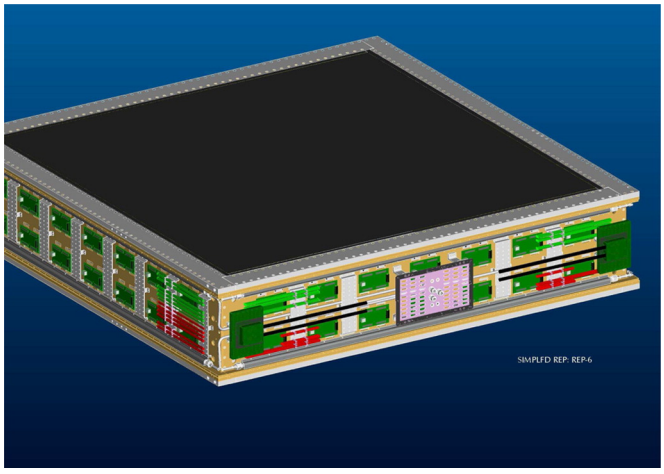

Figure 2.17: Engineering drawing of the Downstream ECAL, with light tight veneers removed[42].

The P0D ECAL is composed of a total of six modules, arranged around the P0D. There are two distinct types of P0D ECAL module and each consists of 6 active layers, with a lead sheet thickness of 4mm for each layer, providing approximately 4.3 radiation lengths (X_0) of material. The scintillator bars in each module are all oriented parallel to the direction of the beam, and their electronics readout is single-ended.

Module Type	External Dimensions (mm)	No. Bars per Layer	Weight (kg)
P0D Top or Bottom	$2454 \times 1584 \times 155$	38	1500
P0D Side	$2454 \times 2898 \times 155$	69	3000
Barrel Top or Bottom	$4140 \times 1676 \times 462$	38 Long $\times$ 96 Perp	8000
Barrel Side	$4140 \times 2500 \times 462$	57 Long $\times$ 96 Perp	10000
Downstream	$2300 \times 2300 \times 500$	50	6500

Table 2.1: ECAL module specifications [54]. "Long" denotes bar orientation parallel to the beam direction, "Perp" denotes perpendicular.

The Barrel and Downstream ECALs surround the ND280 tracker, and are commonly referred to as the Tracker ECAL. The Barrel ECAL comprises six modules placed around the ND280 tracker, and again comes in two types. All of the Barrel modules contain 31 layers, and each layer's lead sheet has thickness 1.75mm, which corresponds to approximately $10X_0$ of material. The Downstream ECAL, depicted in Figure 2.17, is situated at the end of the inner detector basket, and is the most downstream of all ND280's detectors. It contains 34 layers, each hosting a lead sheet of thickness 1.75mm, providing approximately $11X_0$ of material. The Barrel ECAL contains scintillator bars which employ both single-ended and double-ended readout, whereas the Downstream employs double-ended readout only.

The main function of the ND280 ECAL is to ensure that electrons, positrons and γs exiting the P0D or tracker are detected. This is of particular importance for the reconstruction of π^0s, a case in which decay products of the parent particle are electrically neutral, and thus are only detectable by their subsequent electromagnetic shower in a suitably dense material. Both the Barrel and Downstream ECALs are capable of measuring the development of tracks and electromagnetic showers in three dimensions, by virtue of successive and mutually perpendicular stacking of scintillator bar orientations. The P0D ECAL is capable only of two dimensional reconstruction of energy deposits, as its scintillator layers are successively aligned in parallel.

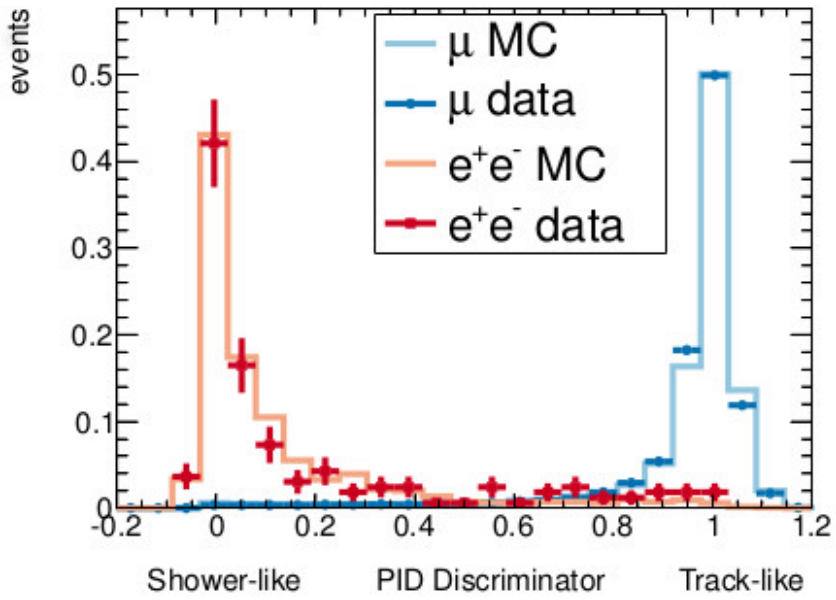

Figure 2.18: Demonstration of ECAL PID ability in the case of electron/muon discrimination [54]

The ECAL is also capable of complementing the particle identification power of the TPC (as shown in Figure 2.18), performing well in the case of track/shower discrimination due to the distinct signatures these types of particle leave in the detector.

2.4.5 UA1 Magnet and Side Muon Range Detector

The former UA1/NOMAD magnet [56] was donated by CERN and refurbished to provide a magnetic field for ND280 off-axis detector. It consists of a set of aluminium coils and 16 flux return yokes, which together encase the inner detectors and provide the 0.2T magnetic field, as shown in Figure 2.19, required for the determination of the charge and momenta of particles.

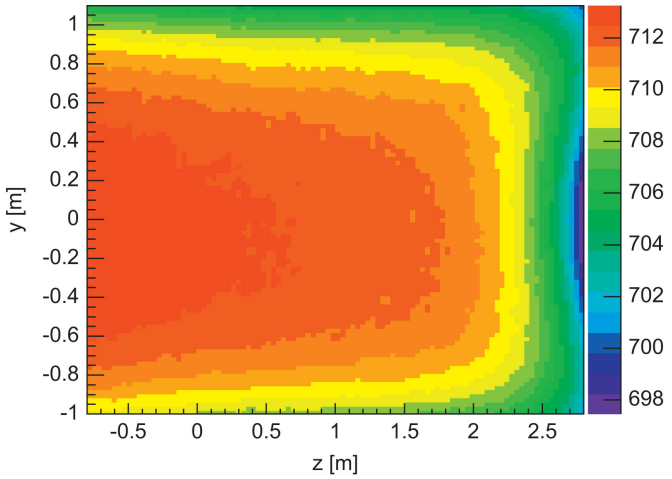

Figure 2.19: Magnetic field flux inside ND280 [56]

The magnet is assembled in two separate symmetric pieces, and each symmetric piece consists of 8 C-shaped magnet yokes (depicted in Figure 2.20) and two aluminium coils. Each piece is mounted on rails which allow the magnet to open and close around the inner detectors as needed. The exterior dimensions of the magnet are 7.6m $\times$ 5.6m $\times$ 6.1m, with the yoke weighing in at 850 tons.

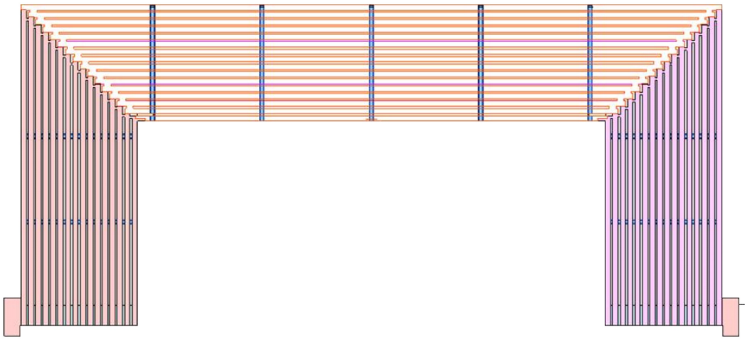

Figure 2.20: Engineering drawing of a single magnet yoke, rotated 90 degrees[56]

The Side Muon Range Detector (SMRD) [56] is housed within the UA1 magnet, and consists of a total of 440 detector modules placed in the gaps between the magnet's flux return yokes. The dimensions of the modules are chosen to correspond to the physical dimensions of the gaps in the magnet yoke, and there are two module types, corresponding to two orientations (horizontal and vertical). Each module type contains a number of scintillation counters, the number and dimensions of which depend on the intended orientation and are set out in Table 2.2.

Orientation	No. Modules	Counter dimensions	No. Counters per Module
Horizontal	192	7mm $\times$ 167mm $\times$ 875mm	4
Vertical	248	7mm $\times$ 175mm $\times$ 875mm	5

Table 2.2: SMRD module dimensions [56].

The active component of the SMRD counter consists of a slab of extruded polystyrene scintillator which houses a WLS fibre, depicted in Figure 2.21. The fibre is embedded within the slab in a sinuous groove, which is purposefully milled into the scintillator during manufacturing. The fibre is read out on each of its ends by an MPPC, which is seated on an end-cap to ensure good coupling between the fibre's ferrule and the photodetector.

The primary role of the SMRD is to assist in the reconstruction of the momenta and direction of muons produced in CCQE neutrino interactions which originate in the ND280 tracker. Many of the measurements made by ND280 depend on being able to efficiently reconstruct the energy of the incoming neutrino which, in CCQE interactions, is a function of the momentum and direction of the outgoing lepton.

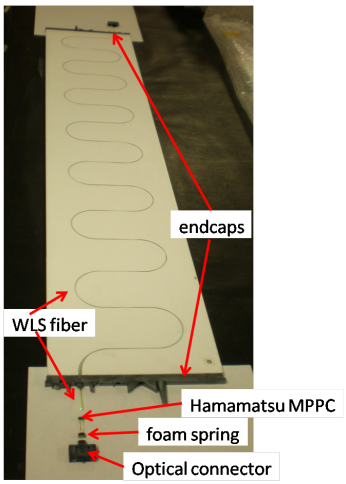

Figure 2.21: Assembled SMRD counter without light-tighting [48].

Reconstruction of these quantities from tracker data alone can be problematic if, for example, the trajectory of an outgoing muon deviates significantly from the beam direction, in which instance the muon leaves little signature of its passing in the tracking region. It is in these cases that the SMRD, in conjunction with the ECAL, can provide information which would otherwise be missing. The trajectory of the muon can be determined from the reconstructed position of scintillator hits in both the ECAL and the SMRD, and the momentum can be inferred by considering the range of the detected track as it has traversed successive iron plates of the magnet yoke.

The SMRD also plays a significant part in both the calibration of ND280's sub-detectors and the identification of background neutrino interactions from the magnet. As the entire magnet is instrumented with the SMRD, it is ideally suited to serve as a trigger for through-going events which originate from outside of ND280. This fact is extensively exploited to provide a large amount of MIP-like cosmic ray muons for inner detector calibration by requiring coincidence of a signal in both the top and bottom segments of the SMRD, outside of a beam spill window.

2.5 Far Detector: Super-Kamiokande

Super-Kamiokande (Super-K) [57] is T2K's far detector, and with a net mass of 50 kilotons is the world's largest water Čerenkov detector. The facility is located 1km under Mount Ikenoyama, 295km west of J-PARC, and consists of a cylindrical welded stainless steel tank with a capacity of 50kt of water.

The main detector volume is split into two separate detector volumes, an "inner detector" and an "outer detector", as depicted in Figure 2.22. The inner detector comprises a 33.8m $\times$ 36.2m (diameter $\times$ height) cylindrical volume, the inner walls of which are affixed with 11,129 inward-facing photo-multiplier tubes (PMTs). The outer detector envelops the inner detector, and is a cylindrical space of radial thickness 2m instrumented with 1,885 outward-facing PMTs. The inner detector constitutes the target mass for neutrino interactions from the T2K beam, and the outer detector permits events that originate from outside of Super-K to be vetoed.

The main purpose of Super-K in the T2K experiment is to measure the energy spectrum and flavour composition of the neutrino beam after it has traversed the length of Japan from J-PARC. Indirect detection of neutrinos at Super-K is performed by searching for the signature of final state charged particles from interactions within the inner detector volume. In the case of CCQE neutrino interactions, this involves the detection of the lepton produced at the interaction vertex, and corresponds to the parent neutrino flavour.

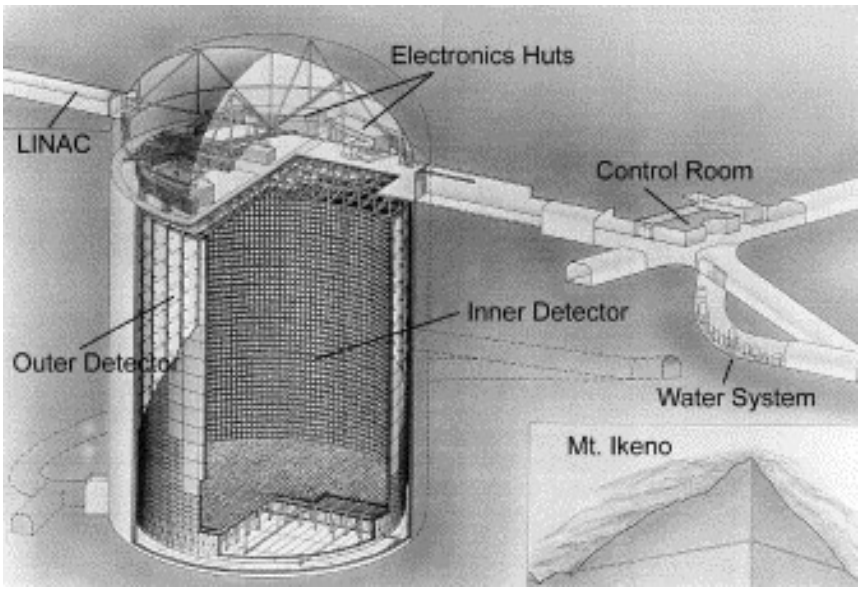

Figure 2.22: The Super-K far detector[57].

As charged particles traverse a dielectric medium, the constituent electrons and atoms of the material become disrupted and polarised. If the velocity of the charged particle exceeds the phase velocity of light in that medium, photons emitted in the depolarisation process form coherent wavefronts which are commonly referred to as Čerenkov radiation. These wavefronts form a cone whose opening angle is a function of the charged particle's velocity and the refractive index of the medium, the relationship between these quantities is shown in Equation 2.1.

$$\cos\theta = \frac{1}{\beta n} \tag{2.1}$$

Super-K uses the Čerenkov radiation emitted in the passing of charged particles by detecting the rings of light projected onto the detector walls in this process using PMTs. Particle identification is be achieved by considering the distortion of the imaged ring. Electrons, depending on their momentum, undergo multiple scattering or participate in electromagnetic showers. These processes alter the momentum of the particle and even produce new particles, each of which can also produce their own Čerenkov radiation. The result is a set of superimposed Čerenkov rings which manifests as a "fuzzy" single ring, as shown in Figure 2.23. Conversely, muons undergo very little scattering by virtue of their large mass, and therefore produce sharp rings. Finally, the diameter of the projected rings allows the

momentum of the charged particle to be determined.

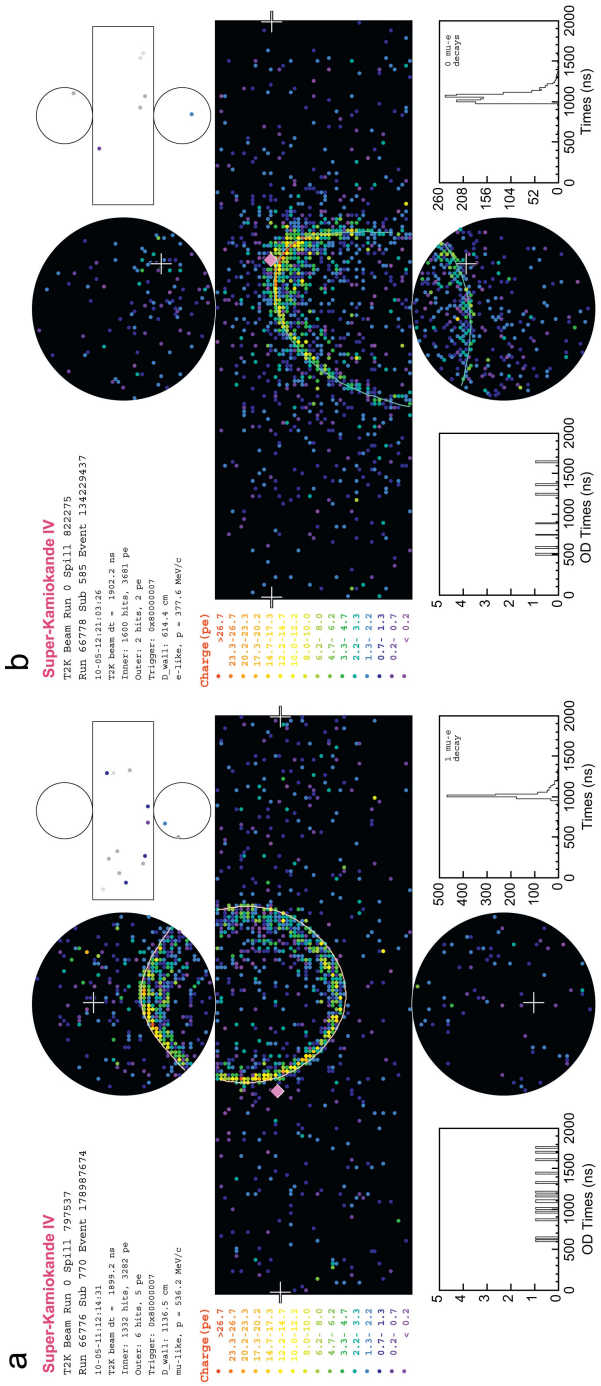

Figure 2.23: Super-K event display, case a) (bottom) showing a clear muon-like ring, and case b) (top) showing a distorted electron-like ring. Each coloured pixel corresponds to a PMT [42].

A proposed upgrade to Super-K (named Hyper-K [58]) aims to utilise a 1 million ton water target (over 20x that of Super-K) to continue improving the sensitivity of proton decay searches, as well as improving measurements of neutrino oscillation parameters, CP violation and exploring the mass hierarchy, utilising neutrinos from both accelerator and atmospheric sources.

Chapter 3

Construction and Operation of Barrel ECAL

The Barrel Electromagnetic Calorimeter (Barrel ECAL) [54] consists of a total of 6 separate modules, mechanically supported by the UA1 magnet and arranged around the tracking region of ND280's off-axis detector suite. All six modules were designed, assembled and tested by a multi-disciplinary team across a number of academic and laboratory sites in the UK, with the final assembly and testing of the modules taking place both at Daresbury Laboratory and the University of Liverpool. The modules were individually shipped to J-PARC for installation and commissioning as they were completed.

Construction of the Barrel ECAL commenced in the summer of 2009, and was concluded with the completion and shipping of all six modules by winter 2010. The Barrel ECAL, along with the rest of ND280, has performed well since its installation, despite nature's inclination to put its mechanical and electrical robustness to the test with a series of significant seismic events, including (but not confined to) being in the vicinity of the fourth largest earthquake on record since 1900.

3.1 Detector Instrumentation and Readout

The ECAL, like many of ND280's subdetectors, employs Multi-Pixel Photon Counters [50] (MPPCs) for photodetectors and Trip-T [59] based electronics for readout. The specifications of each are briefly higlighted.

3.1.1 Multi-Pixel Photon Counter

The Hamamatsu MPPC was selected for use in ND280's subdetectors on the basis of a number of criteria. Firstly, the photodetectors must be compact as the near detector contains as many as 56,000 readout channels. It must have good photon detection efficiency, it must also be insensitive to magnetic fields, as ND280 is bathed in a 0.2T field for the purposes of aiding particle reconstruction, and finally it must be cheap. The MPPC itself consists of a grid of "pixels", each of which is an avalanche photo-diode operating in Geiger mode, as depicted in Figure 3.1. Each MPPC consists of 667 pixels in a 1.3 $\times$ 1.3mm^2 array, and the MPPC gain is determined by the charge accumulated in an individual pixel

capacitance, given by $Q_{\text{pixel}} = C_{\text{pixel}}\Delta V$.

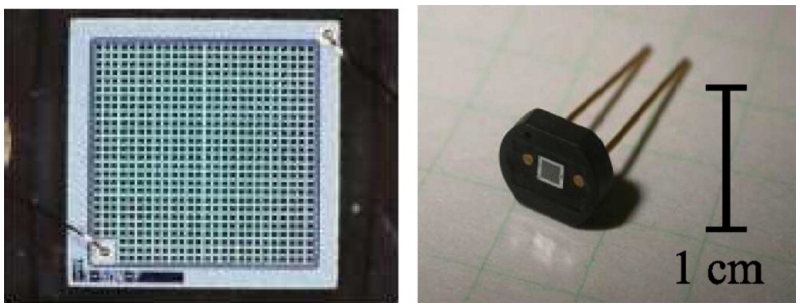

Figure 3.1: An MPPC, showing the grid of photodiode pixels to the left and its approximate scale to the right [42].

Photons impinging on an MPPC pixel create photoelectrons which then initiate a Geiger avalanche, and the signal is the sum of all of the individual fired pixels, which is proportional to the number of individually fired pixels. Photodetector noise comes in the form of crosstalk and dark current, crosstalk occurs when photons are emitted during a nearby Geiger avalanche, triggering another avalanche in a nearby pixel. The origin of the dark current is the initiation of avalanches from random thermal activity within the photodetector, which is random.

3.1.2 Trip-T Frontend Board

The Trip-T Frontend Board (TFB) serves as the interface between the MPPCs and the upstream Readout Merger Module (RMM), and houses 64 channels serviced by 4 Trip-T ASICs. The MPPC readout charges are split between high and low gain channels capacitively in the ratio of 1:10, and is then integrated in programmable windows (in the case of T2K, the windows are programmed to coincide with beam spills from the GPS trigger). The chip can hold 23 integration cycles at any one time, and once saturated the data is digitised by ADCs. The entire board is controlled by a central FPGA which assembles digitised and timestamps the data before sending it to the RMM to be buffered. The TFB also provides temperature information from attached sensors and provides output from discriminators which can be used to calculate trigger primitives.

3.2 Detector Materials

The Barrel ECAL modules all share the same construction materials, with only the physical design and dimensions of each module and its components differing depending on their intended position within the ND280 detector suite.

3.2.1 Scintillator Bars

The ECAL scintillator bars were manufactured at the Fermi National Accelerator Laboratory (FNAL) to specifications previously used by the MINOS experiment [60], and serve as the active material of each module. Each bar consists of extruded polystyrene doped with small proportions of two distinct organic scintillators. The primary dopant at the level of 1% is PPO, which provides a scintillation mechanism

in which charged particles participate. The secondary dopant at the level of 0.03% is POPOP, facilitates a shift in the wavelength of scintillation light. Each bar is also covered in a layer of polystyrene co-extruded with titanium dioxide, the purpose of which is to reflect incident light, ensuring that each bar is optically isolated from its external environment and other nearby bars, while keeping light generated within the bar contained by reflection.

3.2.2 Wavelength Shifting Fibre

Each scintillator bar is threaded with a length of optic fibre in a bid to facilitate the absorption, transmission and subsequent detection of light created by the interaction of charged particles with the scintillating medium as they traverse the ECAL's active volume. A total in excess of 17,000 of multi-clad Kuraray Y-11(200)M, CS-35J fibres were cut to length, ice-polished and treated at FNAL before being delivered to Liverpool University and Daresbury Laboratory for installation. The fibres intended for use in single-ended readout channels were coated on one end in aluminium by a vacuum deposition process to the end of reflecting collected scintillation light back to the instrumented end of the fibre, thereby minimising signal loss in signal ended readout channels.

3.2.3 Lead

The Barrel ECAL employs 2% Sb-stiffened lead as the target, radiative material in its sampling calorimeter configuration. The material is provided in the form of black, metal-conditioning primer coated lead sheets of thickness 1.75mm, each smaller than any given layer of scintillator bars, intended to be contiguously placed and glued directly to the frame and scintillator.

3.3 Construction Procedure

Construction of the larger side barrel modules took place at Daresbury Laboratory, where the manufacture and subsequent installation of individual layers took place concurrently. Construction of the smaller top and bottom modules was carried out at Liverpool University, where layers were delivered in bulk following their manufacture at Lancaster University.

3.3.1 Individual Layer Assembly

Each layer consists of a frame, a number of scintillator bars and a number of lead sheets. The frame is composed of machined aluminium, and each length of frame contains a sequence of holes, each of diameter 2mm. After the frame is affixed to a working surface, scintillator bars are individually inserted into the structure having been treated with adhesive along one of their edges, such that the WLS fibre hole on each end of the bar corresponds to one of the 2mm holes in the aluminium frame. Each scintillator bar hole is temporarily sealed with an O-ring and locator pin throughout the process of applying the adhesive to ensure that it remains unobstructed.

Once all of the layers are in place, a number of lead sheets are measured and cut to the required

size. An additional strip of adhesive is then applied both around the perimeter of the frame and to the top surface of the scintillator bars, upon which the lead layers are slowly placed with the aid of a crane and a vacuum lifter as shown in Figure 3.2.

Figure 3.2: Lead layers being affixed with adhesive to plastic scintillator at Daresbury Laboratory

Once the lead layers are in place, the entire layer is covered and sealed in plastic, vacuum pumps are placed at four positions around the surface of the layer and the adhesive is left to cure overnight under vacuum compression. Upon completion of this process, the layer is ready to be installed into a module.

3.3.2 Module Frame Assembly

Every module is mounted on a transport frame to which a robotic scanning mechanism is also attached, as shown in Figure 3.3. The main frame of each detector consists of a carbon-fibre base panel and three load bearing stainless steel bulkheads.

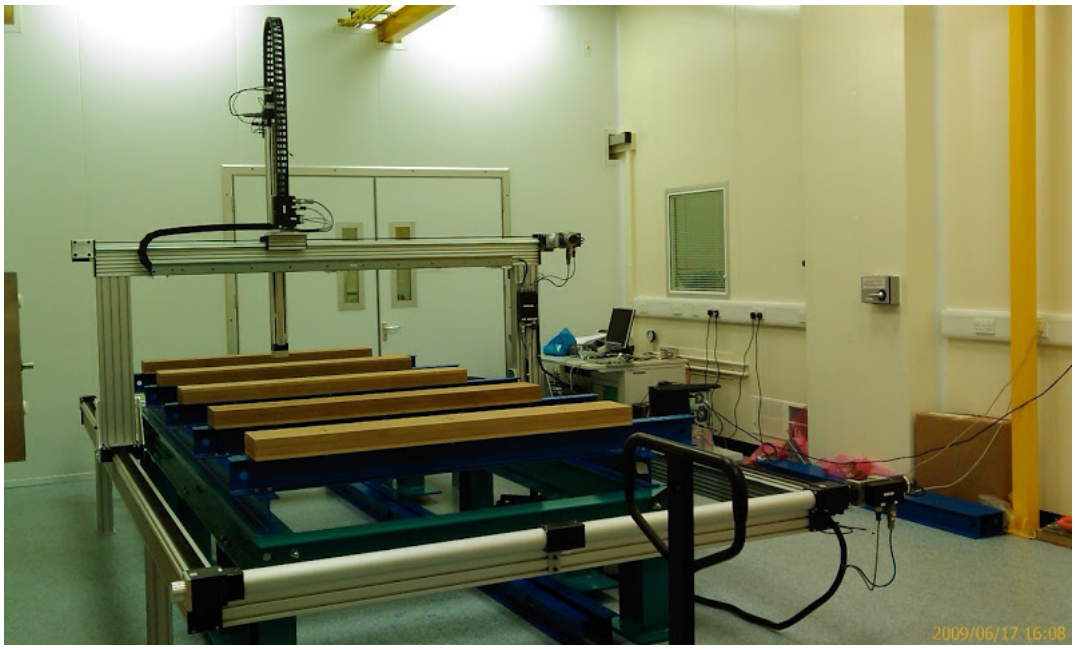

Figure 3.3: Transport frame with robotic scanning mechanism attached

The carbon-fibre base panel is attached to the transport frame and each of the three bulkheads is affixed to the base, at which point a first layer is placed (as illustrated in Figure 3.4) in order to allow for the installation of the light injection system, as well as the calibration of the robotic scanning mechanism.

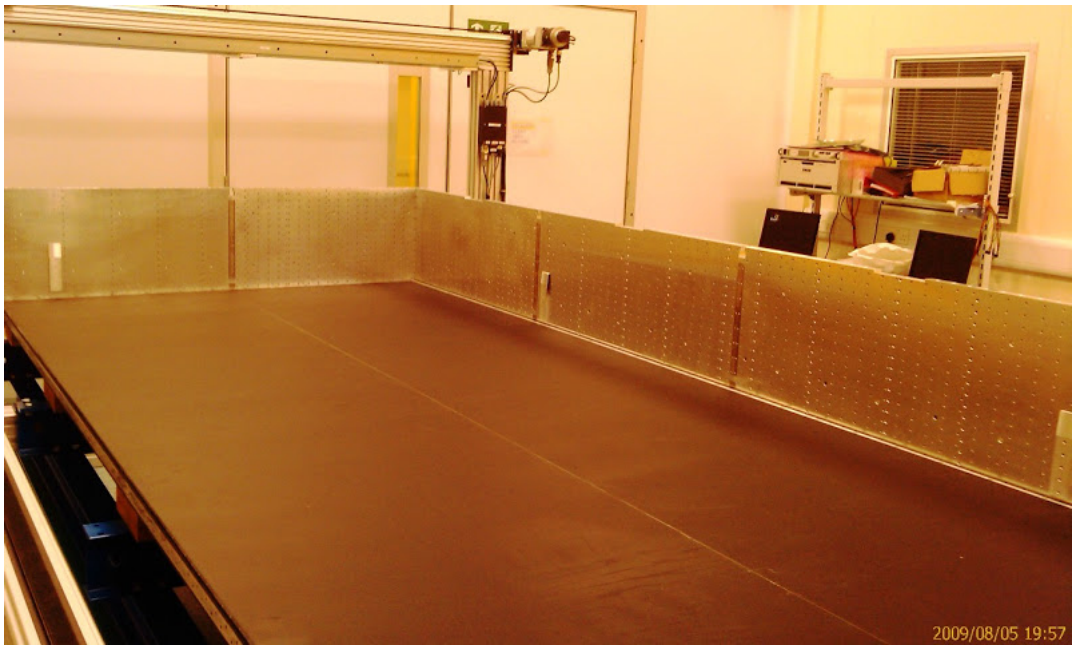

Figure 3.4: An ECAL module with bulkheads assembled and first layer installed.

3.3.3 Layer Installation and Instrumentation

With the exception of the first layer, each layer is attached to the one directly beneath it by a set of screws located around the layer's aluminium frame. As the number of installed layers increases, the overall deflection of the layer is considered by surveying the the surface of the lead layer with the aid of the robotic scanning apparatus. Sheets of rohacell encased in a thin plastic are sandwiched between subsequent layers to the end of offsetting any deviation of the expected position of the layers.

Each scintillator bar in each layer is threaded with a length of WLS fibre appropriate to the layer's bar readout configuration. An interfacing polymer tube is inserted through the bulkhead fibre hole into the scintillator bar aperture in order to ensure that the fibres are not scratched as they are threaded through the bulkhead, as shown in Figure 3.5.

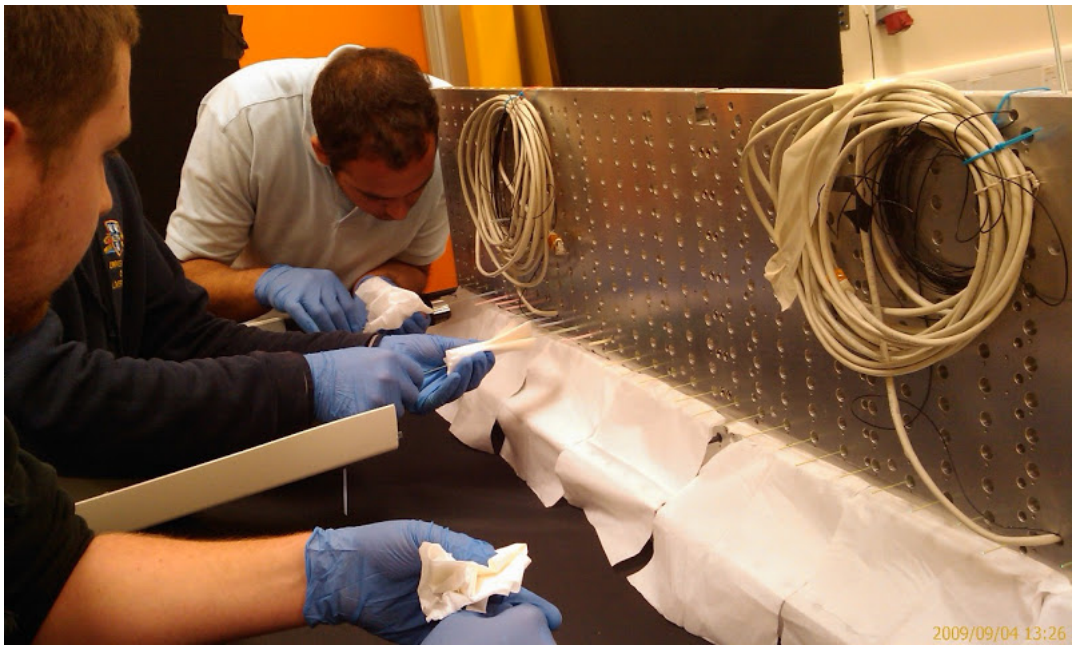

Figure 3.5: Workers carefully threading WLS fibres with the aid of advanced organic polymer based guidance equipment.

Every WLS fibre requires a ferrule which serves to optically couple the MPPC to the fibre's end. In the case of a single-ended readout layer, each WLS fibre comes with a ferrule already glued to the non-mirrored end, allowing the fibre to be threaded easily. However, in the double-ended readout case, the fibre must first be threaded before ferrules can be glued to both sides of the fibre. This is due to the bulkhead fibre holes being too small to thread the entire ferrule through. In this case, the ferrules are attached with the aid of a silicon-based optical epoxy resin, and must be attached to both sides simultaneously, judiciously and left to cure before the fibres can be tested.

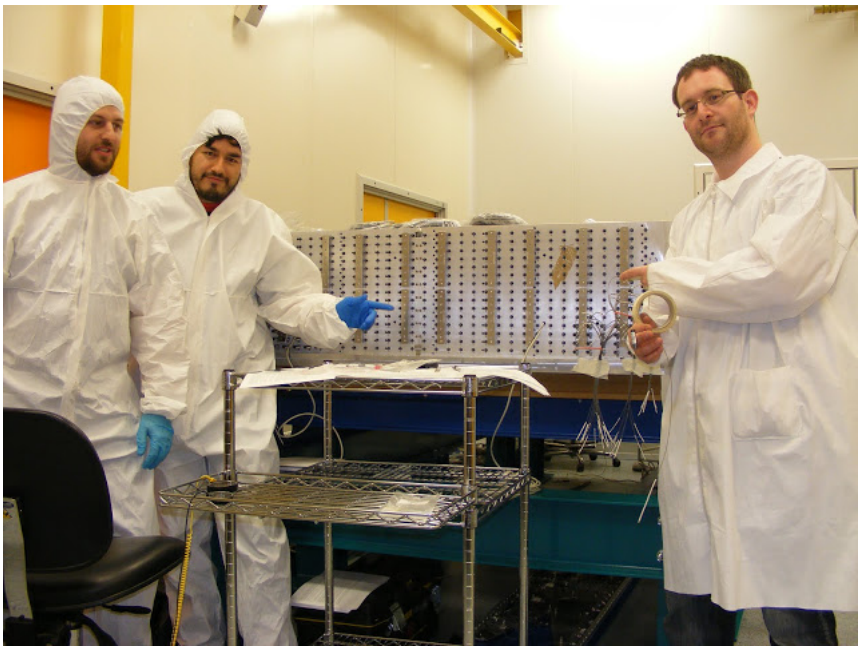

Figure 3.6: Complete set of double ended readout channels in place.

3.3.4 Layer Testing

Each installed scintillator bar is tested with the aid of a radioactive source, which is mounted on the arm of the robotic scanning apparatus. The collimated 115MBq caesium-137 (Cs-137) source is housed in a small detachable module, and in the scanner's "parked" position is held within a lead shielded container to the rear of the scanning assembly. The testing process relies on the detection of 662keV γs produced in the β decay of the Cs-137 source, and at this energy the γ cross-section on lead is dominated by Compton scattering and photoelectric processes.

Every layer is instrumented with a set of test MPPCs and is fully light tight in order to prevent saturation of any of the individual photodetectors, as shown in Figure 3.7. The scanner is configured to position the radioactive source at a set number of points along the length of each bar, and the spacing between scanning points is decreased around the ends of the bar, where edge effects are prominent.

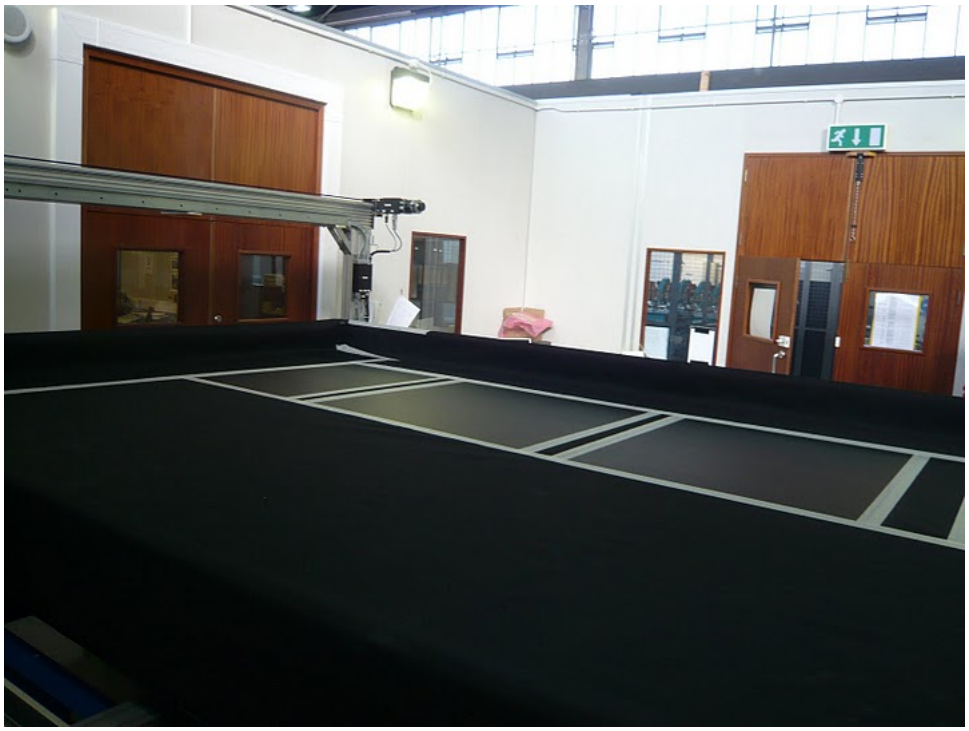

Figure 3.7: A light tight layer from one of the side modules ready to be scanned.

The scanner holds its position for a fixed amount of time for each scanning point, as shown in Figure 3.8, while the DAQ collects data and writes it to a local disk. An attenuation profile for each bar is constructed by determining the signal to background ratio as a function of the scanner's position relative to the photosensor.

Figure 3.8: Bar scanner in action at Daresbury Laboratory.

A comparison of the typical signal and background photoelectron spectra is shown in Figure 3.9. The dominant dark noise component of the photoelectron spectra, common to both the signal and background distributions, is negated in the ratio calculation by integrating beyond the fifth photoelectron

peak, after which point the dark noise rate in the background distribution becomes negligible.

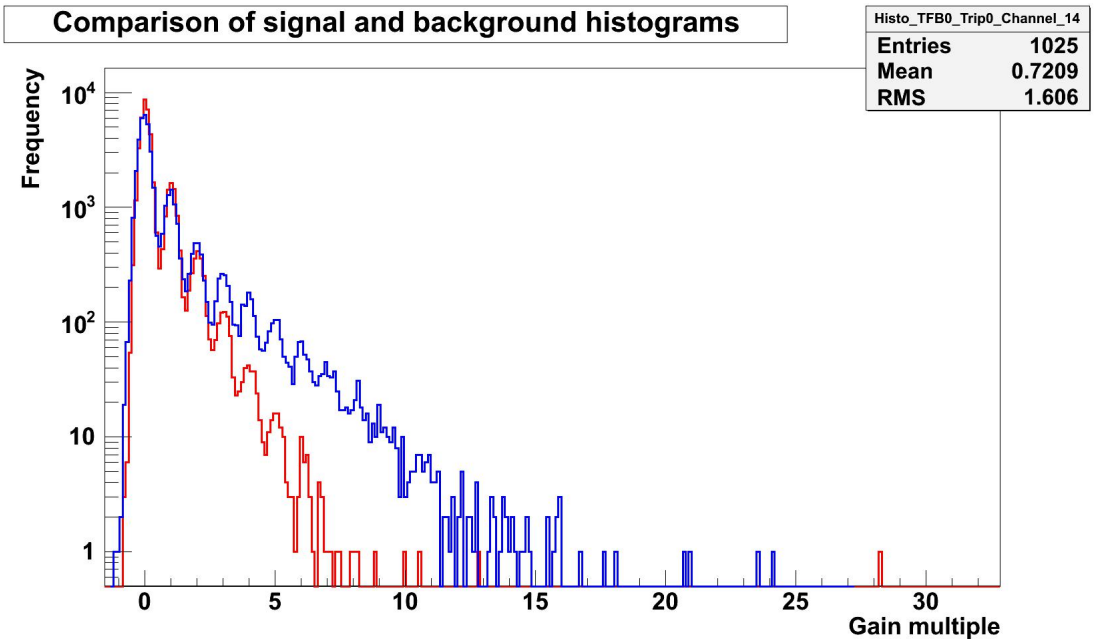

Figure 3.9: Signal and background photoelectron spectra at a single position along the length of a scintillator bar. The red histogram (background) corresponds to the data collected in the absence of a radioactive source, the blue histogram (signal) corresponds to data collected in the presence of a radioactive source.

Typical attenuation profiles for long and short bar types are illustrated in Figure 3.10 and Figure 3.11 respectively. The integrity of a fibre is determined by the result of performing an fit to the measured profile. The integrated light yield ratio in the case of good fibres is expected to fall off smoothly and exponentially as the scanner moves away from the photosensor, with a sharp drop-off around the bar's edges. Bad fibres are easily visually identified by a discontinuous drop in the light yield distribution, usually as a result of a break somewhere along the fibre's length. The fit to the attenuation profile of broken fibres also tends to be of very poor quality, and the automation of identifying these channels amongst the tens of thousands analysed throughout the process of construction was the subject of a number of master's student projects at the university. An example of a bad fibre identified by one of these methods is shown in Figure 3.12.

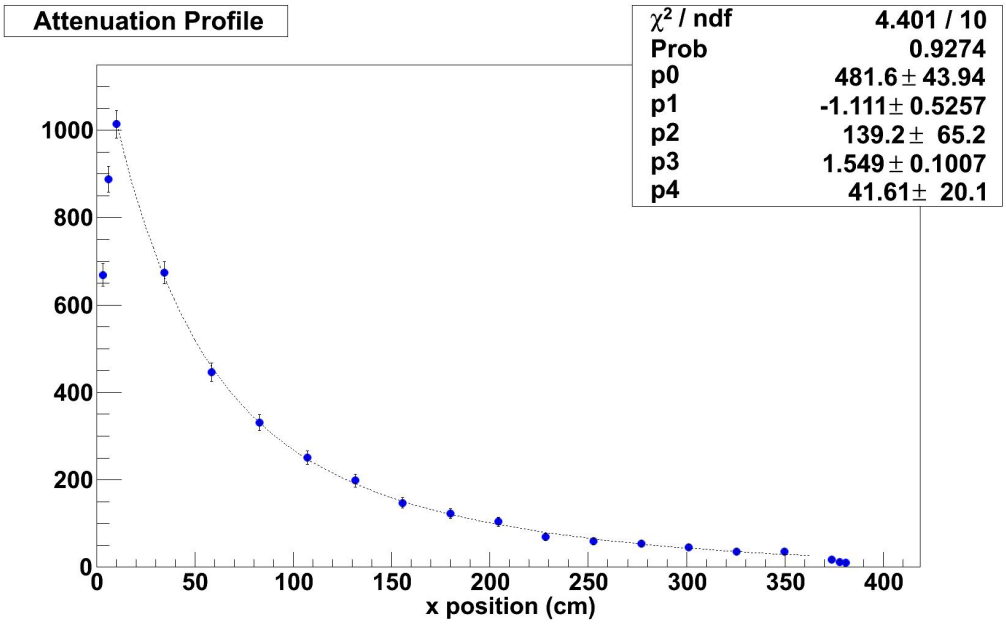

Figure 3.10: A typical attenuation profile for a long bar.

A number of improvements in the analysis of scanner data resulted in significant time savings as construction went on. Firstly, the use of the University of Liverpool's MAP2 cluster in the analysis of data from both construction sites allowed scanner data to be analysed on the fly, with analysis results often being ready at the start of the working day. The flow of data from the sites to the central processing centre is illustrated in Figure 3.13.

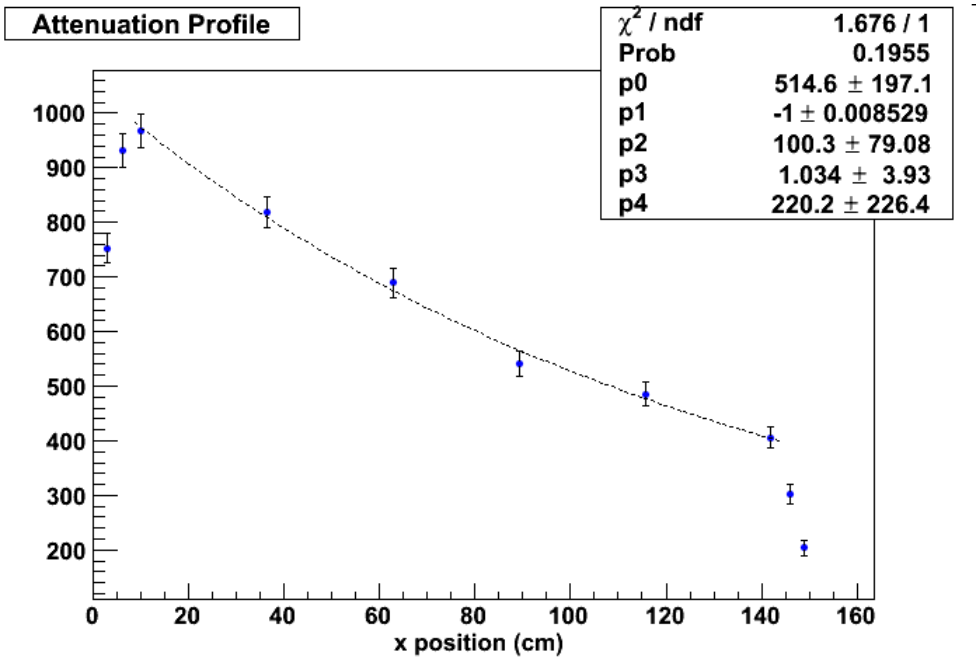

Figure 3.11: A typical attenuation profile for a short bar.

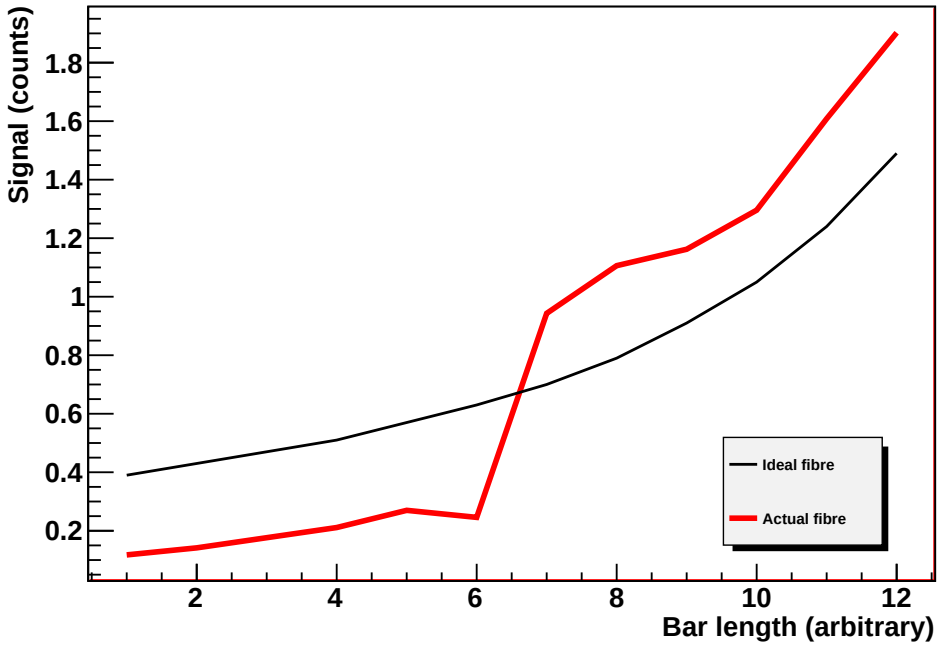

Figure 3.12: An example of a bad fibre attenuation profile compared to the reference profile constructed from a sample of good fibres [61].

Scanner data is synchronised with the MAP2 data storage as it is written to the disk at each site and subsequently analysed. Upon the completion of analysis, is archived and moved to long term storage, which was necessary due to the very large file sizes of individual layer data. The second major improvement came with the realisation that the radiation from the Cs-137 source was sufficiently energetic to penetrate multiple layers, which allowed the installation, instrumentation and testing of two layers at a time, reducing the remaining build time by a factor of a half.

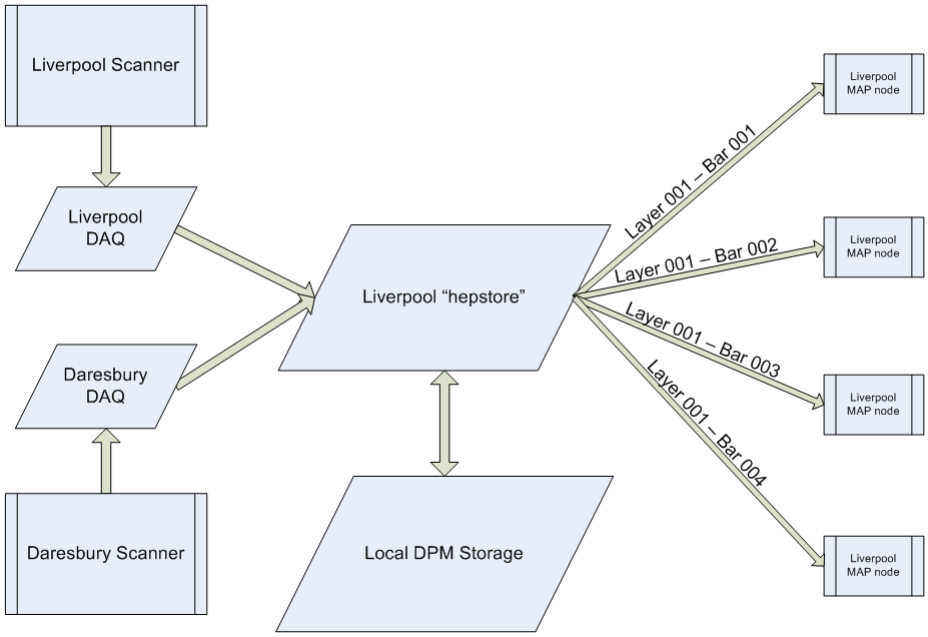

Figure 3.13: Illustration of scanner data analysis process.

3.3.5 Instrumentation

The instrumentation of the scintillator bars takes place upon the completion of the layer installation and testing process, and each scintillator bar is assigned one or two MPPCs, depending on the fibre configuration.

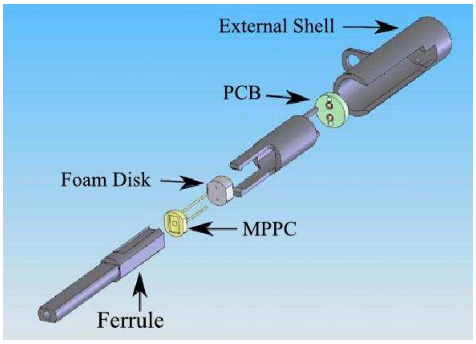

Figure 3.14: An exploded view of the housing that couples wavelength shifting fibres to the MPPC. [54]

A mini coaxial cable is attached to each MPPC, which is housed in a custom sheath (Figure 3.14), along with a foam spring, and is attached to the fibre ferrule such that the photodetector is optically coupled to the fibre's end.

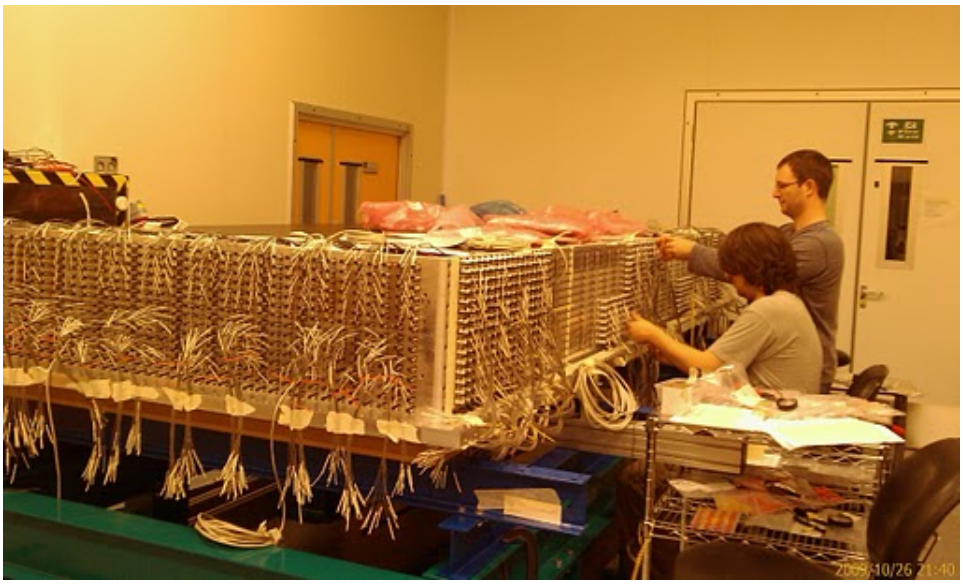

Figure 3.15: A small Barrel ECAL module in the process of being instrumented.

When all of the MPPCs are attached to their corresponding fibres, cooling plates are secured to the outer perimeter of the base plate, upon which are mounted sets of TFBs. The TFBs are screwed into the cooling plate, the Trip-T ASIC on the underside of the PCB is in contact with the plate via a thickness of thermally conducting paste, which is applied before installation. The mini-coaxial cables from each MPPC are attached to predefined channels on each TFB, as shown in Figures 3.16, 3.15. Each TFB is also equipped with LM92 temperature boards, which are screwed onto the inner bulkheads and connected to the TFB by ribbon cable.

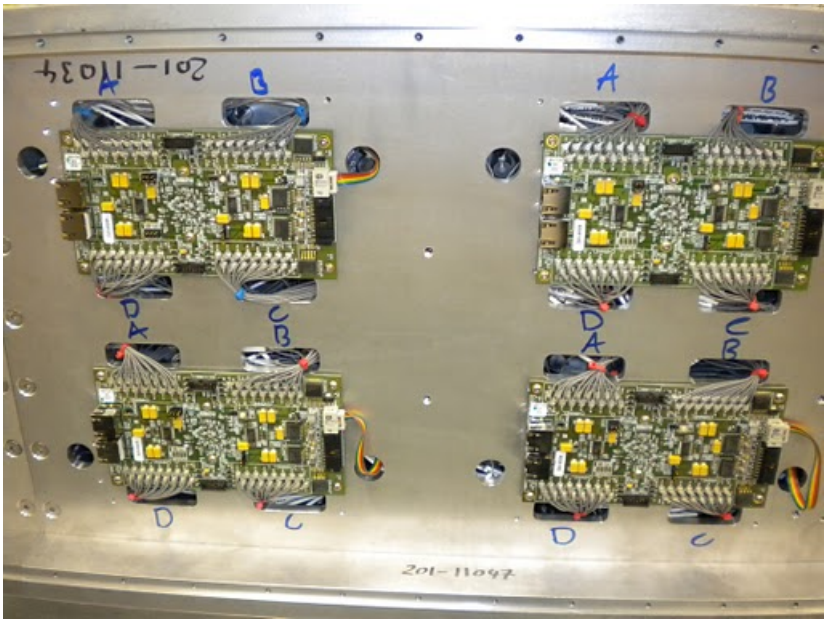

Figure 3.16: Mini-coaxial MPPC cables fully connected to TFB channels.

3.3.6 Services and Finalisation

Following the successful test of each individual TFB, the ECAL's power and cooling services are installed. Each ECAL module is furnished with a water cooling loop, which is affixed to the top and bottom of the cooling plates upon which the TFBs are attached around the detector. The constituent pipes of the loop are welded together and tested under pressure to ensure that no leaks occur during operation. Power for the MPPCs and TFBs is provided in the form of a set of individual bus bars, placed centrally around the detector and individual voltage lines are welded together, ensuring that each bus bar is continuous and electrically isolated from neighbouring bars. Each bar corresponds to an individual voltage rail, required for the TFBs to function, as well as a separate rail providing the relatively higher MPPC voltage required for their operation. Shielded category 5e Ethernet cables are crimped with RJ45 connectors on one end and connected to each TFB. As the cables are subsequently routed around the length of the detector and exit by being threaded through a patch panel, they must be each be cut to a specific length such that the length of the cables outside of the detector is approximately uniform. Once the Ethernet cables are threaded through the patch panel, the remaining end is crimped and the module is ready to be fully tested, as shown in 3.17

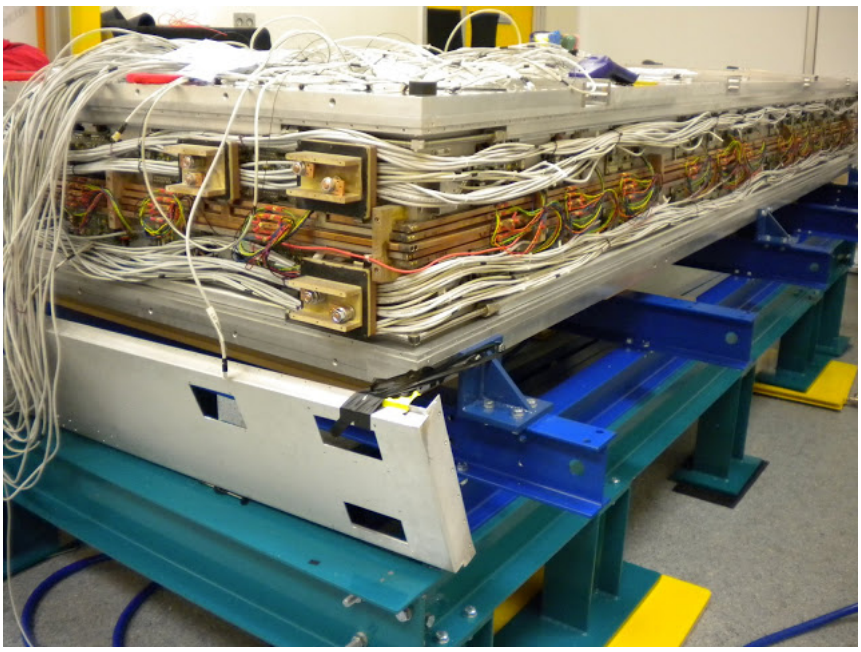

Figure 3.17: A small Barrel ECAL module with cooling pipes, bus bars and Ethernet cables attached.

The completed module undergoes overnight data-taking for the purposes of a brief burn-in test, before being packed up and loaded onto a HGV to be shipped to J-PARC (Figure 3.18). The module is tested upon arrival before being lowered into the ND280 detector pit and installed.

Figure 3.18: A completed module in preparation to be shipped.

3.4 On-site Operation

The ongoing operation and maintenance of the full ECAL during data-taking periods is facilitated by the presence of experts who work on-site at J-PARC. What follows is a brief overview of the calibration and monitoring responsibilities of an ECAL expert, as well as an explanation as to how the process was improved in some areas during the author's various stints at the facility.

3.4.1 Calibration

To ensure the quality of data collected by the ECAL, the electronics response of every installed channel needs to be carefully and frequently monitored throughout data taking periods. As previously discussed, the response of the MPPC strongly depends on its temperature, and the location of calorimeters in the detector pit makes regulation of the environmental temperature impossible, leaving the MPPCs susceptible to wide, daily variations in temperature.

The complete ECAL subsystem is instrumented with of the order of 23,000 channels, therefore automation of calibration tasks and the efficient identification of problem channels is an important priority in ensuring the reliable operation of the detector.

During data taking periods, an on-line monitoring process makes available sets of diagnostic and calibration histograms in ROOT format which can be used to determine the (almost) near time state of the detector. The accumulated hits from each MPPC are histogrammed as shown in Figure 3.19 and the resulting photoelectron spectrum is parametrised by fitting each peak in the spectrum, the results of which are used to define quantities which are useful in the normalisation of the response of all of the detector's MPPCs.

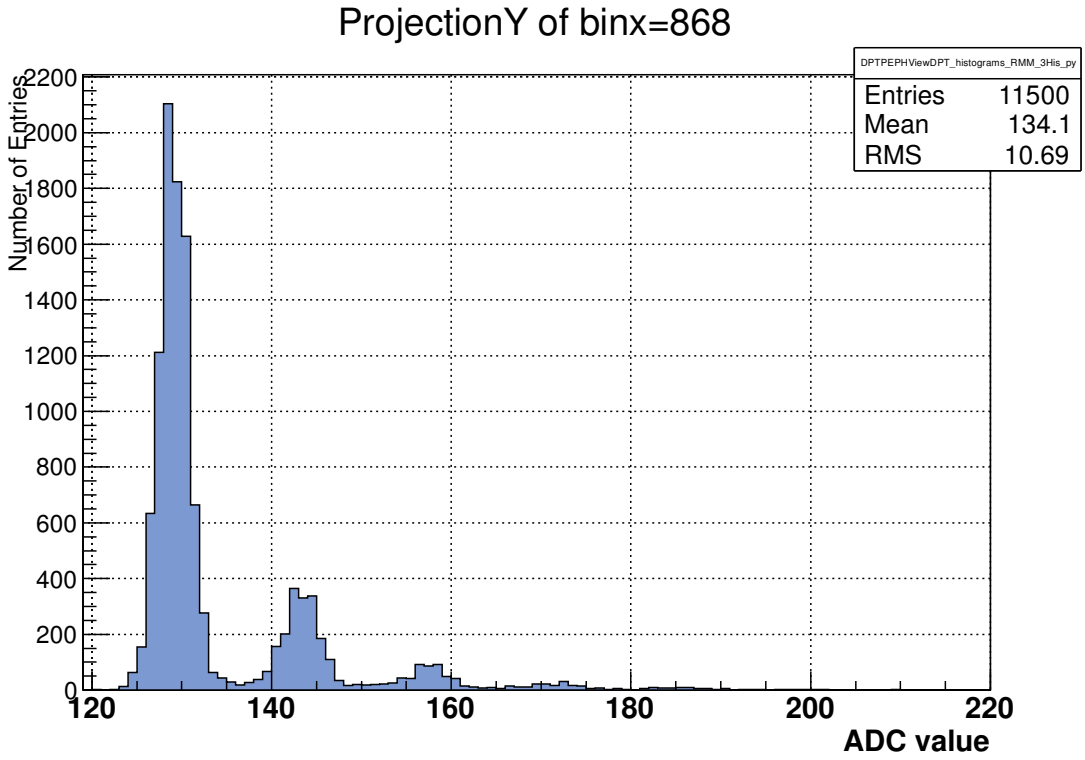

Figure 3.19: Photoelectron spectrum for a single MPPC extracted from DPT pedestal data.

TFB Charge Injection

The electronics response of each TFB in the ECAL is not perfectly linear, and moreover there is a transition in the response between the high and low gain channels of the TFB. This is accounted for by the ability of a known charge to be injected into each channel, such that the response per channel can be parametrised and stored. Dedicated charge injection runs are time-consuming, of the order of twelve hours, and therefore take place relatively infrequently. Mercifully, a single calibration run tends to remain representative for a long period of time.

Pedestal determination

The first peak in the photoelectron spectrum is commonly referred to as the "pedestal", and corresponds to the ADC value recorded from the MPPC in the absence of any signal. The spread and position of this value depends on the MPPC in question, but the distribution is Gaussian in shape. A fit is performed to every pedestal in every channel and the pedestal ADC position is recorded, a typical set of pedestal values for a subset of the ECAL's MPPCs is shown in Figure 3.20.

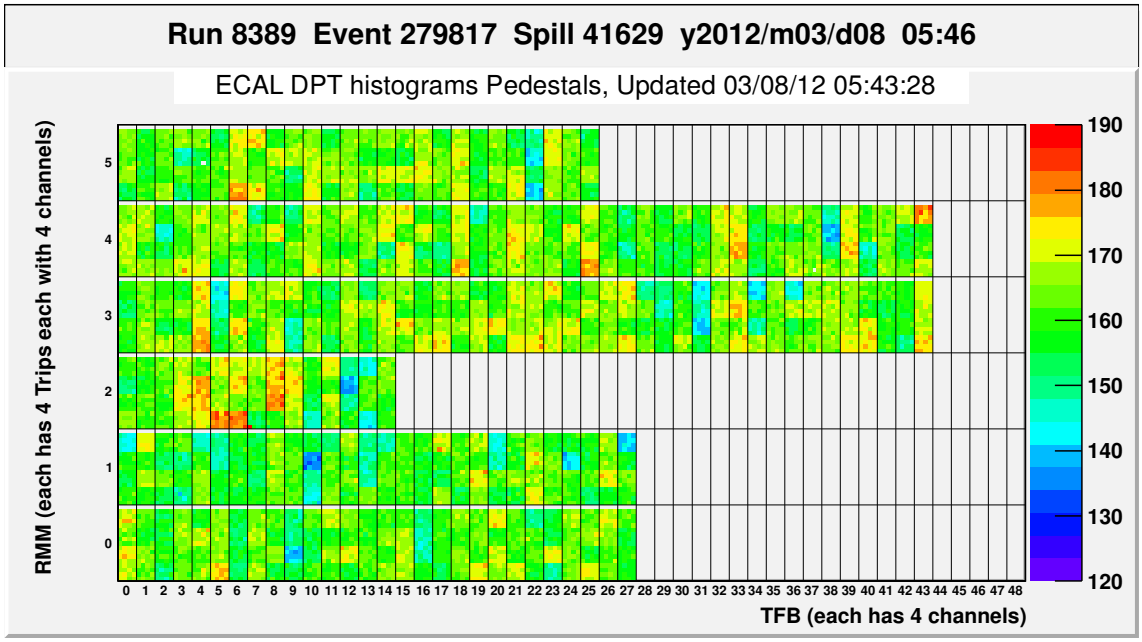

Figure 3.20: Pedestal values as recorded by the DPT.

The recorded position of the pedestal for each channel is used to offset the entire photoelectron spectrum by a simple subtraction, such that the peak of the pedestal corresponds to an ADC value of zero. A useful quantity in determining the need to perform a new pedestal run is the the difference between the "live" measured pedestal from the DPT channel histograms and the constant stored by the DAQ for all available channels, as shown in 3.21.

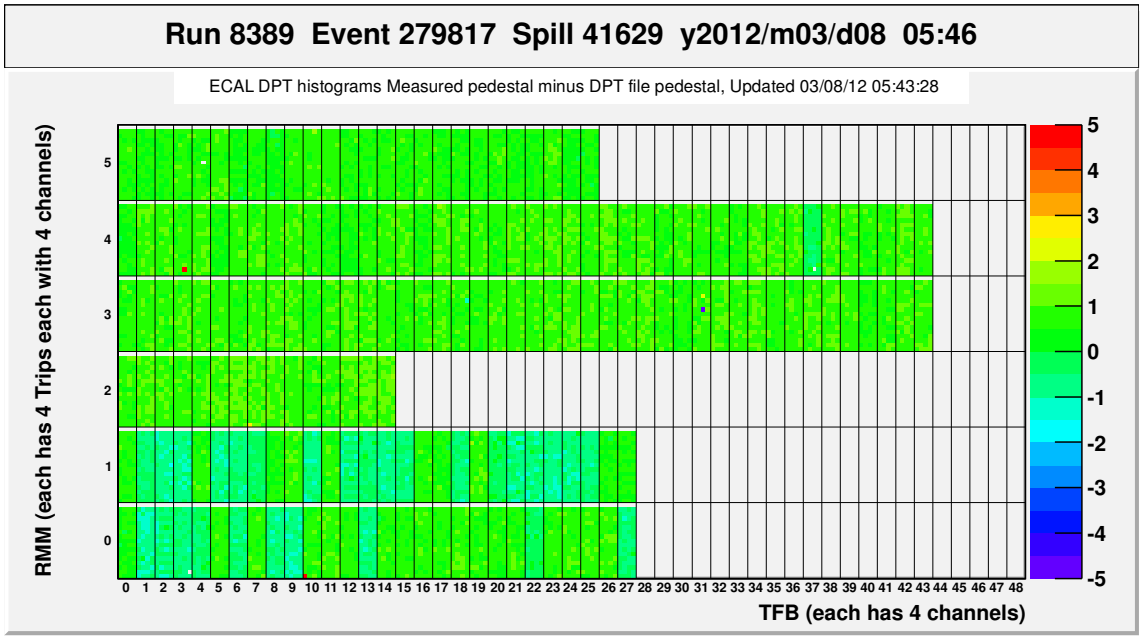

Figure 3.21: Quantification of pedestal drift from the stored pedestal value for MPPCs in 6 RMMs

Gain calculation

The gain of MPPCs is determined by taking a set of dedicated runs in the local DAQ, with the aid of a parameters file provided to a MIDAS sequencer. As the local DAQ is furnished only with a SCM, the full detector is read out at a constant rate set determined by the trigger frequency. Each run in the sequence corresponds to a specific trim voltage offset, set by the sequencer, such that the end result is photoelectron spectra for every MPPC for a range of applied voltages, projections of each of these spectra is depicted in Figure 3.24.

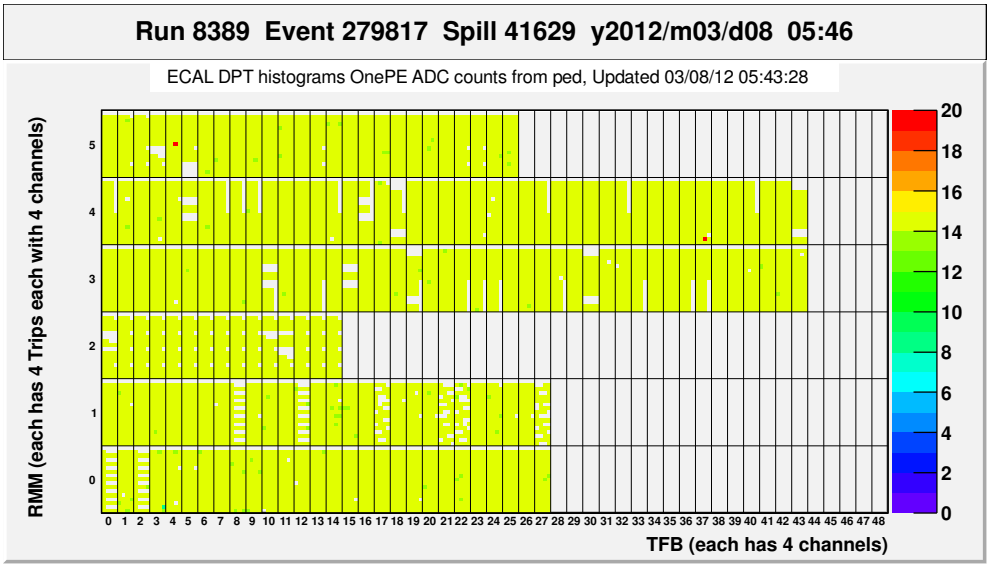

Figure 3.22: Gain in ADC counts as determined by analysing DPT photoelectron spectra.

The gain of each distribution is determined by performing a Gaussian fit to the pedestal and the first photoelectron peaks and determining the number of ADC counts between the respective means of the peak fits, the result of which is depicted in Figure 3.22. This process is repeated for all of the pedestal runs, and the change in gain as a function of applied temperature is then used to determine the breakdown voltage of the MPPC. This breakdown voltage is then used to determine the applied voltage at which the MPPC operates at the nominal over-voltage of 1.366V, which corresponds to a nominal gain of 14. An example of the result of this process is shown in Figure 3.23.

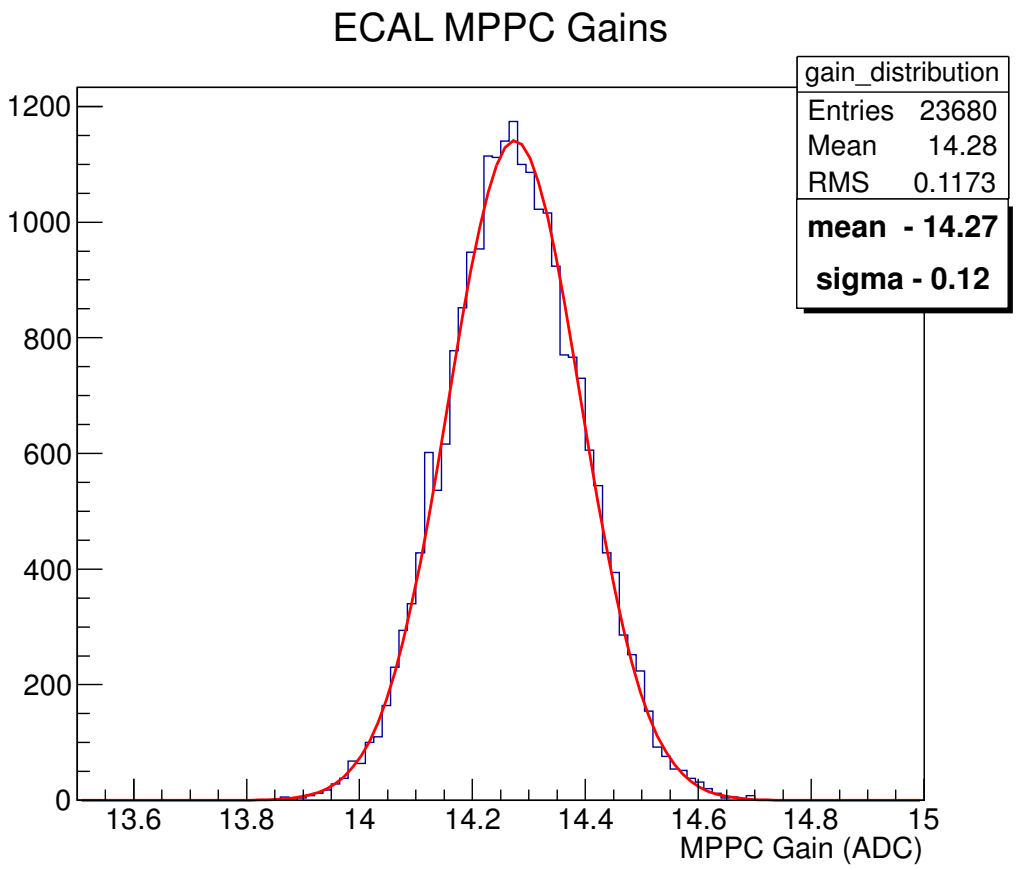

Figure 3.23: Distribution of MPPC gain values after a successful calibration run.

A number of corner cases can occur which result in the determination of the MPPC breakdown voltage to fail, such as the failure of the peak fitter to determine the location of the pedestal and first photoelectron peaks. This can occur if the applied voltage to a given MPPC is such that it is operating near or below its breakdown voltage, thus rendering the photoelectron peaks of interest irresolvable, or in the case of the MPPC operating below breakdown temperature, being absent completely. In these cases the trim voltage of problems channels must be painstakingly investigated and set by the expert. The process by which this was achieved was improved by automatically identifying channels for which the gain setting process had failed, displaying the relevant photoelectron spectra and allowing the expert to set a new trim by simply entering a new value into an interface, at which point the correct XML trim file would be automatically updated.

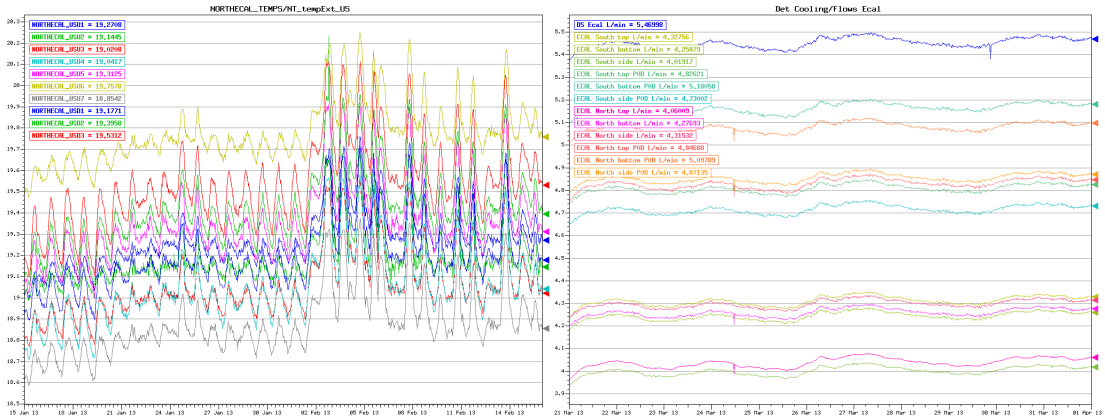

(a) ECAL external temperature variation. **(b)** ECAL cooling system flow rates.

Figure 3.25: GSC ECAL temperature and flow rate health plots

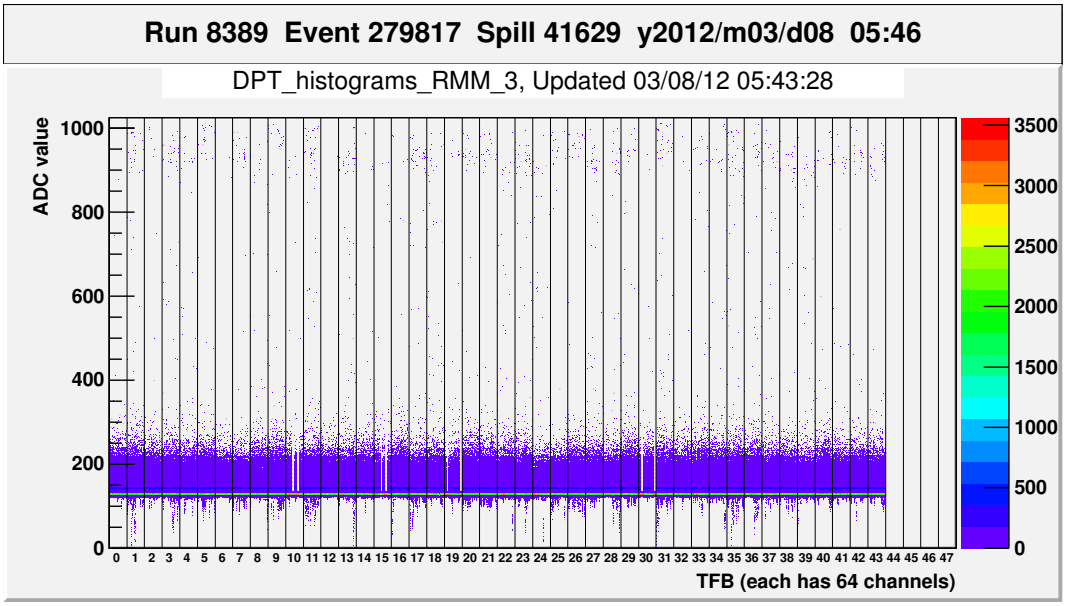

Figure 3.24: Two dimensional histogram of calibrated MPPC photoelectron spectra from pedestal data.

3.4.2 Monitoring

ECAL expert duties also include the real time monitoring of a number detector attributes, which are provided by the ND280 Global Slow Control process. Most monitored detector parameters have an associated GSC alarm process which is set to notify shifters of any unexpected behaviour.

The temperature of each ECAL is measured at a number of points around the detector via a set of thermal sensors affixed to the internal bulkheads of the detector, readings are also provided from a sensor on the TFB itself, the typical output of which is shown in Figure 3.25. Observation of the detector temperature is important as discussed previously as the response of MPPCs strongly depends on the environmental temperature.

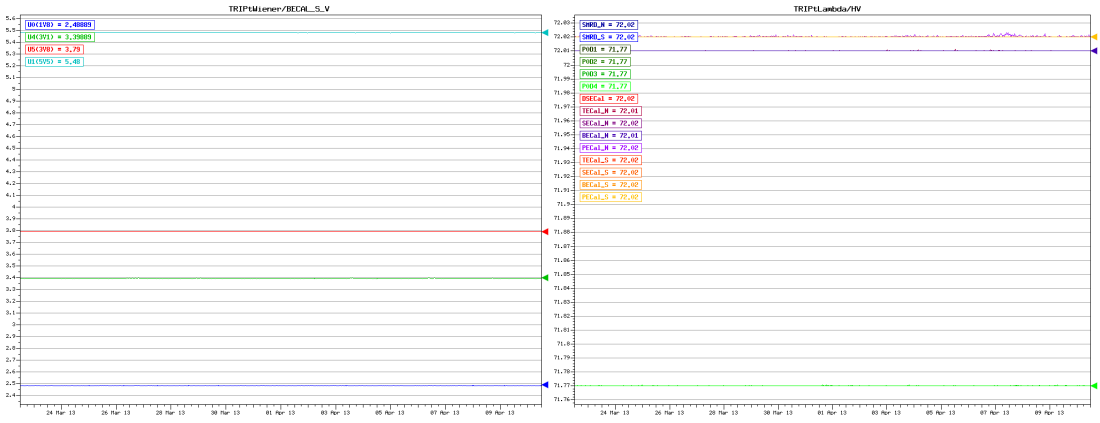

(a) ECAL Wiener supplied TFB voltages **(b)** ECAL TDK-Lambda MPPC HV

Figure 3.26: GSC ECAL voltage health plots

The TFB power lines expect voltages of 5.5V, 3.8V, 3.2V and 2.2V as input, typical GSC output demonstrating this is shown in Figure 3.26. The output voltages of the power supplies tend to be set higher than this to accommodate any voltage drops from the power supply to the detector's electronics, and higher than expected voltages at the TFB side are taken care of by voltage regulation on the board itself. The MPPC voltage, set by the TDK-Lambda power supply, is also an important requirement as to ensure the stable operation of the ECAL's photodetectors owing to the fact that each of the MPPC voltages are carefully calibrated relative to the power supply voltage.

Chapter 4

Software Reconstruction at ND280

The output of ND280's software reconstruction chain constitutes the main dataset of the analysis to follow, and consists of a handful of third-party dependencies and a mix of bespoke C++ and Python code which handles the processing and analysis of data. The main library upon which the suite is built is ROOT [62], an object oriented C++ data analysis framework used throughout high energy physics.

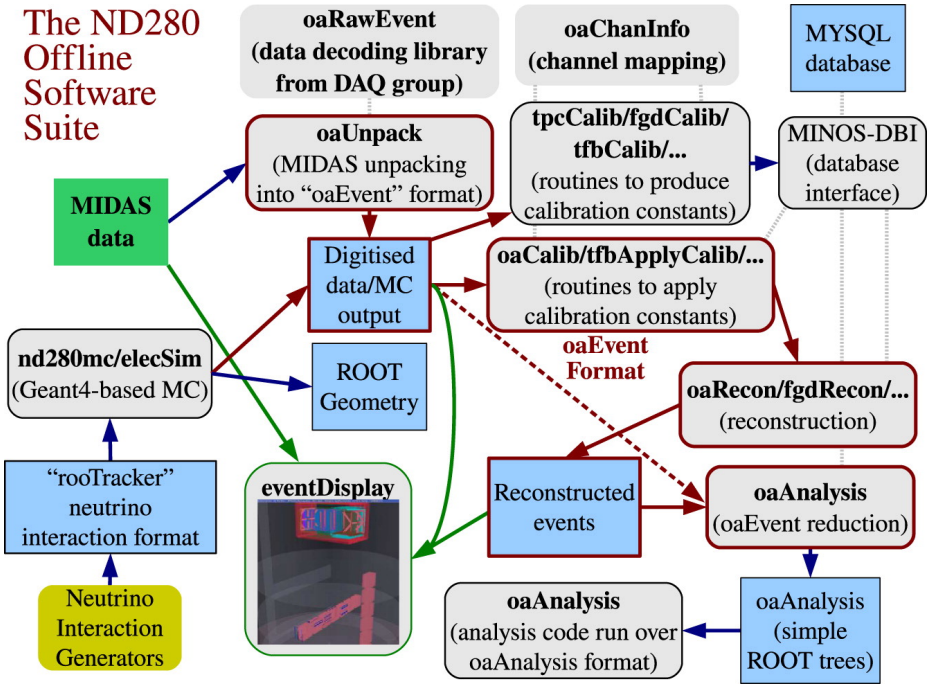

Figure 4.1: The ND280 offline sofware suite [42].

4.1 ND280 Reconstruction Chain

The ND280 off-line software suite is made up of a chain of interdependent modules, all of which have a few core dependencies in common. The relationships between these packages is depicted in Figure 4.1. The oaEvent package serves as the cornerstone of the suite, serving to specify a set of base objects upon which the bulk of ND280's I/O capability is built, and is designed with long-term stability in mind,

therefore receiving very few modifications.

Both data and simulation files employ the same oaEvent format at an early stage in the reconstruction chain, allowing for both types of data to be treated easily and with the same routines. Data collected by the DAQ system is written in the MIDAS [63] file format, and must first be converted to oaEvent format by the oaUnpack package. Simulation data is created in a number of stages, the neutrino interactions are first generated with the aid of an interaction generator (namely NEUT [64] or GENIE [65]), before being propagated through GEANT4 [66]. The detector electronics response to the generated particles is then simulated in the elecSim package, after which point the simulation data is stored in oaEvent format.

Both data types are then calibrated using parameters stored in and retrieved from MYSQL [67] databases. Calibrated hits are then processed by various subdetector reconstruction packages, the outputs of which are reconstructed globally using the RecPack [68] package. The final step involves the conversion of the often information dense oaEvent format to a relatively lighter, ROOT data format for use in physics analyses, called the "oaAnalysis" file format.

4.2 Subdetector Reconstruction Packages

Each subdetector has its own reconstruction package [69], responsible for taking simulated or calibrated, real hits as input and building reconstructed objects as prescribed by the oaEvent output specification. What follows is a brief overview of the reconstruction process of each package, focusing mainly on relevant reconstruction outputs which are employed in the analysis to come. The steps of the ECAL reconstruction are explained in relatively more detail as to highlight areas in which the author assisted in the development and maintenance of the package.

4.2.1 p0dRecon

The P0D reconstruction consists of a sequence of stages, in which hits are time separated, filtered, and subsequently reconstructed as belonging to tracks or showers. Calibrated hits are taken as input and separated into their constituent 23 integration cycles. The hits are then filtered for noise by applying cuts to combinations of charge and nearest neighbour parameters.

The hits are then passed to a track reconstruction algorithm, which identifies the seeds of tracks by applying a Hough Transform [68] to the XZ and YZ two-dimensional views of the detector, thereby identifying groups of hits which correspond to straight lines. Located track seeds must contain at least four hits, and tracks are rebuilt from the seeds layer by layer with a road following algorithm. The character of EM showers at this stage of the reconstruction is such that the reconstructed objects tend to manifest as parallel or collinear in orientation, therefore a merging algorithm is employed to consolidate these tracks.

The reconstructed two dimensional tracks from each view are then matched to create three dimen-

sional objects, those objects are then fitted with a Kalman filter (or a "Parametric" fitter in cases where the track is prohibitively high angle or short). The fitted 3D tracks are then used in the reconstruction of vertices, where each pair of tracks are considered pairwise. Constituent tracks are then analysed by a PID routine which determines the originating particle by considering the energy deposited by the track. The full results of the track reconstruction algorithm are passed to a shower reconstruction algorithm.

4.2.2 tpcRecon

The TPC reconstruction analyses data from each of its three detectors individually, breaking down tracks which span the tracker region into individual segments which are subsequently matched with corresponding reconstructed tracks from other detectors by reconstruction packages downstream in the software chain. The first stage of the analysis algorithm involves the processing of a waveform, which corresponds to the time varying ADC readout from an individual micromega pad for a specific time period. Waveforms are clustered by row, and subsequently joined into tracks based on their spatial and temporal coincidence by a pattern recognition algorithm.

Particle identification in the TPC is performed by a "truncated mean" [70] algorithm. Tracks are clustered from the readout pads and the total energy of each cluster is determined by summing the charges of its consistent hits. The truncated mean C_T, a quantity determined by calculating the mean energy deposition of clusters while omitting the largest energy depositions, and is functionally dependent on both the number of samples used in calculating the truncated mean and the track length. This is accommodated by the inclusion of calibration factors which are determined by the number of clusters and the track length, and are included in the determination of the calibrated truncated mean energy deposit $\overline{C}_T$ per segment, given by:

$$\overline{C}_T = \frac{1}{\alpha N f(N)} \sum_{i}^{\alpha N} g(d_i) C_C(i)$$

Where N is the number of energy measurements, α is the truncation function, $C_C(i)$ is the energy of the ith cluster, $f(N)$ and $g(d_i)$ are calibration factors relating to the cluster sample size and segment length respectively.

This quantity, coupled with a measurement of the particle momentum from its track curvature, is compared against a set of expected energy depositions for a range of particle types, and a "pull" σ_E in each particle hypothesis is defined as:

$$\sigma_E(i) = \frac{\overline{C}_T - C_E(i)}{\sigma_o(i)}$$

for each particle hypothesis i, with $\sigma_o(i) = \sigma_T(i) \oplus (\frac{dC_E}{dp})\sigma_P$ [70] corresponding to the uncertainty of the measured particle momentum and the variances on C_T and σ_T. Typical distributions of the pull in the electron hypothesis for electrons are shown in Figure 4.2.

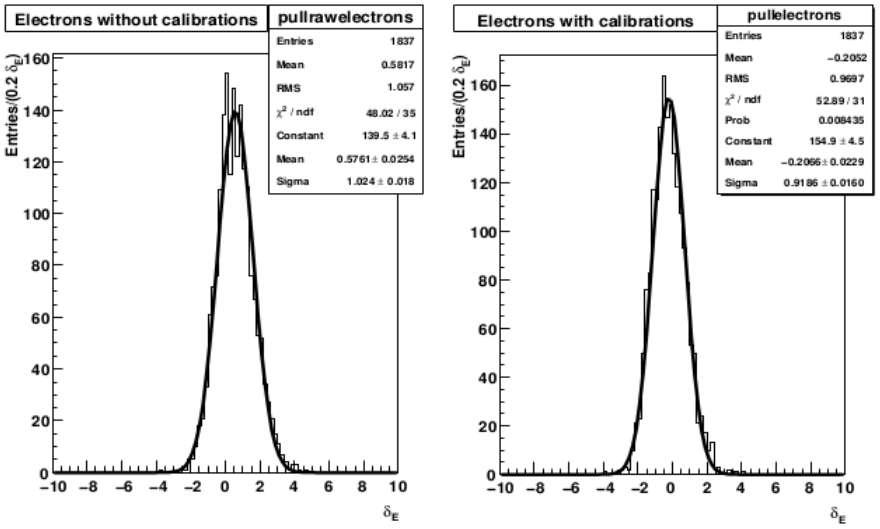

Figure 4.2: Pull in the electron hypothesis, in the respective cases of no applied calibrations and with calibrations. [70]

4.2.3 fgdRecon

The FGD reconstruction is split into three distinct algorithms, the first arranges hits into separate time bins. The spacing of the bins is determined by the temporal separation of consecutive hits, whereby a new bin is created when the time difference between a pair of hits exceeds a defined threshold.

These time bins are then analysed independently by separate algorithms depending on whether a TPC track has been reconstructed in the same time period. In the absence of a coincident TPC track, objects in the FGD are reconstructed in isolation, and employs pattern recognition schemes (namely a Radon transform and an algorithm based on SciBar's "Celluar Automation") to reconstruct tracks which do not leave the FGD.

Otherwise, tracks from the TPC are extrapolated to hits in the FGD and matched with the aid of RecPack's Kalman filter.

4.2.4 smrdRecon

The SMRD reconstruction is executed after additional calibrations relating to the double-ended nature of the detector readout are applied by a separate package, and consists of two algorithms. Like the FGD reconstruction, one algorithm deals with matching hits in the detector to reconstructed tracks in other sub-detectors using RecPack's Kalman filter, the other concerns itself with reconstruction inside the SMRD only.

4.2.5 ecalRecon

The ECAL reconstruction consists of a chain of algorithms, beginning with the preparation of calibrated hits. These hits are organised by 2D view and integration cycle and are treated separately by the reconstruction. A charge cut is applied to reduce noise hits and readout from double ended bars are combined

into single hits. The filtered hits are then passed to an algorithm that applies an attenuation correction to the hit charges, to account for the light yield drop by virtue of the signal traversing the optic fibres. The hit charges are then rescaled to MIP equivalent units, a quantity determined separately for both simulation and data which corresponds to the typical energy deposition of a through-going cosmic ray muon.

Hits are then analysed by a three stage clustering algorithm, with each view of the ECAL analysed separately. "Basic" clustering isolates the highest charge hit in the view and then adds surrounding hits on the basis of three considerations. Firstly whether any given hit is in a neighbouring or next-to-neighbouring layer, secondly whether a hit is in an adjoining bar in the same layer, and finally whether a hit's time stamp is within a defined window of that of the seed. This process is is then recursively repeated for all of the hits found by the clustering algorithm, with each new hit being considered as a seed, until no new hits are found.

The result of "Basic" clustering must contain at least three hits in order to be processed by the next stage of the chain. The "Combine" cluster seeks to merge clusters from the same particle event which have been reconstructed as spatially separated individual clusters by the basic clustering, and does so by considering the relative positions of clusters as well as individual cluster parameters calculated by a principal component analysis (PCA).

The final stage of the clustering, "Expand" clusters, considers individual unclustered hits for addition to existing clusters on the basis of relative timing information and a PCA based criterion, similar to that used by the cluster merging stage.

Complete 2D clusters are then matched together into 3D objects, with the ratio of charges between views and the difference in the end layer number of pairs of clusters being employed in the construction of a likelihood. All possible combinations of clusters between views is considered, and the pairings with the best likelihood value are combined into 3D clusters.

A rematching step follows in which unmatched individual hits in one view are matched against potential 2D clusters in the other. The hits are subject to tight time and layer cuts, and is included to accommodate for the case of low energy depositions in which the 3-hit 2D clustering threshold is satisfied in only one view.

The position of hits inside 3D clusters is then recalculated using position information of neighbouring hits in both views. Upon recalculation of individual hit positions, the attenuation correction and MEU unit scaling is performed on the original charges of the constituent hits. The clusters are then passed to an algorithm written to reconstruct electromagnetic showers, the process by which this occurs discussed in detail in Chapter 5.

A fit is then performed on each cluster, under both track and shower hypotheses. The shower fitter determines the direction and central position of the shower by way of a PCA analysis. The track fitter is a more detailed algorithm which performs a sequence of linear fits to distributions of hits, initially on

each 2D view invidiously and ultimately resulting in a 3D track. Each track object consists of a set of nodes, each node containing position and direction information results from the fit.

The final relevant step in the reconstruction is the Particle Identification (PID) algorithm [54], which employs an artificial neural network, implemented wih ROOT's TMVA [71] module, to assist in the separation of track and shower like objects in the ECAL. The network takes five input parameters of an object, and returns a single value between 0 and 1, corresponding to more shower-like and more track-like events respectively. This value is used in the final determination of the character of reconstructed objects, where values below 0.5 correspond to a shower, and values above 0.5 to a track.

4.3 Global Reconstruction

The global reconstruction takes the reconstruction outputs from each of the sub-detectors and attempts to create objects that encompass the entire detector using RecPack.

Each sub-detector package provides the same standardised reconstruction output, providing the global reconstruction with information such as the the reconstruction status of the object, whether it is more likely to be a track or a shower, and a correctly filled covariance matrix.

Copies of each sub-detector object are made and, in the cases of objects reconstructed as tracks, the RecPack Kalman filter [68] is used to refit them, and in the case of showers, no modifications are made. Tracks reconstructed within the ND280 tracker are then matched with objects from the surrounding sub-detectors.

4.4 oaAnalysis

The final step of the software reconstruction is the execution of the oaAnalysis package on oaEvent files. The purpose of this package is twofold, firstly to strip specific information out of files which are relevant to analysers, therefore reducing the data footprint of what would otherwise be a dataset of a somewhat unwieldy scale. The second benefit of oaAnalysis lies in the liberation of the analyser from using the full ND280 software suite when processing data. Files processed with oaAnalysis depend on only a handful of libraries in order to be read, which are purposefully pruned to ensure that only the bare minimum of ND280's functionality is required to convert and subsequently read data in oaAnalysis format. This format is used in all of the analyses to follow.

Chapter 5

Electromagnetic shower reconstruction

5.1 The physics of electromagnetic showers

As photons and electrons traverse matter, they lose some fraction of their energy via a number of processes [72], the cross sections of which vary by energy and material, as depicted in Figure 5.1. Above a few tens of MeV, the primary processes involved in the energy loss of these particles are bremsstrahlung and pair production. For incident particles above the critical energy E_c, the emission of a photon by an electron or the conversion of a photon to an electron-positron pair will initiate an electromagnetic shower.

The reality of electromagnetic shower development is very complicated, but there exists a simplified model of shower development which reproduces most of the parameters used in characterising a given calorimeter design. The longitudinal depth is related to the radiation length X_0, which is defined as the distance an electron must travel through a material before losing all but $\frac{1}{e}$ of its initial energy by bremsstrahlung. The lateral development of the shower is characterised by the Moilère radius, which defines a cylinder of radius $R_{\text{Moilère}}$ in which 90% of the total energy of the electromagnetic shower is contained.

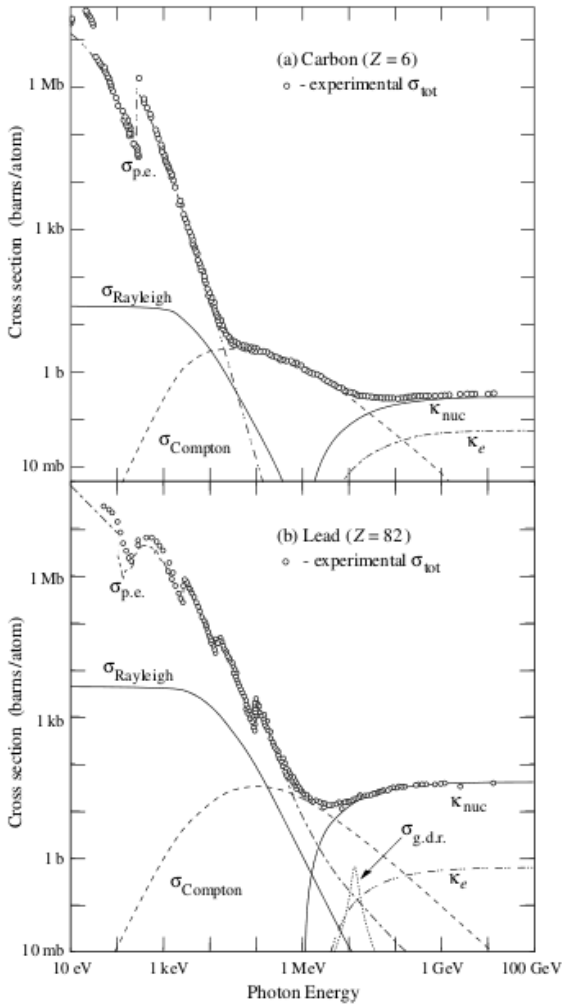

Figure 5.1: Photon cross section on carbon and lead [39]

5.2 Electromagnetic showers at ND280

5.2.1 Physics motivation

The ability to fully reconstruct particle showers at ND280 is one of the primary deliverables of the ECAL, alongside the ability to determine the type of particle associated with a reconstructed object. The ability to reconstruct a electromagnetic shower and measure its shape, direction and energy is of particular importance in the study of a number of physical processes at the near detector.

For example, any measurement of the momentum of a track in the tracking region of ND280 can be complemented (and even improved upon in some cases) with the inclusion of information from its associated ECAL energy deposit, which can serve to enhance tracker neutrino analyses. An effective ECAL electromagnetic energy and direction measurement is also important for any tracker analysis which involves the reconstruction of an interaction involving a π^0, as the dominant signature of its subsequent decay ($\pi^0 \rightarrow \gamma\gamma$) will often manifest exclusively in the ECALs, and good direction resolution

is important in order to attempt to associate two seemingly neutral clusters to one decay vertex.

5.2.2 Scintillator bar calibration

The result of any energy measurement made by the software reconstruction will depend mainly on the charges of individual hits contained in reconstructed 3D clusters, and the reliability of any measurement made is therefore contingent on the quality of any preceding calibration of scintillator hits.

The calibration process for ND280's scintillator detectors is performed in a number of steps. For the purposes of a discussion of the energy fitter, the step of greatest interest is that which normalises the charge response of each scintillator bar in the detector. Before calibration, charges from MPPCs are read out in 'pixel energy units' (PEU). This quantity corresponds to the total sum of pixels fired in the MPPC, expressed as a multiple of the charge seen when an individual pixel fires. In ecalRecon the unit of charge in hits is in "MIP equivalent units" or MEU, which is expected to be converted from PEU and equalised for every bar in every ECAL.

The normalisation of the response of each bar is carried out with the aid of cosmic ray data, collected in-situ between beam spills during data taking periods, and from dedicated cosmic runs during beam downtime as shown in Figure 5.2. Cosmic rays are minimum ionising particles (MIPs) in their typical energy ranges and therefore the energy they deposit per unit length when transiting the detector is independent of their incoming momenta. This fact is the crux of the ECAL calibration and enables the response of each bar to be understood and normalised.

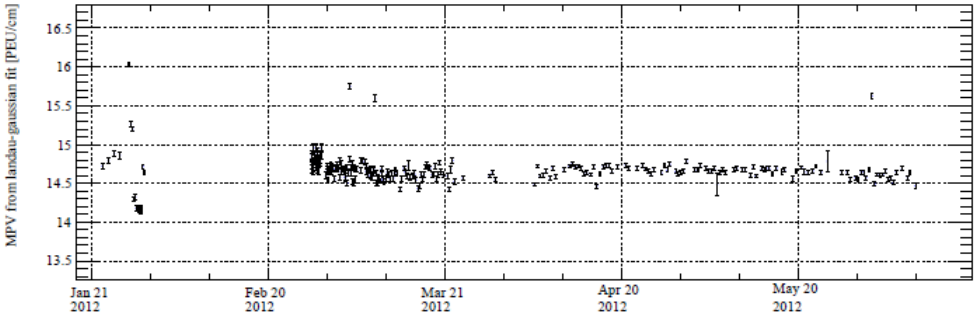

Figure 5.2: MPV from Landau-Gaussian fit of cosmic ray muons during beam data-taking, from [54]

Currently, the calibration "signal" at ND280 is that of a through-going cosmic ray muon traversing the scintillator at a distance of 1 metre from the photodetector. As cosmic rays enter the scintillator at a variety of angles, a path length correction is applied to reconstructed tracks in order to account for the additional energy deposited in the scintillator relative to a through-going track. In addition to this, an attenuation calibration is applied to account for the attenuation of signal photons as they traverse the wavelength shifting fibre before reaching the photodetector surface.

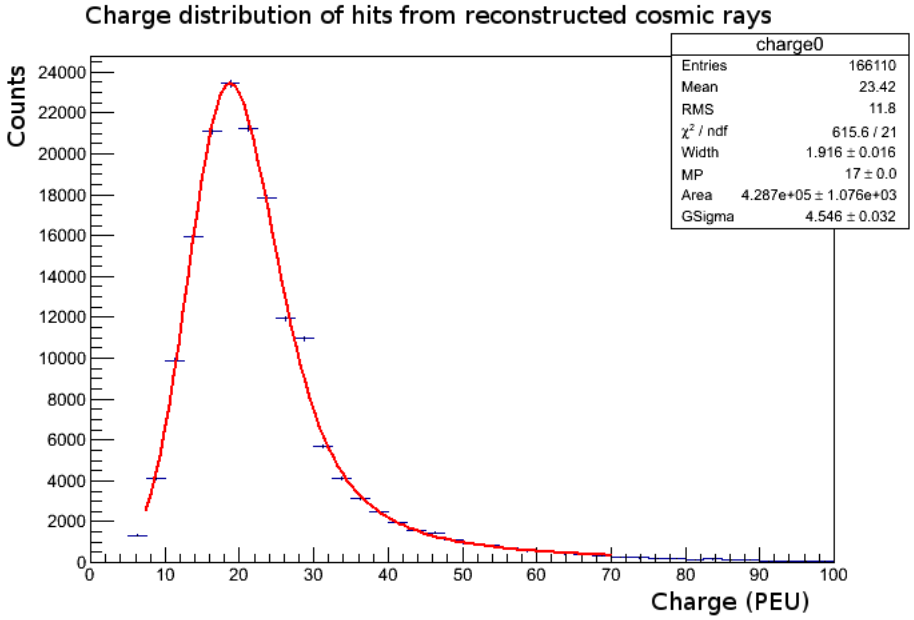

Figure 5.3: Landau-Gaussian fit to hit charge distribution of reconstructed cosmic ray data in the Downstream ECALs

Once these calibrations have been applied, the charges of reconstructed hits from cosmic data is histogrammed and a Landau-Gaussian function is fitted to the distribution, as shown in Figure 5.3. The Landau-Gaussian distribution arises from the convolution of the individual Landau and Gaussian distributions.

The most probable value (MPV) from the fit is then extracted and subsequently used in ecalRecon to convert charges from PEU to MEU. This is achieved by knowing that the energy deposited by MIPs in the detector is known, and follows a fixed distribution. By determining the MPV of the MIP's charge distribution in terms of the PEU charge, the response of the channel can be scaled to ensure the energy response across the detector is uniform.

The fitter is therefore extremely sensitive to the value of the constant used to normalise the charge distribution to MEU units, and variations in its value between modules, and even between bar types (Figure 5.4) can have a dramatic effect on the output of the fitter.

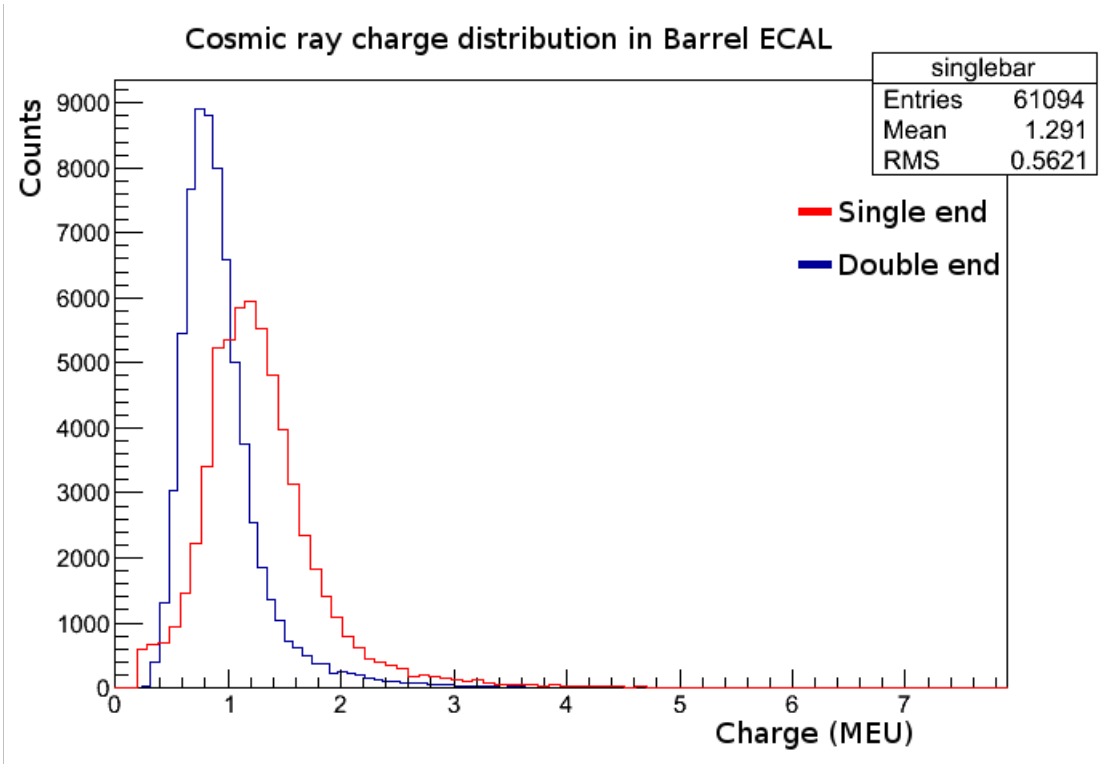

Figure 5.4: Differences in charge distributions for different bar types in the Barrel ECAL (cosmic data)

5.3 Electromagnetic energy fit

The measurement of the of the energy of a reconstructed ECAL cluster under an electromagnetic shower hypothesis is performed by the ecalRecon's EM energy fitter. This is a set of classes which employ ROOT's MINUIT minimisation package to determine the most probable energy of a cluster given a set of calculated parameters. The output of the fitter depends almost exclusively on variables which depend on the charge distribution of the reconstructed cluster.

The operation of the fitter depends upon the provision of a likelihood function L, which is a standard multivariate Gaussian distribution of dimension N, n where N corresponds to the number of cluster parameters used by the fitter. Each dimension of the likelihood corresponds to an individual cluster parametrisation, and the variation of each of these cluster parameters is quantified as a function of energy with the aid of a simulation of incident particles entering the ECAL and undergoing an electromagnetic shower within the detector.

5.3.1 Cluster parameters

The training of the fitter is performed by analysing the output of reconstructed clusters from ecalRecon associated with incoming simulated γs. γs of a fixed energy are generated at the front face of an ECAL. The simulation then propagates these photons into detector where they begin to undergo an

electromagnetic shower. The electronics response to these particles is then simulated, calibrated and the resulting detector hits are reconstructed as a three dimensional object in the detector by ecalRecon.

As the properties of these reconstructed clusters are a function of energy, simulations are generated over a range of energies, currently from 25MeV up to 20GeV. The large range of simulation is to ensure that the likelihood is well described over the entire potential range of inputs to the fitter, and the bulk of the energy points are located at the low end of the spectrum, which is the area in which most of the fitting is expected to take place.

Currently, three cluster parameters are calculated for the construction of the likelihood, with the potential to add additional parameters as time progresses. Their distributions and the variation of their fit parameters with energy are listed hence.

5.3.2 Parameter distributions

QSum

This parameter corresponds to the sum of the charges of the constituent hits in a reconstructed cluster (Figure 5.5). This parameter is particularly useful as, in the low energy region, the mean of the Gaussian fit of this parameter increases linearly with energy. This information allows the fitter to make a preliminary estimate of the most likely energy for use as an initial value for the fitter, and is given by:

$$Q_{\text{SUM}} = \sum_{i=1}^{n} Q_i$$

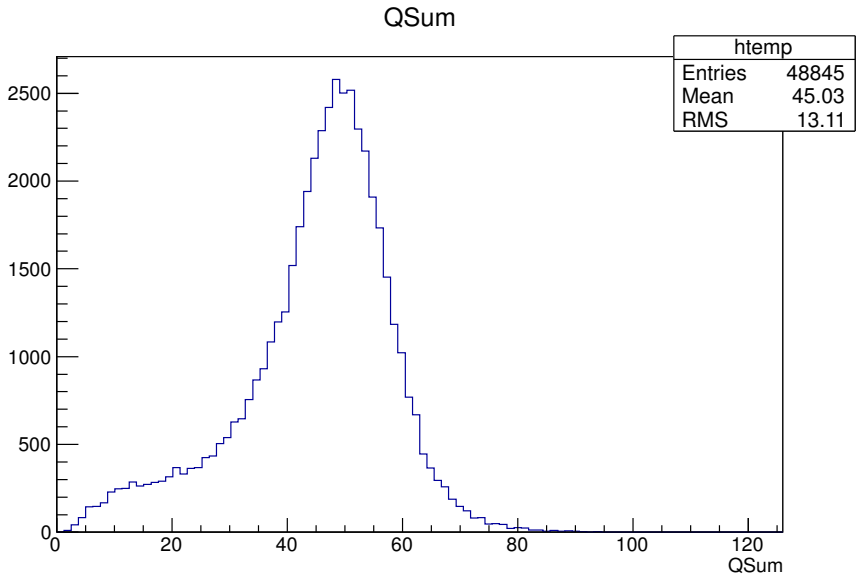

Figure 5.5: Distribution of the sum of hit charges for 50000 reconstructed events at 200MeV

QRMS

This parameter corresponds to the RMS deviation of the cluster's charges relative to the calculated mean charge of the reconstructed cluster (Figure 5.6), and is given by:

$$Q_{\text{RMS}} = \sqrt{\frac{\sum_{i=1}^{n} (Q_i - Q_{\text{mean}})^2}{n}}$$

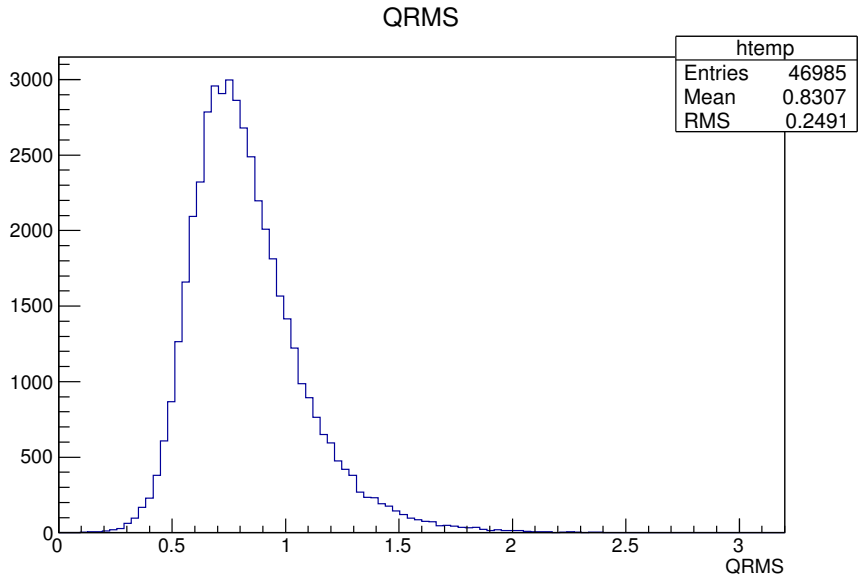

Figure 5.6: Distribution of the RMS of hit charges for 50000 reconstructed events at 200MeV

QSkew

This parameter corresponds to the "skew" deviation of the values of the cluster's charges relative to the calculated mean of the reconstructed cluster (Figure 5.7), and is given by:

$$Q_{\text{SKEW}} = \frac{\sum_{i=1}^{n} (Q_i - Q_{\text{mean}})^3}{n}$$

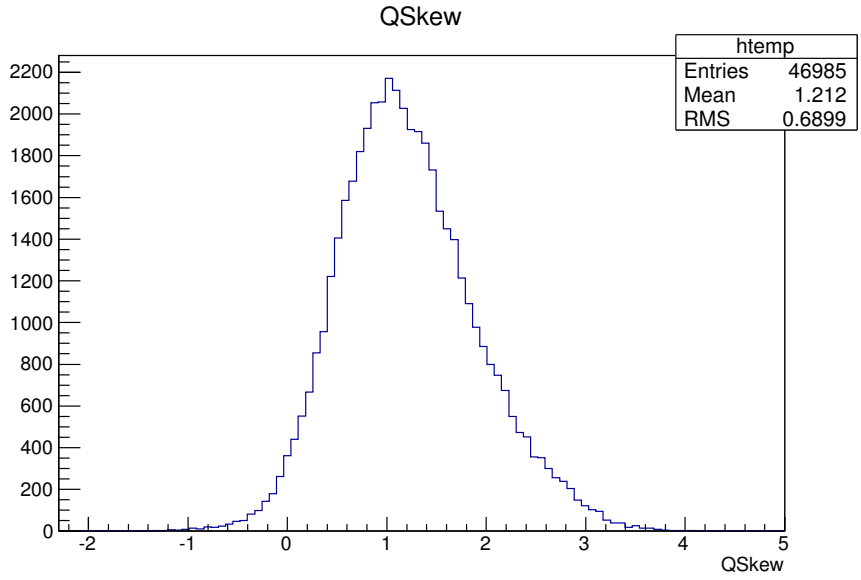

Figure 5.7: Distribution of the skew of hit charges for 50000 reconstructed events at 200MeV

5.3.3 Fit parameter variations as a function of energy

The fit results from each of these variables are stored as a function of energy. The behaviour of these variables need to be understood and parametrised across the entire working range of the energy fitter, which extends from the estimated threshold of shower reconstruction of 25MeV up to 20GeV (Figure 5.8).

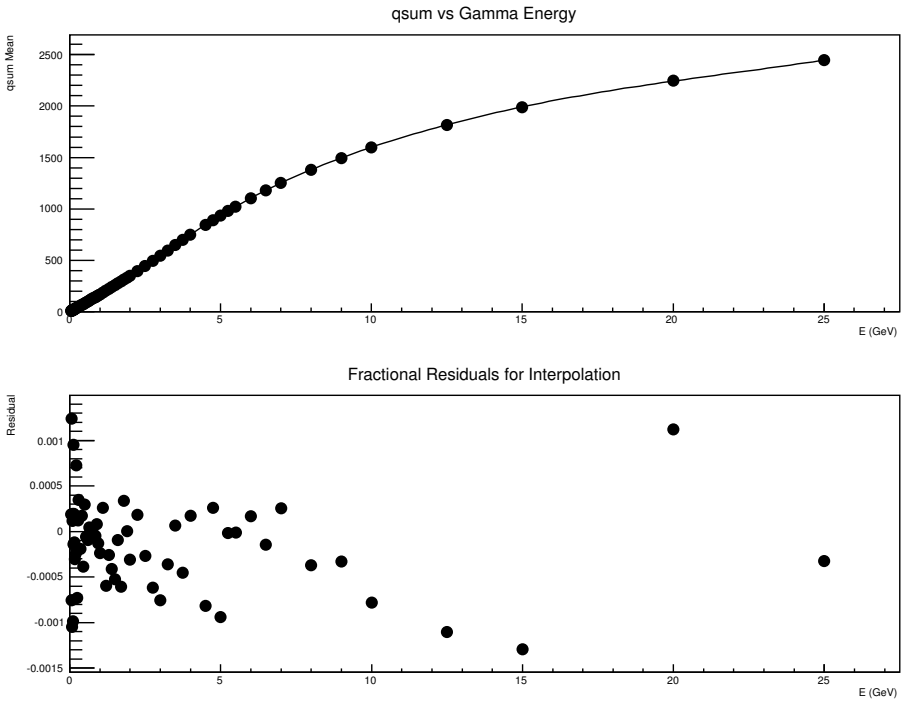

Figure 5.8: Mean value of QSum distribution as a function of energy

The complete set of input parameter variations and their associated correlations can be found in the appendix.

5.4 Verification

5.4.1 Simulation

Verification of the energy fitter's performance takes place by once again simulating showering objects entering the detector at specific energies. A large number of particles are simulated to ensure that the distribution is representative of the fitter's performance, and the standard reconstruction chain is applied to the simulated data, with an additional cut applied to clean up the dataset. Namely, no unmatched clusters should exist in either view (which could be the result of a single energy deposition being broken, which constitutes a reconstruction failure rather than a failure of the fitter). A Gaussian distribution is then fitted to the distribution of energies (Figure 5.9), and the mean value is determined to be the reconstructed energy for that verification step.

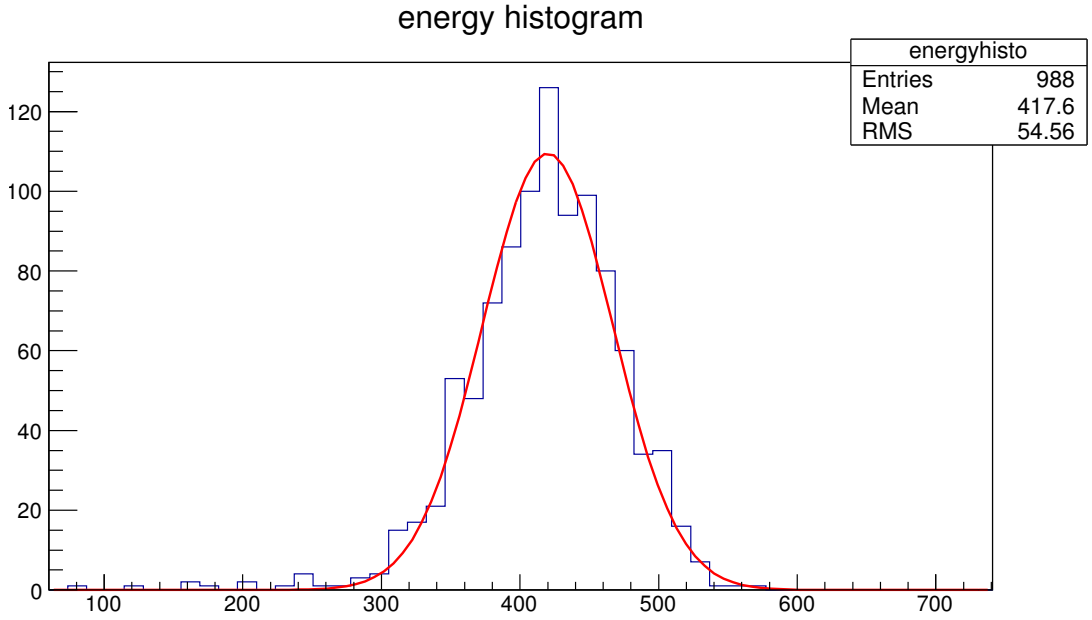

Figure 5.9: Reconstructed energies of 5000 electrons at 400MeV

This process is repeated for a range of energies in the operating range of the fitter, and the fit parameters at each energy are plotted as a function of energy (Figure 5.10). The expectation is that the mean of the fitted Gaussian distribution of reconstructed energies should be consistent with the energies of the simulated incoming particles, and the width of the distribution represents the expected energy resolution of the detector at that energy

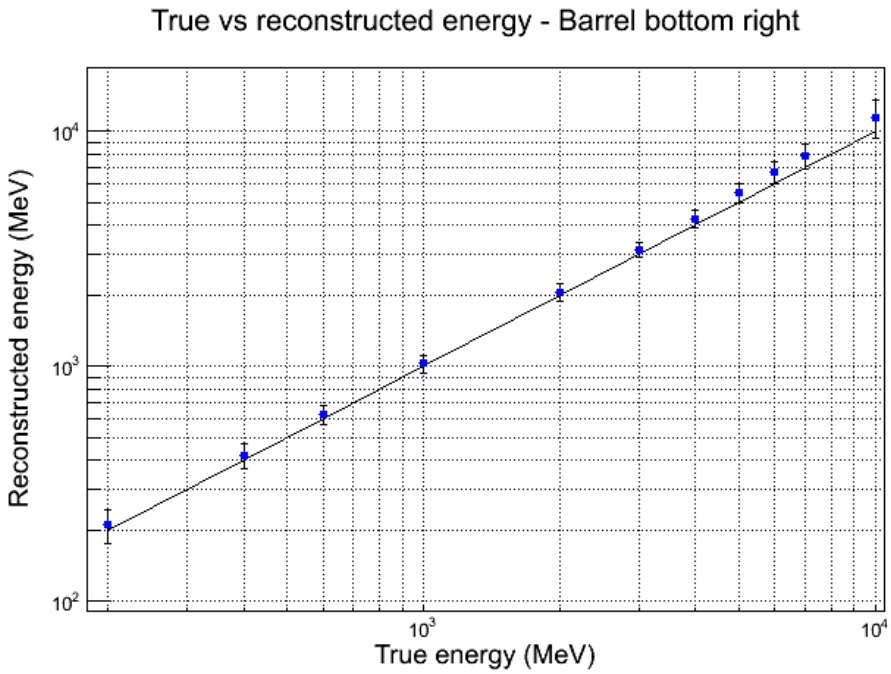

Figure 5.10: True vs reconstructed energy for 5000 reconstructed electrons.

5.4.2 Testbeam analysis

After construction of the downstream ECAL was complete, the module underwent testing at CERN with a beam of known composition. The beam was capable of producing particles of energies starting at 300MeV and up to several GeV, and consisted of a mixture of electrons, pions and protons. The detector was oriented at an angle with respect to the beam of 0, 30 and 60 degrees respectively, which allowed the response of the detector to be understood as a function of particle type, energy and incoming angle. With the aid of a time of flight detector and Čerenkov counters, it was possible to perform basic PID on the beam. This allowed the selection of electrons which can be used to evaluate the performance of the EM energy fitter in data, and assist with the evaluation of the associated systematic error, which is useful for physics analyses in determining the impact of the uncertainty of the ECAL.

Firstly, electrons are selected and their incoming momentum into the downstream is assumed to be close to the beam momentum. The reconstructed energies of electrons associated with a particular beam momentum are then histogrammed and fitted with a Gaussian, an example of this process is shown in (Figure 5.11). In this particular example a low energy tail can be seen in the distribution, which can be accounted for by the incursion of misreconstructed objects in the final dataset (for example, three dimensional objects constructed by the mismatching of two dimensional clusters).

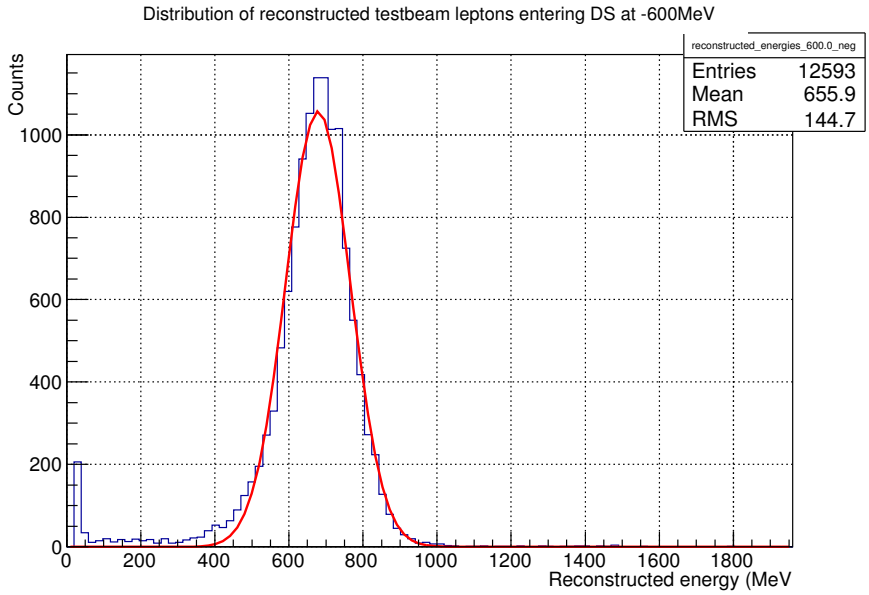

Figure 5.11: Distribution of reconstructed energies of testbeam electrons from a beam momentum of 600MeV

This process is repeated for the full range of available testbeam momenta, and then the mean of the fit is plotted against the beam momentum (Figure 5.12).

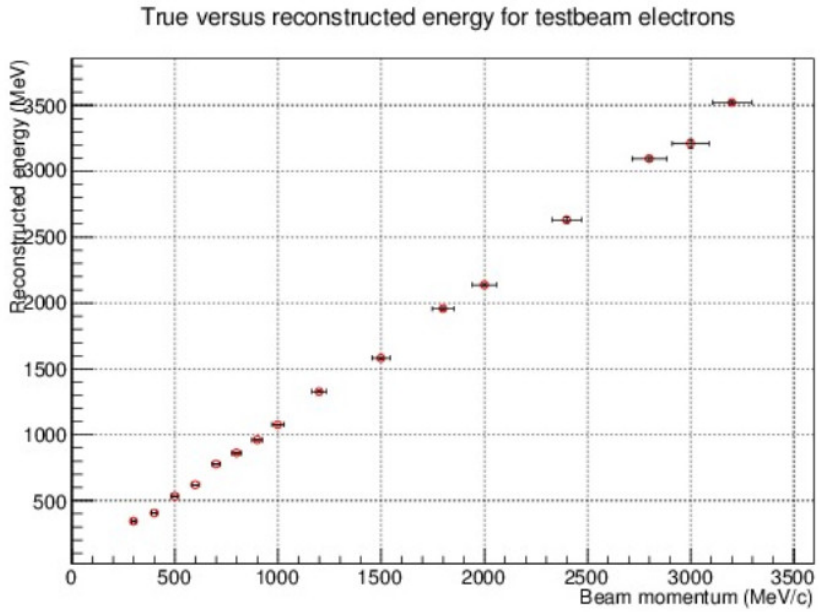

Figure 5.12: Reconstructed energy vs beam momentum of testbeam electrons

This is also performed for simulation data, and the widths of the Gaussian fits for both testbeam and simulated data are plotted in a bid to determine the resolution systematic ($\frac{\sigma}{E}$) (Figure 5.13).

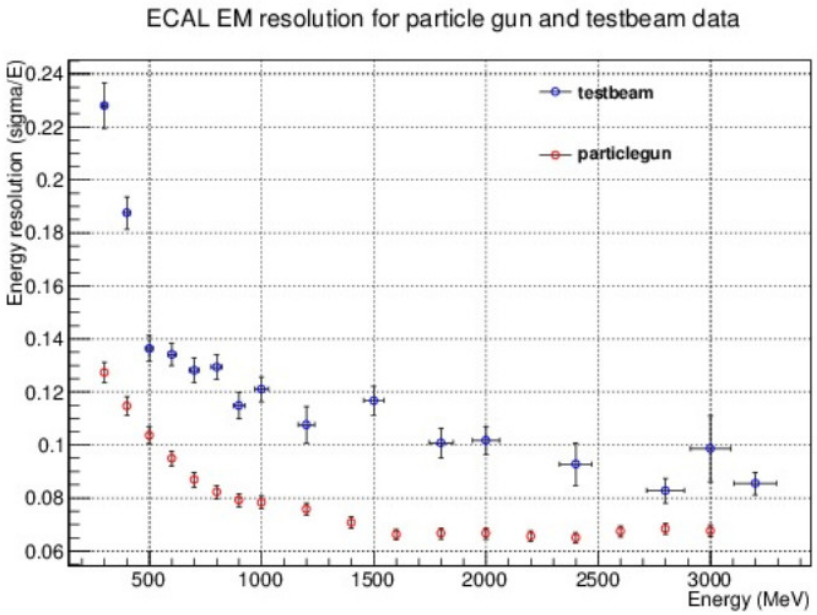

Figure 5.13: Fit results of energy distributions as a function of beam momentum (true energy) for testbeam electrons (MC electrons)

The comparison of testbeam data with simulation allows for a preliminary idea of the systematic error that can be expected when using the energy fitter in subsequent analyses. It can be seen from Figure 5.13 that the shapes of the respective distributions are in reasonable agreement, but a considerable systematic shift is present, both in the scale and the resolution of measurements. This can be accounted for by limitations in the simulation of testbeam data, which was generated using an oversimplified set of assumptions. For example, when generating simulation data the ambient temperature in the vicinity of the MPPCs is assumed to be constant. In reality the sensors would have been subject to varied temperatures across the detector during data-taking periods. As the response of the MPPC is heavily dependent on temperature this would have had an effect on data which was not corrected.

5.4.3 TPC electrons

The Barrel ECAL modules were installed in ND280 directly following their construction. In the absence of testbeam data, verification of the energy fitter's performance in ND280 is possible by examining PID/energy information associated with ECAL clusters which have an associated TPC track.

A selection of showering particles can be made with the following steps:

- Select events which contain a TPC track. Propagate this track until it reaches an ECAL surface. Search the ECAL in the vicinity of the entry point of the track for an ECAL object.
- If associated ECAL object is found, store the information relating to the TPC track and ECAL object (e.g. track momentum at front face, TPC PID, ECAL PID, EM energy)
- Apply cuts on PID information from both subdetectors

This process was applied to production 5 processed Run1 and Run2 beam data along with 10% of cosmic triggers, with the following cuts:

- ECAL TrShVal < 0.3
- ECAL cluster containment $= 1$
- TPC electron weight > 0.8

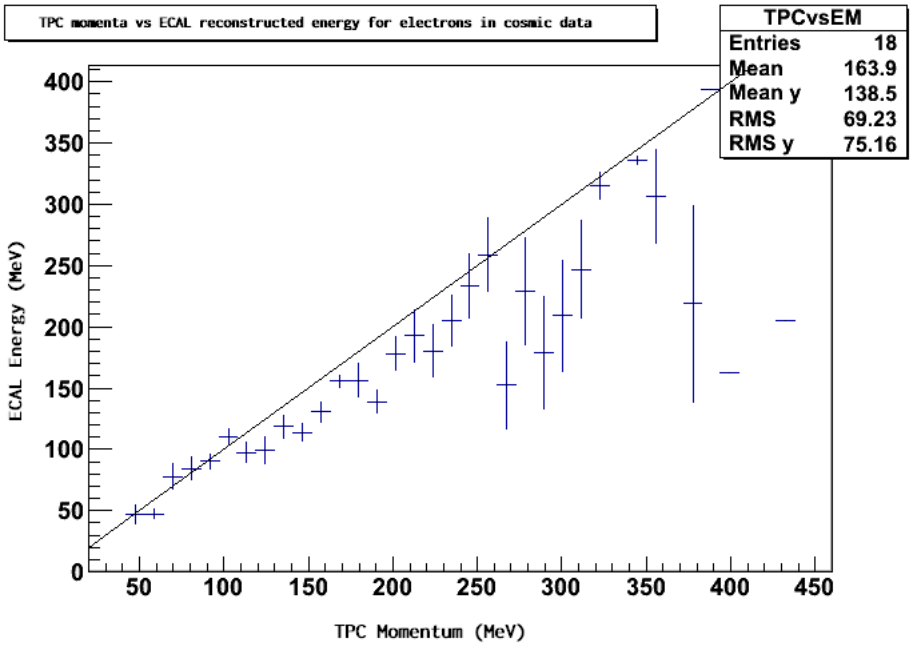

Figure 5.14: Measured momenta of TPC electrons vs reconstructed energy of associated ECAL cluster

The operating range highlighted (Figure 5.14) serves as an extension of the verification range to the testbeam data, for which there is no verifiable dataset below 4-500MeV

5.5 MC correction

The fact that a Gaussian function is used to characterise the distributions of the input variables to the fitter introduces a slight bias into the resulting output of the fitter, this is due to the underlying hit distributions having a more complicated functional form than a Gaussian. This bias is currently quantified and accounted for by the use of a post-reconstruction correction, determined from the difference between the "true" simulated energy of showering objects and the mean of the Gaussian fit described earlier in the verification section. Corrections are currently available for production 5 (Figure 5.15) and production 6 (Figure 5.16) processing, and are accessible for application on oaAnalysis output as a class in nd280AnalysisTools.

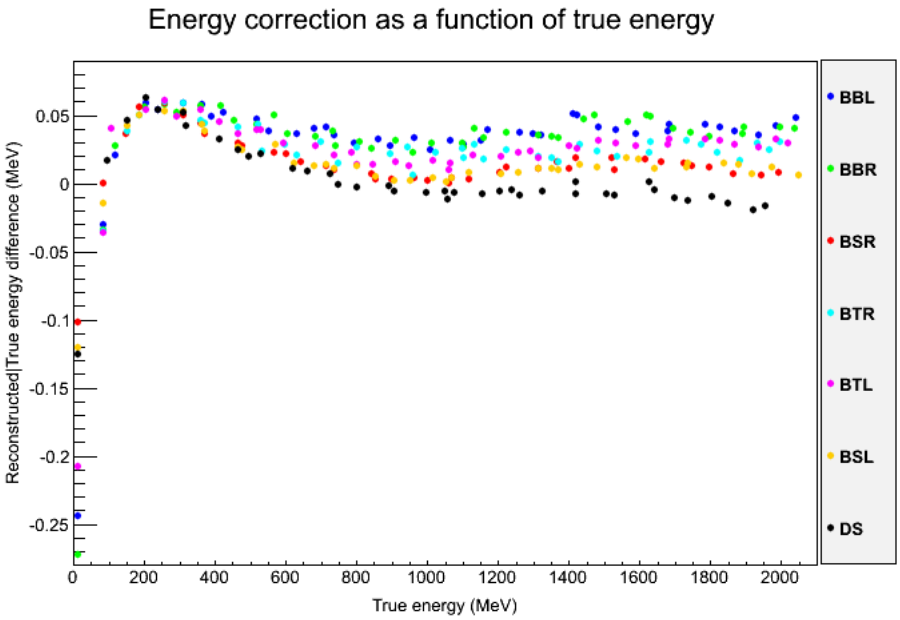

Figure 5.15: MC derived EM energy correction for production 5 processing as a function of energy

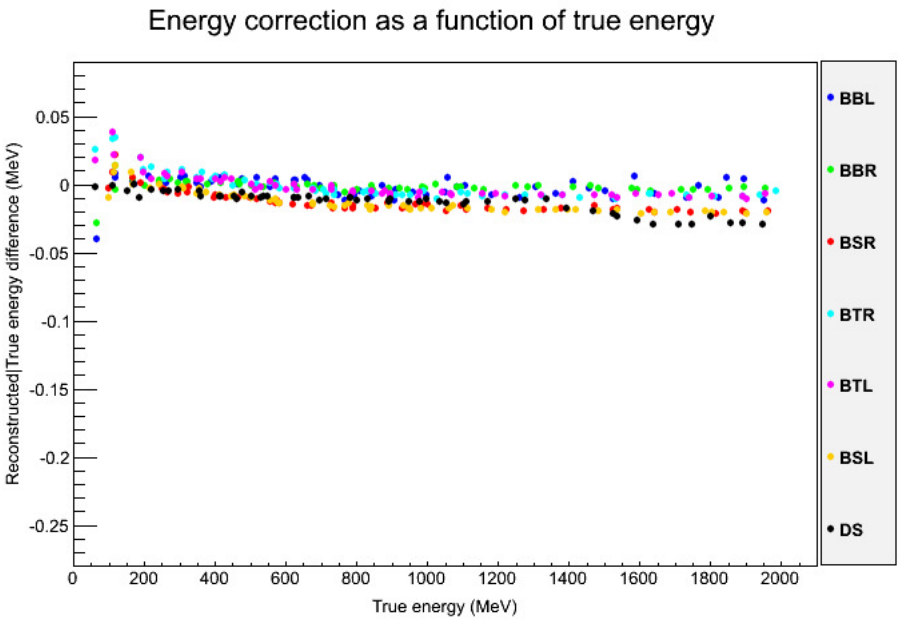

Figure 5.16: MC derived EM energy correction for production 6 processing as a function of energy

Chapter 6

Conclusion

The T2K experiment and its motivations have been introduced and discussed in the wider context of the pursuit of the empirical determination of parameters of a model which describes flavour mixing in the lepton sector. The assembly, testing and in-situ operation of the ND280 ECALs has been discussed in some detail, culminating in the continuation of development of software which assists in the estimation of energy deposited by particles incident on the detectors assuming the particles initiate an electromagnetic shower. The estimation of energy deposition of particles incident on ND280's ECALs is an important contribution to the experiment's ability to measure and constrain the intrinsic electron neutrino contamination of the T2K beam, which has been an important step in measuring the θ_{13} neutrino mixing angle. Accurate contributions from the calorimeter will allow experimenters to better identify neutrino interactions in the near detector's fiducial volume. The performance of this software is demonstrably fit for purpose in the energy ranges of relevance to the main T2K physics analyses, but is heavily contingent on the quality of calibration steps which occur upstream of the ECAL's reconstruction routines. Features of ND280's software reconstruction routines also require corrections to be made to the results of the energy fitter.

Appendices

Appendix A

EM Energy Fitter Distributions

A.0.1 Fit parameter variations as a function of energy

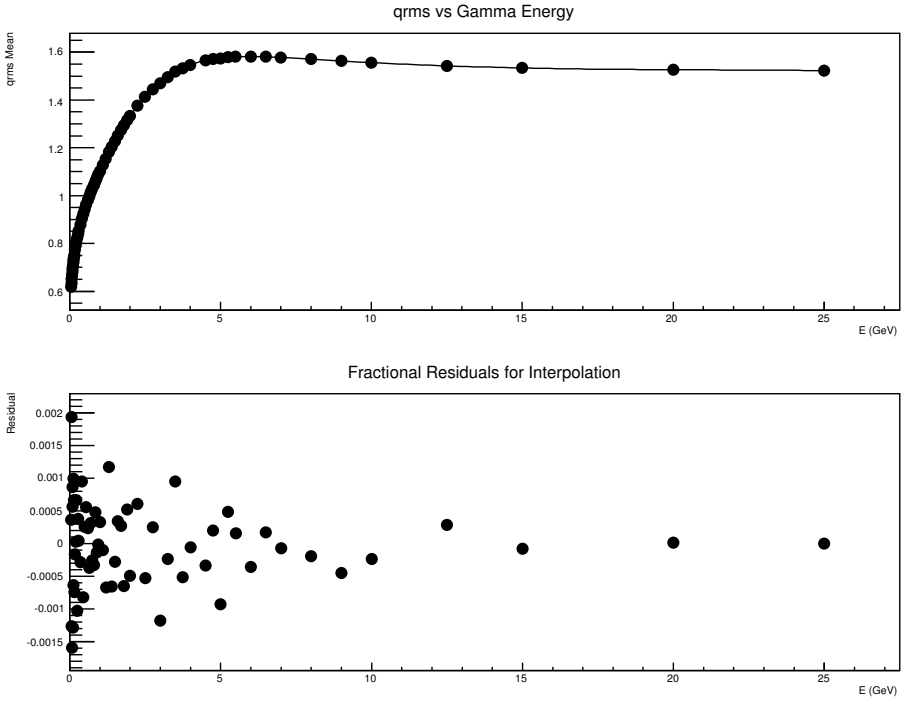

Figure A.1: Mean value of QRMS distribution as a function of energy

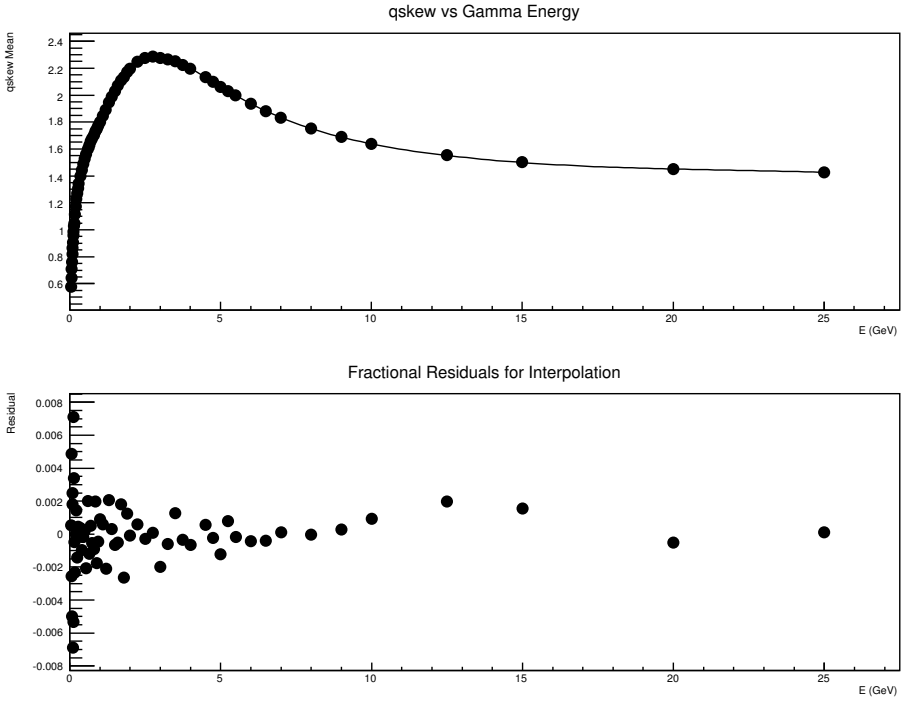

Figure A.2: Mean value of QSkew distribution as a function of energy

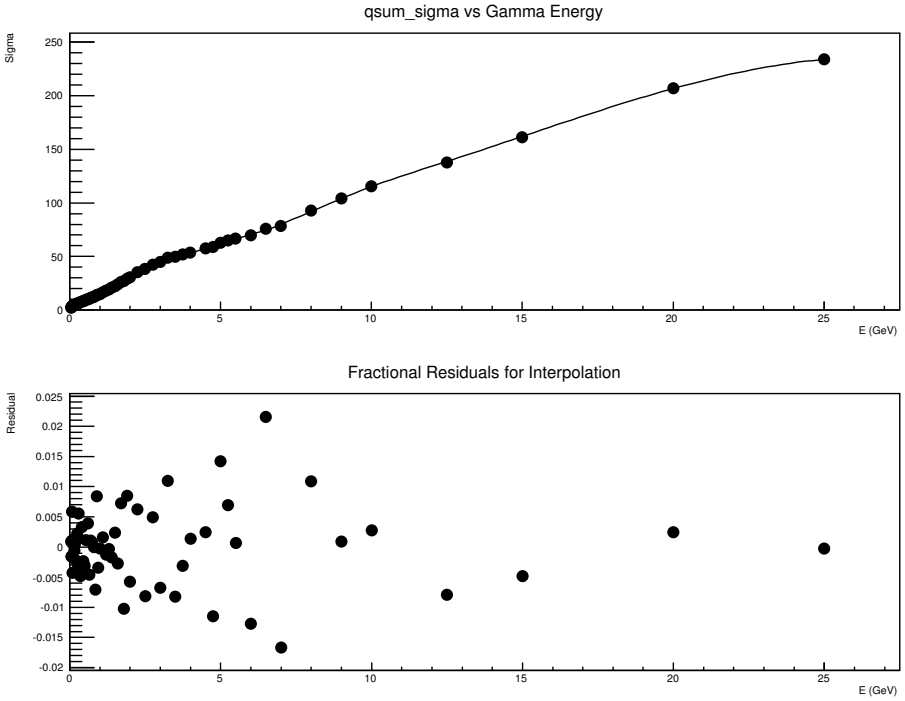

Figure A.3: Sigma value of QSum distribution as a function of energy

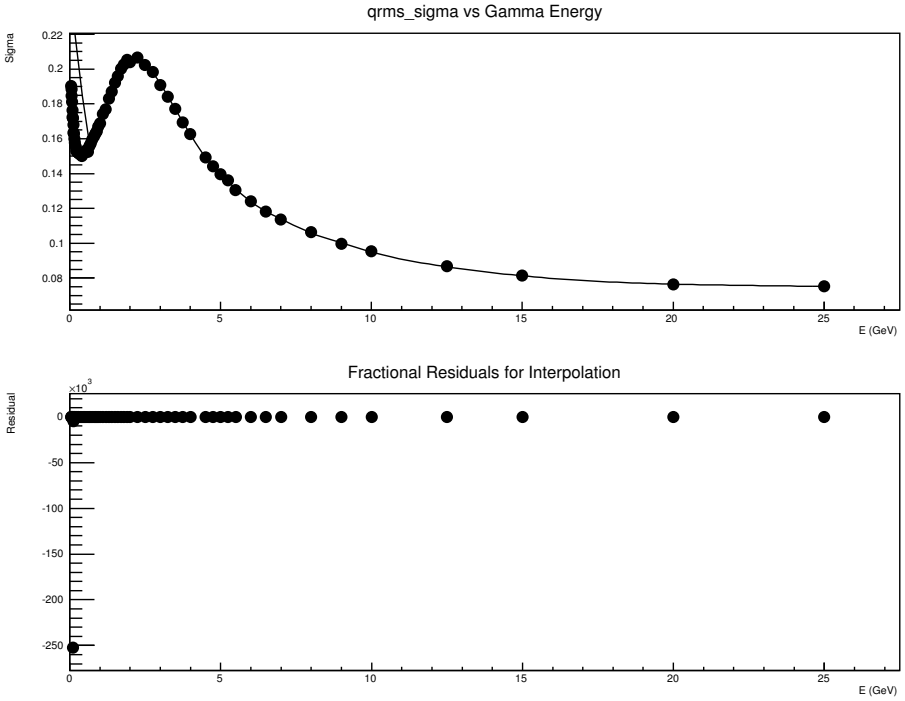

Figure A.4: Sigma value of QRMS distribution as a function of energy

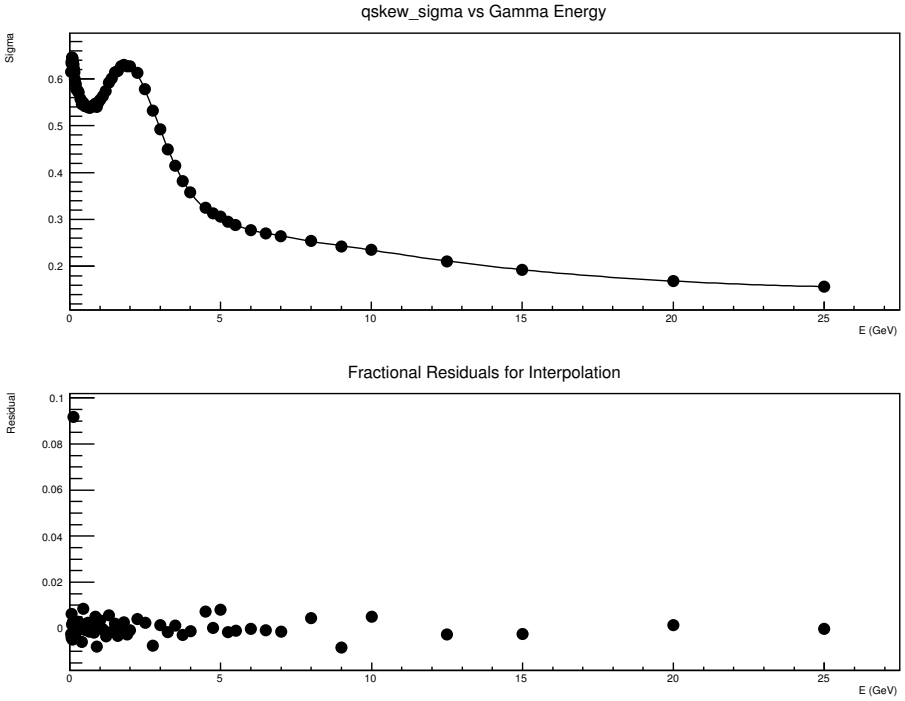

Figure A.5: Sigma value of QSkew distribution as a function of energy

A.0.2 Variable correlations

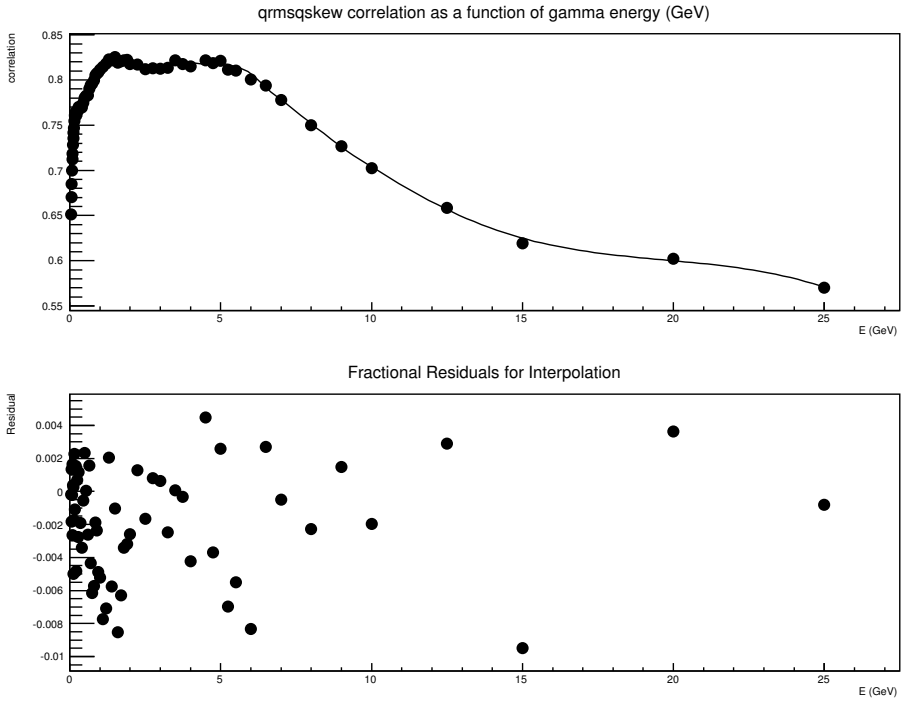

Figure A.6: QRMSQSkew correlation as a function of energy

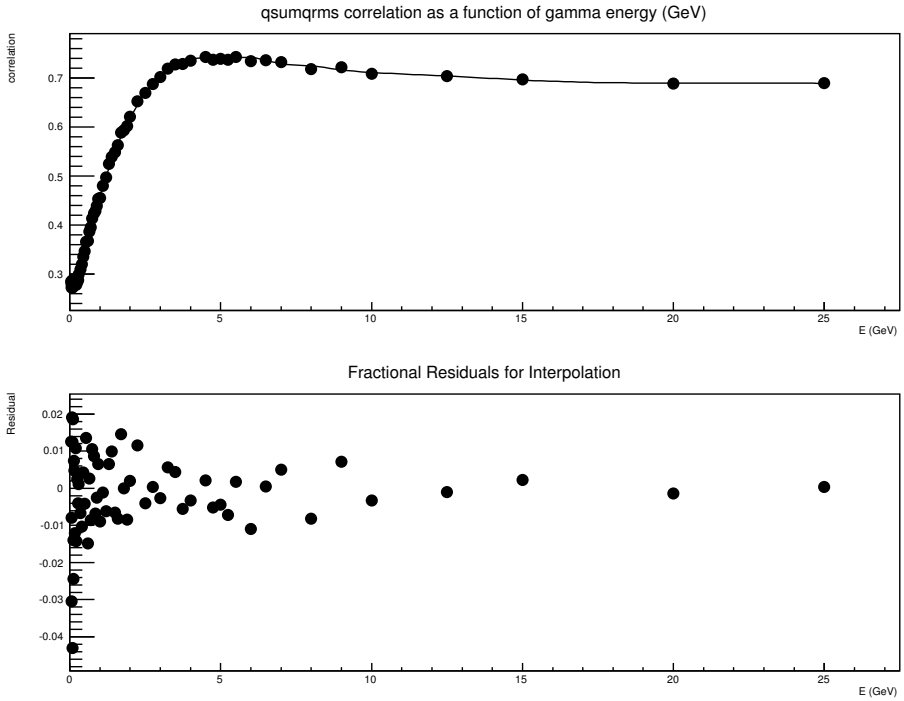

Figure A.7: QSumQRMS correlation as a function of energy

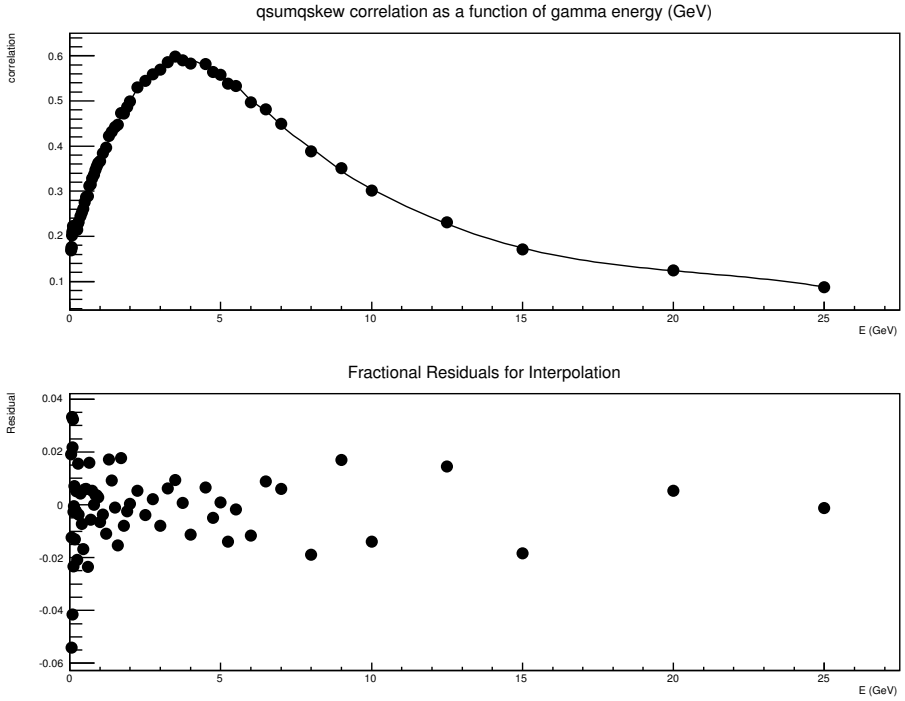

Figure A.8: QSumQSkew correlation as a function of energy

Bibliography

[1] Klaus Winter. *Neutrino physics*. Cambridge monographs on particle physics, nuclear physics and cosmology 1. 1991.

[2] C. L. Cowan et al. “Detection of the Free Neutrino: a Confirmation”. In: *Science* 124.3212 (July 1956), pp. 103–104.

[3] G. Danby et al. “Observation of High-Energy Neutrino Reactions and the Existence of Two Kinds of Neutrinos”. In: *Phys. Rev. Lett.* 9.1 (July 1962), pp. 36–44.

[4] F. J. Hasert et al. “Observation of neutrino-like interactions without muon or electron in the Gargamelle neutrino experiment”. In: *Nuclear Physics B* 73.1 (Apr. 1974), pp. 1–22.

[5] G. S. Abrams et al. “Evidence for Anomalous Lepton Production in e+ - e- Annihilation”. In: *Phys.Rev.Lett.* 35 (1975), pp. 1489–1492.

[6] D. DeCamp et al. “Determination of the number of light neutrino species”. In: *Physics Letters B* 231.4 (Nov. 1989), pp. 519–529.

[7] K. Kodama et al. “Observation of tau neutrino interactions”. In: *Physics Letters B* 504.3 (Apr. 2001), pp. 218–224.

[8] “Precision electroweak measurements on the Z resonance”. In: *Physics Reports* 427.5–6 (May 2006), pp. 257–454.

[9] Ian Johnston Rhind Aitchison. *Gauge theories in particle physics: a practical introduction*. Graduate student series in physics. 1982.

[10] David Jeffery Griffiths. *Introduction to elementary particles*. New York ; Chichester: Wiley, 1987.

[11] Raymond Davis, Don S. Harmer, and Kenneth C. Hoffman. “Search for Neutrinos from the Sun”. In: *Phys. Rev. Lett.* 20.21 (May 1968), pp. 1205–1209.

[12] K. Inoue. “Results from Kamiokande and status of super-Kamiokande”. In: *Nuclear Physics B - Proceedings Supplements* 59.1–3 (Nov. 1997), pp. 267–276.

[13] T. A. Kirsten et al. “GALLEX solar neutrino results and status of GNO”. In: *Nuclear Physics B - Proceedings Supplements* 77.1–3 (May 1999), pp. 26–34.

[14] J. N. Abdurashitov et al. “Measurement of the solar neutrino capture rate with gallium metal. III. Results for the 2002–2007 data-taking period”. In: *Phys. Rev. C* 80.1 (July 2009), p. 015807.

[15] N. Barros. “Final results from SNO”. In: *Nuclear Physics B - Proceedings Supplements* 237–238 (Apr. 2013), pp. 107–110.

[16] K.S. Hirata et al. “Experimental study of the atmospheric neutrino flux”. en. In: *Physics Letters B* 205.2-3 (Apr. 1988), pp. 416–420.

[17] Y. Fukuda et al. “Evidence for Oscillation of Atmospheric Neutrinos”. In: *Phys. Rev. Lett.* 81.8 (Aug. 1998), pp. 1562–1567.

[18] J. A. Formaggio and G. P. Zeller. “From eV to EeV: Neutrino cross sections across energy scales”. In: *Rev. Mod. Phys.* 84.3 (Sept. 2012), pp. 1307–1341.

[19] Carlo Giunti. *Fundamentals of neutrino physics and astrophysics*. Oxford: Oxford University Press, 2007.

[20] J. L. Hewett et al. “Fundamental Physics at the Intensity Frontier”. In: (2012).

[21] C. H. Llewellyn Smith. “Neutrino reactions at accelerator energies”. In: *Physics Reports* 3.5 (June 1972), pp. 261–379.

[22] Dieter Rein and Lalit M Sehgal. “Neutrino-excitation of baryon resonances and single pion production”. In: *Annals of Physics* 133.1 (Apr. 1981), pp. 79–153.

[23] Arie Bodek and Un-ki Yang. “Axial and Vector Structure Functions for Electron- and Neutrino- Nucleon Scattering Cross Sections at all Q^2 using Effective Leading order Parton Distribution Functions”. In: *arXiv:1011.6592 [hep-ex, physics:hep-ph, physics:nucl-ex, physics:nucl-th]* (Nov. 2010).

[24] Boris Kayser. “On the quantum mechanics of neutrino oscillation”. In: *Phys. Rev. D* 24.1 (July 1981), pp. 110–116.

[25] *Neutrino mass*. Springer tracts in modern physics 190. Berlin: Springer, 2003.

[26] L. Wolfenstein. “Neutrino oscillations in matter”. In: *Phys. Rev. D* 17.9 (May 1978), pp. 2369–2374.

[27] A. Y. Smirnov S. P. Mikheev. “Resonance enhancement of oscillations in matter and solar neutrino spectroscopy”. In: *Sov. J. Nucl. Phys. (Engl. Transl.); (United States)* 42:6 (1985).

[28] K. V. Tsang et al. “Results from the Daya Bay Reactor Neutrino Experiment”. In: *Nuclear Physics B - Proceedings Supplements* 246–247 (Jan. 2014), pp. 18–22.

[29] Soo-Bong Kim. “Observation of Reactor Electron Antineutrino Disappearance at RENO”. In: *Nuclear Physics B - Proceedings Supplements* 235–236 (Feb. 2013), pp. 24–29.

[30] M. Apollonio et al. “Limits on neutrino oscillations from the CHOOZ experiment”. In: *Physics Letters B* 466.2–4 (Nov. 1999), pp. 415–430.

[31] A. J. Franke. “Double Chooz: Results and Perspectives”. In: *Nuclear Physics B - Proceedings Supplements* 237–238 (Apr. 2013), pp. 71–76.

[32] A. Piepke. “Final results from the Palo Verde neutrino oscillation experiment”. In: *Progress in Particle and Nuclear Physics* 48.1 (2002), pp. 113–121.

[33] Tadao Mitsui. “KamLAND Results and Future”. In: *Nuclear Physics B - Proceedings Supplements* 221 (Dec. 2011), pp. 193–198.

[34] Jeffrey K. de Jong. “Near-to-Final MINOS Oscillation Results”. In: *Nuclear Physics B - Proceedings Supplements* 237–238 (Apr. 2013), pp. 166–169.

[35] R. B. Patterson. “The NOvA experiment: status and outlook”. In: *Nuclear Physics B - Proceedings Supplements* 235–236 (Feb. 2013), pp. 151–157.

[36] T. Nakaya. “K2K Results”. In: *Nuclear Physics B - Proceedings Supplements* 143 (June 2005), pp. 96–103.

[37] N. Di Marco. “Recent results of the OPERA experiment”. In: *Nuclear Physics B - Proceedings Supplements* 237–238 (Apr. 2013), pp. 187–189.

[38] K. Scholberg. “The Long-Baseline Neutrino Experiment”. In: *Nuclear Physics B - Proceedings Supplements* 237–238 (Apr. 2013), pp. 184–186.

[39] J. Beringer et al. “Review of Particle Physics”. In: *Phys. Rev. D* 86.1 (July 2012), p. 010001.

[40] D. Hywel White. “Neutrino oscillation results from LSND”. In: *Nuclear Physics B - Proceedings Supplements* 77.1–3 (May 1999), pp. 207–211.

[41] C. C. Polly. “Improved statistics in the search for oscillations in MiniBooNE”. In: *Nuclear Physics B - Proceedings Supplements* 235–236 (Feb. 2013), pp. 207–213.

[42] K. Abe et al. “The T2K experiment”. In: *Nuclear Instruments and Methods in Physics Research Section A: Accelerators, Spectrometers, Detectors and Associated Equipment* 659.1 (Dec. 2011), pp. 106–135.

[43] K. Abe et al. “Recent Results from the T2K Experiment”. In: *Nuclear Physics B - Proceedings Supplements* 246–247 (Jan. 2014), pp. 23–28.

[44] F. Retière. “The Neutrino Near Detector Complex of the T2K Experiment”. In: *Physics Procedia* 37 (2012), pp. 1231–1240.

[45] (T2K Collaboration) et al. “Observation of Electron Neutrino Appearance in a Muon Neutrino Beam”. In: *Phys. Rev. Lett.* 112.6 (Feb. 2014), p. 061802.

[46] Shoji Nagamiya. “J-PARC project and its science”. In: *Progress in Particle and Nuclear Physics* 67.2 (Apr. 2012), pp. 580–593.

[47] K. Abe et al. “Measurements of the T2K neutrino beam properties using the INGRID on-axis near detector”. In: *Nuclear Instruments and Methods in Physics Research Section A: Accelerators, Spectrometers, Detectors and Associated Equipment* 694 (Dec. 2012), pp. 211–223.

[48] *http://www.t2k.org - Photographs and figures*.

[49] S. Assylbekov et al. “The T2K ND280 off-axis pi–zero detector”. In: *Nuclear Instruments and Methods in Physics Research Section A: Accelerators, Spectrometers, Detectors and Associated Equipment* 686 (Sept. 2012), pp. 48–63.

[50] Antonin Vacheret. “Characterization of the 1.3 mm 1.3 mm MPPC for the T2K near detectors”. In: *Nuclear Instruments and Methods in Physics Research Section A: Accelerators, Spectrometers, Detectors and Associated Equipment* 623.1 (Nov. 2010), pp. 201–203.

[51] N. Abgrall et al. “Time projection chambers for the T2K near detectors”. In: *Nuclear Instruments and Methods in Physics Research Section A: Accelerators, Spectrometers, Detectors and Associated Equipment* 637.1 (May 2011), pp. 25–46.

[52] A. Delbart. “Production and calibration of 9 m2 of bulk-micromegas detectors for the readout of the ND280/TPCs of the T2K experiment”. In: *Nuclear Instruments and Methods in Physics Research Section A: Accelerators, Spectrometers, Detectors and Associated Equipment* 623.1 (Nov. 2010), pp. 105–107.

[53] P. A. Amaudruz et al. “The T2K fine-grained detectors”. In: *Nuclear Instruments and Methods in Physics Research Section A: Accelerators, Spectrometers, Detectors and Associated Equipment* 696 (Dec. 2012), pp. 1–31.

[54] D. Allan et al. “The electromagnetic calorimeter for the T2K near detector ND280”. en. In: *J. Inst.* 8.10 (Oct. 2013), P10019.

[55] T2K Internal Document. *ND280 Technical Design Report*. 2006.

[56] S. Aoki et al. “The T2K Side Muon Range Detector (SMRD)”. In: *Nuclear Instruments and Methods in Physics Research Section A: Accelerators, Spectrometers, Detectors and Associated Equipment* 698 (Jan. 2013), pp. 135–146.

[57] S. Fukuda et al. “The Super-Kamiokande detector”. In: *Nuclear Instruments and Methods in Physics Research Section A: Accelerators, Spectrometers, Detectors and Associated Equipment* 501.2–3 (Apr. 2003), pp. 418–462.

[58] Masato Shiozawa. “The Hyper-Kamiokande project”. In: *Nuclear Physics B - Proceedings Supplements* 237–238 (Apr. 2013), pp. 289–294.

[59] Antonin Vacheret et al. “The front end readout system for the T2K-ND280 detectors”. In: *IEEE Nuclear Science Symposium Conference Record, 2007. NSS ’07*. Vol. 3. Oct. 2007, pp. 1984–1991.

[60] D. G. Michael et al. “The magnetized steel and scintillator calorimeters of the MINOS experiment”. In: *Nuclear Instruments and Methods in Physics Research Section A: Accelerators, Spectrometers, Detectors and Associated Equipment* 596.2 (Nov. 2008), pp. 190–228.

[61] Richard Graham Calland. *A 3 Flavour Joint Near and Far Detector Neutrino Oscillation Analysis at T2K - PhD Thesis*.

[62] Rene Brun and Fons Rademakers. “ROOT — An object oriented data analysis framework”. In: *Nuclear Instruments and Methods in Physics Research Section A: Accelerators, Spectrometers, Detectors and Associated Equipment* 389.1–2 (Apr. 1997), pp. 81–86.

[63] *MIDAS - http://midas.triumf.ca/MidasWiki/.*

[64] Y. Hayato. “Neut”. In: *Nuclear Physics B - Proceedings Supplements* 112.1–3 (Nov. 2002), pp. 171–176.

[65] C. Andreopoulos et al. “The GENIE neutrino Monte Carlo generator”. In: *Nuclear Instruments and Methods in Physics Research Section A: Accelerators, Spectrometers, Detectors and Associated Equipment* 614.1 (Feb. 2010), pp. 87–104.

[66] S. Agostinelli et al. “Geant4—a simulation toolkit”. In: *Nuclear Instruments and Methods in Physics Research Section A: Accelerators, Spectrometers, Detectors and Associated Equipment* 506.3 (July 2003), pp. 250–303.

[67] *MySQL :: The world’s most popular open source database - http://www.mysql.com/.*

[68] A. Cervera-Villanueva, J. J. Gómez-Cadenas, and J. A. Hernando. ““RecPack” a reconstruction toolkit”. In: *Nuclear Instruments and Methods in Physics Research Section A: Accelerators, Spectrometers, Detectors and Associated Equipment* 534.1–2 (Nov. 2004), pp. 180–183.

[69] A. Hillaret et al. *T2K-TN-072 - ND280 Reconstruction*.

[70] Claudio Giganti and M. Zito. *T2K-TN-001 - Particle Identification with the T2K TPC*.

[71] A. Hoecker et al. "TMVA - Toolkit for Multivariate Data Analysis". In: *arXiv:physics/0703039* (Mar. 2007). PoS ACAT:040,2007.

[72] R. Wigmans. *Calorimetry: energy measurement in particle physics*. International series of monographs on physics 107. Oxford: Clarendon Press ; Oxford University Press, 2000.